NTNU – Trondheim
Norwegian University of
Science and Technology

Optical Properties of truncated and coated spheroidal Nanoparticles on a Substrate

Eskil Aursand

Nanotechnology
Submission date: June 2012
Supervisor: Ingve Simonsen, IFY

Norwegian University of Science and Technology
Department of Physics

Abstract

In nanoparticle research it is common to perform optical measurements on particle films during deposition, to help understand the growth process. GranFilm is a software under development which can calculate the optical properties of an array of truncated nanoparticles supported on a substrate. The theory behind these calculations is based on the work of Bedeaux and Vlieger. One feature which was missing from the software until now was the ability to do such simulations on the case of truncated spheroidal nanoparticles with an arbitrary number of coatings of different materials. In the beginning of this work, the equations needed to perform these simulations are derived, and then reduced to previously derived special cases for verification. The new equations are then implemented into GranFilm, and the new code is put through numerical tests. Finally, the new functionality is tested with the help of experimental data from an oxidation process of a silver nanoparticle film. The qualitative evolution of the optical properties of the film is reproduced quite successfully, but some issues remain.

Sammendrag

Innen nanopartikkelforskning er det vanlig å utføre optiske målinger på partikkelfilmer i løpet av deponering, for å gi mer kunnskap om vekstprosessen. GranFilm er en programvare under utvikling som kan beregne de optiske egenskapene til en film av trunkerte nanopartikler på et substrat. Teorien bak disse beregningene er basert på arbeidene til Bedeaux og Vlieger. En funksjonalitet som manglet til nå var muligheten til å gjøre slike beregninger i tilfellet av trunkerte sfæroidiske nanopartikler med et vilkårlig antall overflatelag av forskjellige materialer. I starten av dette arbeidet blir de nødvendige likningene for å utføre disse simuleringene utledet, og så for verifikasjon redusert til spesialtilfeller utledet tidligere. De nye likningene blir så implementert i GranFilm, og den nye koden blir testet numerisk. Til slutt blir den nye funksjonaliteten testet ved hjelp av eksperimentell data fra en oksidasjonsprosess av en film av sølv-nanopartikler. Den kvalitative utviklingen av de optiske egenskapene til filmen blir reprodusert i sine grove trekk, men noen problemer gjenstår.

Preface

This master's thesis is the final part of a five-year master's program in Nanotechnology at the Norwegian University of Science and Technology in Trondheim. The work on this thesis was performed during the spring semester of 2012, under the supervision of Prof. Ingve Simonsen at the Department of Physics.

The initial work on this thesis consisted of analytical work in the fields of physics and mathematics, a process which is well documented in this report. However, to enable tangible results it also consisted of a large programming part, which for practical reasons cannot be documented in whole in a report like this. The reader is also spared from descriptions of the considerable amount of time spent debugging and quality controlling the code. For those especially interested in the implementation details, the source code of the GranFilm software is freely available for study.

Being a student which is very interested in the fields of physics, mathematics, numerics and programming, my work on this master's thesis has been very rewarding and educational. I am also very happy with the results obtained in a relatively small amount of time. While I would have liked to analyze certain things a little more closely, this was unfortunately prevented by illness in the final month before the deadline.

I would like to thank my supervisor, Prof. Ingve Simonsen, for giving great advice on how to solve the big and small issues which arose during my work, as well as teaching me many new things in the fields of physics and programming. I would also like to thank Dr. Rémi Lazzari from the Paris Institute of Nanosciences for providing me with experimental data crucial for the final part of this work, as well as kindly answering any questions I might have had.

This work builds upon my experiences from my pre-masters project [1] during the fall of 2011. In fact, the introductory parts Sec. 1 and 2 are only slightly modified versions of similar sections from this previous report.

Eskil Aursand
Trondheim, June 2012

Contents

1. Introduction

Nanoparticle growth is an active field of research, both caused by a desire to understand their fascinating optical, electronic and chemical properties, as well as the current and potential practical applications [2, 3]. These applications include nanoelectronics [2, 4], biology/medicine [5, 6, 7], chemical sensing [2, 8], catalysis [9] and composite materials [3].

One way to obtain metallic nanoparticles is to grow them on a substrate through the Volmer-Weber growth mode, where the relatively large surface energy between the substrate and the deposited metal causes the metal to initially deposit as separate islands/particles [3]. During such a deposition it is common to perform an optical measurement called SDRS (Surface Differential Reflectance Spectroscopy) [10, 11], in the hope of learning something about the growth process. This essentially entails measuring the specular reflectance spectrum of the surface using linearly polarized radiation in and around the visible range (see Fig. 1.1). This can be done *in situ*, and typically several spectra are recorded during growth resulting in a time-series. Of particular interest is the *differential reflectance*, which is the difference between the reflectance recorded with the nanoparticles present and the reflectance measured with the bare substrate before deposition. When this difference is normalized with the latter, it is the SDRS signal commonly denoted $\Delta R/R$.

One might wonder why this signal is interesting. It is commonly stated that light in the visible spectrum is quite useless in observing the nanoscale because of the diffraction limit [12]. While this is true for imaging, this SDRS signal allows one to indirectly probe the properties of metallic nanoparticles through nanoplasmonics [13]. When a metallic nanoparticle is exposed to the light's electric field, its electrons are periodically displaced relative to the lattice ions. This induces opposite charges on the opposing surface giving a restoring force, and thus effectively creating an electron oscillator. The quantum of this oscillator is called a *surface plasmon*, with a resonant frequency depending not only on the type of metal, but also on the particle's size, shape and environment [13]. This is the key to gaining information about the nanoparticles using visible light: The optical properties of a substrate covered with metallic nanoparticles depend on the excitation of plasmon modes, and the latter depends sensitively on the size and shape of these particles.

A recorded SDRS signal, such as the one shown in the inset in Fig. 1.1, is quite useless alone however. One obviously cannot read particle size and shape

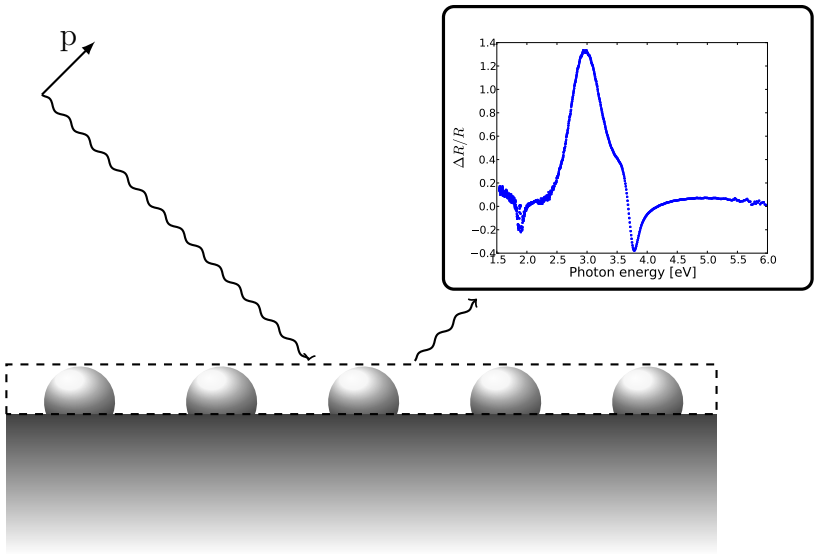

Figure 1.1.: A schematic illustration of a common SDRS measurement. The substrate is exposed to linearly polarized light, causing some of it to be transmitted and some of it to be reflected. The specularly reflected light is collected into a spectrometer, giving data on the reflectance for different photon energies. If the same measurement was also done with the bare substrate before the growth began, one can find and plot the quantity *differential reflectance* ($\Delta R/R$), as shown in the inset.

directly from the curve. What is needed is a theoretical model for the physical process causing the observed phenomenon. When this is in place one can simulate the phenomenon to see what kind of particles would cause the obtained measurement. Several attempts have been made to model the phenomenon, including effective medium theories [14] and the Yamaguchi model [15, 16]. These theories fail in completely describing the observations because the approximations are too rough and/or because they oversimplify the geometry. Because of these inadequacies there was a need for a new model, which could properly account for the break in symmetry caused by particle truncation, interactions with the substrate, and interactions between neighboring particles.

Such a model was developed by Bedeaux and Vlieger [17]. It is seated in the framework of classical electromagnetism, and essentially entails solving Maxwell's Equations in the area of the nanoparticles using appropriate approximations. The theory can be quickly summarized as follows: The goal is to find the Fresnel coefficients [18] of the nanoparticle covered substrate sur-

face, which essentially contain all the information needed on its macroscopic optical properties. The presence of the nanoparticles, or *metallic islands* as they are often called, represent a perturbation from the easily solvable case of an ideally flat surface between two bulk media. This perturbation is described through the formalism of *excess fields*, and by doing so one can express the Fresnel coefficients in terms of *surface susceptibilities*. The latter depends on the density of particles and their individual polarizabilities.

The final and most complex stage of the treatment entails finding the polarizability of a truncated particle (or *island*) supported on a substrate. When they are much smaller than the optical wavelength, this can thankfully be reduced to an electrostatic problem. For islands of a single material, *i.e.* with no coating, the problem has been solved analytically by Bedeaux and Vlieger [17] for spherical and spheroidal islands. The derivation results in an infinite system of linear equations which can be truncated to a specific multipole order depending on the desired accuracy. Solving this requires numerical methods on a computer, both because the linear system is very large and because the matrix elements contain integrals which cannot be calculated analytically in most cases. A solution of this system can be used to find the polarizabilities, the surface susceptibilities, the Fresnel coefficients and finally the reflectance.

A numerical simulation based on this theoretical treatment has been implemented as part of a computer software named GranFilm [19], which has been in development for several years now. In fact, just before the beginning of this work, a solution for spherical islands with an arbitrary number of coatings had been derived and implemented in GranFilm. One thing which was missing however, was similar functionality for spheroidal islands. While the original work of Bedeaux and Vlieger had already derived some results for spheroidal islands, these did not cover the case of islands with an arbitrary number of coatings of any thickness. This missing functionality is what this work aims to create.

The three main goals of this work is to:

- Perform an analytical derivation for solving the above problem for the case of coated spheroidal islands truncated and supported on a substrate. This will be inspired by both the work on non-coated spheroidal islands by Bedeaux and Vlieger and the derivations made by Prof. Ingve Simonsen for the case of coated spherical islands.

- Implement (*i.e.* program) the results of the analytical derivation as an integral part of the existing GranFilm 2.0 code, and perform numerical tests to ensure that it has been done correctly.

- Do a preliminary test of comparing the numerical results to experimental data. In this case it entails trying to reproduce general trends from SDRS

data recorded during oxidation of silver islands on a substrate.

The contents of this report may be summarized as follows: Section 2 covers the necessary theoretical background, including the formalism of excess fields and how the surface susceptibilities relate to the optical properties of the surface. This mostly consists of summaries of relevant parts of the book by Bedeaux and Vlieger [17]. Section 3 contains the main analytical work of this report, which is mostly solving Laplace's equation for the case of a coated spheroidal island truncated and supported on a substrate, exposed to a homogeneous electric field. Some verifications of these results are presented in Sec. 4, as they are reduced to the two previously available special cases and compared. Section 5 covers the implementation and integration of the new equations into GranFilm, as well as the numerical tests performed to verify correctness and convergence. Section 6 presents the results from the attempt to qualitatively reproduce the observed evolution of the SDRS spectrum as Ag islands are exposed to oxygen gas, which may be expected to create a coating of Ag_2O on the islands. Section 7 contains analyses and discussions concerning all the performed work and obtained results, while Sec. 8 attempts to draw some final conclusions.

This report also contains some appendices (A – D), which cover technical details not essential for understanding the theory or the results, but which could be very useful for someone attempting to understand and/or modify the added source code in GranFilm.

2. Background

While deriving the optical properties of a uniform planar interface is a standard procedure in optics textbooks [18], the interfaces to be treated here are not discontinuous transitions from one homogeneous bulk to another, but rather *non-sharp*. Initially a general non-sharp interface will be considered, such as

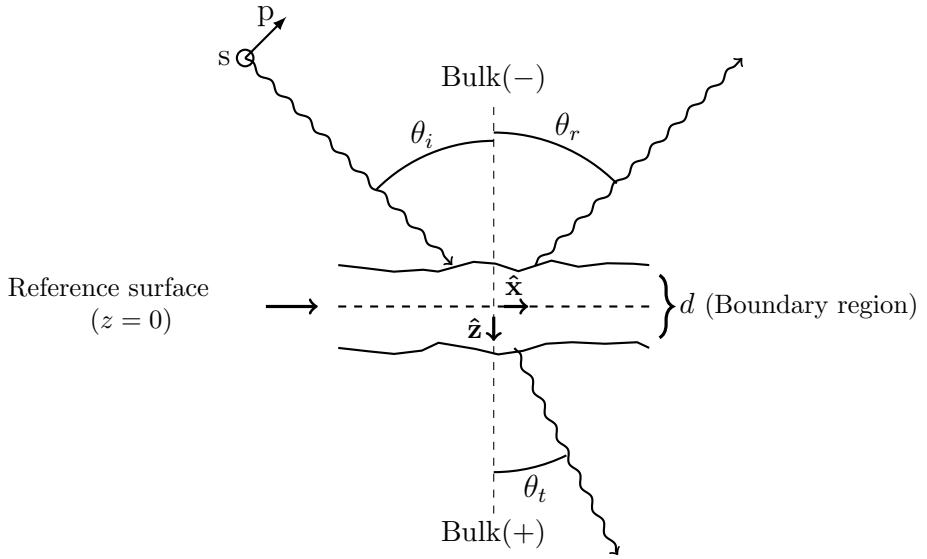

Figure 2.1.: An illustration of the general non-sharp interface to be considered. A boundary region of thickness d is surrounded by bulk media on both sides. Inside this boundary region the $z = 0$ plane is placed, which will be referred to as the *reference surface*. Incident radiation is coming from the bulk in the negative z region at an angle θ_i, causing a reflected beam (θ_r) and a transmitted beam (θ_t). The two linear polarization directions termed p and s are shown at the start of the incident beam.

the one shown in Fig. 2.1. To help describe the electromagnetic properties of such a boundary region, the formalism of *excess quantities* by Bedeaux and Vlieger [17] will be summarized in Sec. 2.1. Once this is in place, the Fresnel coefficients of such an interface can be found in terms of a few properties of

the general boundary region called *surface susceptibilities* (Sec. 2.2). These surface susceptibilities will depend on the internal structure of the boundary region. The derivation of this for the case of a film of truncated and coated spheroidal islands will be presented in Sec. 3. Tabulated values found for the dielectric functions of metals are not necessarily appropriate for nanoparticles. Some of the corrections needed to account for this will be covered in Sec. 2.3.

2.1. Boundary conditions at non-sharp interfaces

Our starting point is the Maxwell equations [20], which in SI units are given by

$$\nabla \cdot \mathbf{D} = \rho \tag{2.1a}$$

$$\nabla \cdot \mathbf{B} = 0 \tag{2.1b}$$

$$\nabla \times \mathbf{E} = -\frac{\partial \mathbf{B}}{\partial t} \tag{2.1c}$$

$$\nabla \times \mathbf{H} = \mathbf{J} + \frac{\partial \mathbf{D}}{\partial t}, \tag{2.1d}$$

where the vectors $\mathbf{D}$, $\mathbf{B}$, $\mathbf{E}$, $\mathbf{H}$ are the electric displacement field, the magnetic flux density, the electric field and the magnetic field, respectively. The density of free charges is given by ρ, while $\mathbf{J}$ is the density of free current.

To describe the properties of a boundary layer like the one shown in Fig. 2.1 without considering the details along the axis perpendicular to it, one may introduce the concept of *excess quantities*. It will be shown that the boundary conditions for extrapolated bulk fields at the reference surface may be expressed in terms of these excesses. A detailed introduction to excess quantities can be found in the book by Bedeaux and Vlieger [17].

As an example, the excess electric field ($\mathbf{E}_{\text{ex}}$) is defined by

$$\mathbf{E}_{\text{ex}}(\mathbf{r}, t) \equiv \mathbf{E}(\mathbf{r}, t) - \mathbf{E}^{-}(\mathbf{r}, t)\theta(-z) - \mathbf{E}^{+}(\mathbf{r}, t)\theta(z), \tag{2.2}$$

where $\theta(z)$ is the step function. The fields $\mathbf{E}^{+}$ and $\mathbf{E}^{-}$ are examples of *bulk extrapolated quantities*, corresponding to the bulk on the $z > 0$ and the $z < 0$ side of Fig. 2.1, respectively. These bulk extrapolated quantities are the same as the real quantities when far away from the boundary. When in the boundary layer, these quantities are extrapolated from their values in the bulk. It follows that the excess quantities are nonzero only in the region of the boundary. Other excess quantities are defined equivalently.

Inserting the real field from Eq. (2.2) and its equivalents into the Maxwell equations (2.1), while using that the Maxwell equations should also hold for the extrapolated fields, and the fact that $\nabla\theta(z) = \delta(z)\hat{\mathbf{z}}$, one can find the

following new set of equations for the excess fields

$$\nabla \cdot \mathbf{D}_{\rm ex}(\mathbf{r},t) + (D_z^+(\mathbf{r},t) - D_z^-(\mathbf{r},t))|_{z=0}\delta(z) = \rho_{\rm ex}(\mathbf{r},t), \tag{2.3a}$$

$$\nabla \cdot \mathbf{B}_{\rm ex}(\mathbf{r},t) + (B_z^+(\mathbf{r},t) - B_z^-(\mathbf{r},t))|_{z=0}\delta(z) = 0, \tag{2.3b}$$

$$\nabla \times \mathbf{E}_{\rm ex}(\mathbf{r},t) + \hat{\mathbf{z}} \times (\mathbf{E}_\parallel^+(\mathbf{r},t) - \mathbf{E}_\parallel^-(\mathbf{r},t))|_{z=0}\delta(z) = -\frac{\partial \mathbf{B}_{\rm ex}(\mathbf{r},t)}{\partial t}, \tag{2.3c}$$

$$\nabla \times \mathbf{H}_{\rm ex}(\mathbf{r},t) + \hat{\mathbf{z}} \times (\mathbf{H}_\parallel^+(\mathbf{r},t) - \mathbf{H}_\parallel^-(\mathbf{r},t))|_{z=0}\delta(z) = \mathbf{J}_{\rm ex}(\mathbf{r},t) + \frac{\partial \mathbf{D}_{\rm ex}(\mathbf{r},t)}{\partial t}, \tag{2.3d}$$

where all excess quantities are defined in ways equivalent to Eq. (2.2). The unit normal vector to the flat reference surface is given by $\hat{\mathbf{z}}$.

Integrating Eqs. (2.3) along the entire z-axis, one can find the following boundary conditions for the bulk extrapolated fields at the reference surface:

$$\left[D_z^+(\mathbf{r}_\parallel,t) - D_z^-(\mathbf{r}_\parallel,t)\right]|_{z=0} = -\nabla_\parallel \mathbf{D}_\parallel^s(\mathbf{r}_\parallel,t) + \rho^s(\mathbf{r}_\parallel,t), \tag{2.4a}$$

$$\left[B_z^+(\mathbf{r}_\parallel,t) - B_z^-(\mathbf{r}_\parallel,t)\right]|_{z=0} = -\nabla_\parallel \mathbf{B}_\parallel^s(\mathbf{r}_\parallel,t), \tag{2.4b}$$

$$\left[E_x^+(\mathbf{r}_\parallel,t) - E_x^-(\mathbf{r}_\parallel,t)\right]|_{z=0} = \frac{\partial}{\partial x}E_z^s(\mathbf{r}_\parallel,t) - \frac{\partial}{\partial t}B_y^s(\mathbf{r}_\parallel,t), \tag{2.4c}$$

$$\left[E_y^+(\mathbf{r}_\parallel,t) - E_y^-(\mathbf{r}_\parallel,t)\right]|_{z=0} = \frac{\partial}{\partial y}E_z^s(\mathbf{r}_\parallel,t) + \frac{\partial}{\partial t}B_x^s(\mathbf{r}_\parallel,t), \tag{2.4d}$$

$$\left[H_x^+(\mathbf{r}_\parallel,t) - H_x^-(\mathbf{r}_\parallel,t)\right]|_{z=0} = \frac{\partial}{\partial x}H_z^s(\mathbf{r}_\parallel,t) + \frac{\partial}{\partial t}D_y^s(\mathbf{r}_\parallel,t) + J_y^s(\mathbf{r}_\parallel,t), \tag{2.4e}$$

$$\left[H_y^+(\mathbf{r}_\parallel,t) - H_y^-(\mathbf{r}_\parallel,t)\right]|_{z=0} = \frac{\partial}{\partial y}H_z^s(\mathbf{r}_\parallel,t) - \frac{\partial}{\partial t}D_x^s(\mathbf{r}_\parallel,t) - J_x^s(\mathbf{r}_\parallel,t), \tag{2.4f}$$

where the superscript s indicates a *total excess quantity*, which is the excess of the indicated quantity integrated along the entire z-axis.

One can also introduce polarization and magnetization densities for the interface. The total excess surface polarization is given by [17]

$$\mathbf{P}^s(\mathbf{r}_\parallel,t) \equiv [\mathbf{D}_\parallel^s(\mathbf{r}_\parallel,t), -\epsilon_0 E_z^s(\mathbf{r}_\parallel,t)], \tag{2.5}$$

and the surface magnetization by

$$\mathbf{M}^s(\mathbf{r}_\parallel,t) \equiv [\frac{1}{\mu_0}\mathbf{B}_\parallel^s(\mathbf{r}_\parallel,t), -H_z^s(\mathbf{r}_\parallel,t)], \tag{2.6}$$

where the superscripts s again indicate a *total excess* quantity. The quantities ϵ_0 and μ_0 are the electric permittivity and magnetic permeability of vacuum respectively. It is important to stress that Eqs. (2.5) and (2.6) must be used for the surface polarization and surface magnetization, and not simply the z-integral over some excess polarization and magnetization densities [17].

Using the relations in Eqs. (2.5) and (2.6), one can transform Eqs. (2.4) into the following boundary conditions for the bulk extrapolated fields:

$$(D_z^+ - D_z^-)|_{z=0} = -\nabla_\parallel \mathbf{P}_\parallel^s + \rho^s, \tag{2.7a}$$

$$(B_z^+ - B_z^-)|_{z=0} = -\mu_0 \nabla_\parallel \mathbf{M}_\parallel^s, \tag{2.7b}$$

$$(\mathbf{E}_\parallel^+ - \mathbf{E}_\parallel^-)|_{z=0} = \mu_0 \frac{\partial}{\partial t}\left(\hat{\mathbf{z}} \times \mathbf{M}_\parallel^s\right) - \frac{1}{\epsilon_0}\nabla_\parallel P_z^s, \tag{2.7c}$$

$$(\mathbf{H}_\parallel^+ - \mathbf{H}_\parallel^-)|_{z=0} = -\frac{\partial}{\partial t}\left(\hat{\mathbf{z}} \times \mathbf{P}_\parallel^s\right) - \nabla_\parallel M_z^s - \hat{\mathbf{z}} \times \mathbf{J}_\parallel^s, \tag{2.7d}$$

where the dependence on variables $(\mathbf{r}_\parallel, t)$ is implicit on all the field quantities, as well as ρ^s and $\mathbf{J}^s$.

In time-dependent problems, it can be convenient to define a quantity called the *generalized electric displacement field*, given in terms of the Fourier transformed displacement field and current density by

$$\mathbf{D}'(\mathbf{r}, \omega) \equiv \mathbf{D}(\mathbf{r}, \omega) + \frac{i}{\omega}\mathbf{J}(\mathbf{r}, \omega). \tag{2.8}$$

Here ω is the angular frequency variable introduced by the Fourier transform. Using this generalized electric displacement field, one can also define a generalized surface polarization density as

$$\mathbf{P}'^s(\mathbf{r}_\parallel, t) \equiv [\mathbf{D}_\parallel'^s(\mathbf{r}_\parallel, t), -\epsilon_0 E_z^s(\mathbf{r}_\parallel, t)]. \tag{2.9}$$

By using Eqs. (2.8) and (2.9) together with the Fourier transform of Eqs. (2.7), and using the frequency domain expression of charge conservation given by

$$i\omega\rho(\mathbf{r}, \omega) = \nabla \cdot \mathbf{J}(\mathbf{r}, \omega), \tag{2.10}$$

one can express the boundary conditions as:

$$\left[D_z^+(\mathbf{r}_\parallel, \omega) - D_z^-(\mathbf{r}_\parallel, \omega)\right]\Big|_{z=0} = -\nabla_\parallel \mathbf{P}_\parallel'^s(\mathbf{r}_\parallel, \omega), \tag{2.11a}$$

$$\left[B_z^+(\mathbf{r}_\parallel, \omega) - B_z^-(\mathbf{r}_\parallel, \omega)\right]\Big|_{z=0} = -\mu_0 \nabla_\parallel \mathbf{M}_\parallel^s(\mathbf{r}_\parallel, \omega), \tag{2.11b}$$

$$\left[\mathbf{E}_\parallel^+(\mathbf{r}_\parallel, \omega) - \mathbf{E}_\parallel^-(\mathbf{r}_\parallel, \omega)\right]\Big|_{z=0} = -i\omega\mu_0 \hat{\mathbf{z}} \times \mathbf{M}_\parallel^s(\mathbf{r}_\parallel, \omega) - \frac{1}{\epsilon_0}\nabla_\parallel P_z^s(\mathbf{r}_\parallel, \omega), \tag{2.11c}$$

$$\left[\mathbf{H}_\parallel^+(\mathbf{r}_\parallel, \omega) - \mathbf{H}_\parallel^-(\mathbf{r}_\parallel, \omega)\right]\Big|_{z=0} = i\omega\hat{\mathbf{z}} \times \mathbf{P}_\parallel'^s(\mathbf{r}_\parallel, \omega) - \nabla_\parallel M_z^s(\mathbf{r}_\parallel, \omega). \tag{2.11d}$$

To simplify the notation, the primes will be dropped and the symbols $\mathbf{D}$ and $\mathbf{P}$ will from now on refer to the generalized displacement field and polarization respectively.

For these boundary conditions (2.11) to have any practical use, one needs constitutive equations relating the interfacial polarization and magnetization densities to the extrapolated fields outside the boundary region.

In the absence of spatial dispersion in the interface, the general constitutive relation is given by [17]

$$\mathbf{P}^s(\mathbf{r}_\parallel, \omega) = \xi_e^s(\omega) \cdot [\epsilon_0 \mathbf{E}_{\parallel,\Sigma}(\mathbf{r}_\parallel, \omega), D_{z,\Sigma}(\mathbf{r}_\parallel, \omega)], \tag{2.12}$$

where ξ is the *constitutive tensor*, and the subscript Σ indicates the arithmetic mean of the two corresponding bulk extrapolated fields at the reference surface ($z = 0$). From now on the discussion will be limited to non-magnetic materials ($\mathbf{M}^s$=0), and thus no corresponding constitutive relation for the surface magnetization density will be presented.

If the interface is isotropic, homogeneous and symmetric, the constitutive tensor is given by [17]

$$\xi_e^s(\omega) = \begin{bmatrix} \gamma(\omega) & 0 & 0 \\ 0 & \gamma(\omega) & 0 \\ 0 & 0 & \beta(\omega) \end{bmatrix}, \tag{2.13}$$

where the constitutive coefficients γ and β are called the *first order surface susceptibilities*. These coefficients have the dimensions of length[1].

The description given by Eqs (2.12) and (2.13) ignore the possible spatial dispersion in the interface. This effect can be taken into account by introducing constitutive coefficients of second order (δ and τ). Their influence on the optical properties are a factor of d/λ smaller than that of the first order coefficients, so they can be neglected in an approximation if the interface is thin enough compared to the optical wavelength [17].

2.2. Optical response of non-sharp interfaces

It is a standard procedure in optics textbooks [18] to derive the *Fresnel equations* for a uniform and planar boundary between two bulk media[2]. This is done by expressing the fields as a superposition of incoming and reflected plane waves on one side, and a transmitted plane wave on the other side, and inserting these fields into the boundary conditions which Maxwell's equations imply for a sharp interface. This leads to the laws of reflection and refraction, as well as expressions for the reflection and transmission amplitudes for the interface.

Here we are treating interfaces which are *not* perfectly sharp, but a derivation of the same form can now be done in the following way [17]: The fields

[1] Recall that the total excess quantities have an extra dimension of length compared to the quantities themselves.

[2] Sometimes called a *Fresnel interface*

constructed from plane wave solutions can now take the role of the bulk extrapolated fields, which can be expressed in terms of reflection and transmission amplitudes. By extrapolating them to the reference surface to express the averages (subscript Σ) and inserting them into Eq. (2.12), one can find the surface polarization density. By inserting this surface polarization density into the right hand side of Eqs. (2.11), using the bulk extrapolated fields to express the differences on the left side, and assuming non-magnetic materials ($\mathbf{M}^s$=0), one can solve for the new amplitudes of reflection and transmission. During this derivation, one also finds that the laws of reflection and refraction stay in their traditional form.

For non-magnetic media, while ignoring spatial dispersion ($\delta = \tau = 0$), one finds the following reflection and transmission amplitudes for s and p polarization [17, 21, 19]:

$$r_s(\omega) = \frac{n^- \cos(\theta_i) - n^+ \cos(\theta_t) + i(\omega/c)\gamma}{n^- \cos(\theta_i) + n^+ \cos(\theta_t) - i(\omega/c)\gamma}, \tag{2.14}$$

$$t_s(\omega) = \frac{2n^- \cos(\theta_i)}{n^- \cos(\theta_i) + n^+ \cos(\theta_t) - i(\omega/c)\gamma}, \tag{2.15}$$

$$\begin{aligned} r_p(\omega) =& \Bigg\{ \left[n^+ \cos(\theta_i) - n^- \cos(\theta_t)\right] \left(1 - \left(\frac{\omega}{2c}\right)^2 \gamma\beta\epsilon^- \sin^2(\theta_i)\right) \\ &+ i\frac{\omega}{c} \left[\beta\epsilon^- n^+ n^- \sin^2(\theta_i) - \gamma \cos(\theta_i)\cos(\theta_t)\right] \Bigg\} \\ &\Big/ \Bigg\{ \left[n^+ \cos(\theta_i) + n^- \cos(\theta_t)\right] \left(1 - \left(\frac{\omega}{2c}\right)^2 \gamma\beta\epsilon^- \sin^2(\theta_i)\right) \\ &- i\frac{\omega}{c} \left[\beta\epsilon^- n^+ n^- \sin^2(\theta_i) + \gamma \cos(\theta_i)\cos(\theta_t)\right] \Bigg\}, \end{aligned} \tag{2.16}$$

$$\begin{aligned} t_p(\omega) =& \left\{ 2n^- \cos(\theta_i) \left[1 + \left(\frac{\omega}{2c}\right)^2 \gamma\beta\epsilon^- \sin^2(\theta_i)\right] \right\} \\ &\Big/ \Bigg\{ \left[n^+ \cos(\theta_i) + n^- \cos(\theta_t)\right] \left(1 - \left(\frac{\omega}{2c}\right)^2 \gamma\beta\epsilon^- \sin^2(\theta_i)\right) \\ &- i\frac{\omega}{c} \left[\beta\epsilon^- n^+ n^- \sin^2(\theta_i) + \gamma \cos(\theta_i)\cos(\theta_t)\right] \Bigg\}, \end{aligned} \tag{2.17}$$

where $n^\pm$ is the bulk refractive index for the region indicated by the superscript. In non-magnetic materials, $n = \sqrt{\epsilon}$, where ϵ is the relative permittivity (or dielectric function) of the given medium. The angle of incidence and the angle of transmission is given by θ_i and θ_t, respectively. They can be related to each

other by the law of refraction $[n^- \sin(\theta_i) = n^+ \sin(\theta_t)]$ (See also Figure 2.1). The constant $c = 1/\sqrt{\epsilon_0 \mu_0}$ is the speed of light in vacuum.

It should be noted that the exact position of the reference surface ($z = 0$) in the mathematical derivation carries no physical significance, and thus measurable quantities should not depend on this choice. The constitutive coefficients $(\gamma, \beta, \delta, \tau)$ do depend on this, as do the amplitudes of reflection and transmission. One can, however, define new quantities called *invariants*. These are combinations of constitutive coefficients which are independent of the position of the reference surface. It can be shown [17] that the reflection and transmission amplitudes can be written as a term involving only invariants, multiplied by a phase factor which is not invariant. The dependence in the latter is not a problem, since these amplitudes are not directly measurable, and the phase factor will disappear when calculating the coefficient of reflection (R) and the coefficient of transmission (T), which *are* measurable.

Note also that in the limit of a perfectly sharp interface, where $\gamma = \beta = 0$ because there is no boundary region with excess polarization, Eqs. (2.14), (2.15), (2.16) and (2.17) reduce to the traditional amplitudes for a Fresnel interface [17, 18], as required.

While the amplitudes of reflection and transmission are not directly measurable, the coefficients of reflection and transmission are. They can be defined as the ratio of reflected to incident power and transmitted to incident power respectively. By assuming energy conservation at the interface, one can find the following expressions for them in terms of the amplitudes [18]

$$R = |r|^2 \tag{2.18}$$

$$T = \frac{n^+ \cos(\theta_t)}{n^- \cos(\theta_i)} |t|^2 \tag{2.19}$$

Be aware that T is not simply given by $|t|^2$, since one must take into account a different wave speed and direction in the substrate.

2.3. Finite-size corrections to the dielectric function of metals

Tabulated values for the dielectric function are often measured for bulk materials. When doing calculations on nano-sized metallic islands however, these values might not be accurate. This section will cover some of the corrections to ϵ needed for small particle sizes.

When the size of the particles become comparable to the mean free path of the conduction electrons in the bulk, the dielectric function will start to be affected. The mean free path is an important contributor to the dielectric

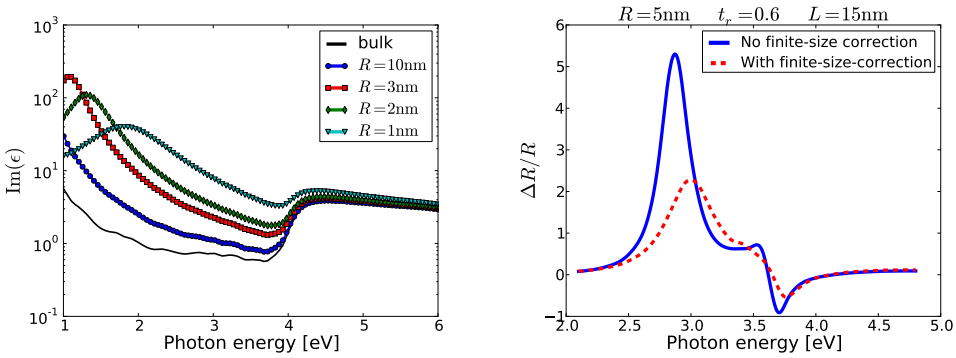

(a) (b)

Figure 2.2.: The effect of the finite-size correction given in Eq. 2.20 with $\hbar\omega_p = 9.17\,\text{eV}$, $\hbar/\tau_b = 0.018\,\text{eV}$, $\hbar v_f = 0.91\,\text{eV nm}$ and $B = -1.13\,\text{eV}^2\text{nm}$ (values for silver from [22]). a) The effect on the imaginary part of the dielectric function on a logarithmic scale for a set of different radii, while holding the truncation ratio at 0.6. b) The effect on the $\Delta R/R$ signal as calculated by GranFilm with parameters $R = 5\,\text{nm}$ (spherical), $t_r = 0.6$ and $L = 15\,\text{nm}$.

function, and in the bulk case it is determined by the probability of the electrons scattering off the lattice inside the material. In the case of small particles however, surface and interface scattering become important contributors which essentially have the effect of reducing the mean free path of the electrons, thus also reducing the electron relaxation time. [22, 23] There is another finite-size effect as well, due to a reduced screening of the sp electrons by the d electrons at the surface/interface [22]. This has the effect of blue-shifting or red-shifting the plasmon frequency of the particles, depending on the type of metal [24].

The corrections to the dielectric function due to both these finite-size effects can be approximated by the following equation [22]

$$\epsilon(\omega) = \epsilon_B(\omega) + \frac{\omega_p^2}{\omega^2 + i\omega/\tau_B} - \frac{\omega_p^2}{\omega^2 + \Sigma + i\omega/\tau}, \tag{2.20}$$

where $\epsilon_B(\omega)$ is the material's bulk dielectric function, τ_B is the bulk relaxation time, Σ is the plasmon frequency shift, and τ is the finite-size corrected relaxation time. The latter is given by [25]

$$\tau^{-1} = \tau_B^{-1} + v_F l^{-1}, \tag{2.21}$$

where v_F and l are the Fermi velocity and the mean free path of the electrons respectively. It is not quite clear what the mean free path is in a truncated

sphere however, but a good candidate was found [25] to be half of the particle's height, *i.e.*

$$l = \frac{1}{2}(1 + t_r)R. \tag{2.22}$$

In the oblate spheroidal case, which is the main focus in this work, the radius along the short axis ($R_\perp$) will be used for R in Eq. 2.22, thus keeping l at half of the particle's height. See Sec. 3.1 for definitions of $R_\perp$, t_r and other parameters of the truncated spheroidal shape.

The plasmon shift can be expressed as [22]

$$\Sigma = B\frac{S}{V}, \tag{2.23}$$

where B is a material dependent constant, and S and V are the surface area and volume of the truncated spheroids respectively. The surface-to-volume ratio may be found by using Eqs. (3.115) and (3.116) for the volume and surface area of a truncated spheroid.

Figure 2.2 shows the imaginary part of the dielectric function of silver for different islands sizes, compared to the bulk value. Also shown is the effect on the simulated SDRS signal. As seen, the finite-size effect can have a significant effect on the dielectric function of the islands, and thus also the SDRS signal. Beware that the correction given in Eq. 2.20 is only an approximation which does not correct the interband part of the dielectric function, nor does it account for any size quantization [25].

3. Spheroidal island films

As summarized in in Sec. 2, one may calculate the optical properties of a generic boundary layer if one can find its *surface susceptibilities*. These quantities will obviously depend on the contents of this boundary layer. In this section the surface susceptibilities for a film of truncated and coated oblate spheroidal nanoparticles (or islands) supported on a substrate will be derived, using a quasi static approximation.

Sections 3.1 and 3.2 will introduce the spheroidal shape and the formalism and notation used when dealing with a set of concentric spheroids, which is needed when deriving results for islands with an arbitrary number of coating layers. Section 3.3 will go through the formalism of the oblate spheroidal coordinate system. In Sec. 3.4 the entire process of finding the polarizabilities of a truncated and coated spheroidal island supported on a substrate is gone through in detail. This involves solving the Laplace equation for the quasi static case in each homogeneous region using multipole expansions, in such a way that the required boundary conditions are as closely satisfied as possible at all interfaces between different regions. Section 3.5 summarizes how one goes from having the polarizabilities of a single island, to having the surface susceptibilities of a film of such islands. This includes corrections (to dipolar order) for interactions between different islands.

3.1. Spheroids

An oblate spheroid is an object obtained by rotating an ellipse about its minor axis. In this text the axis of symmetry will always be along the z-axis, which by definition will be perpendicular to the substrate surface. The equation for such a spheroidal surface is

$$\frac{x^2+y^2}{R_\parallel^2}+\frac{z^2}{R_\perp^2}=1, \tag{3.1}$$

with $R_\parallel > R_\perp$ for it to be oblate. The parameters $R_\parallel$ and $R_\perp$ are the distances from the center to the surface along $\widehat{r}_\parallel$ and the z axis respectively. Specifying such spheroids requires two parameters, but they do not have to be these two radii. Another important parameter is the distance from the center to the two *focal points* of the rotated ellipse, which in the spheroidal case is the radius of

the *focal ring*. This is given in terms of the radii as

$$a = \sqrt{R_{\parallel}^2 - R_{\perp}^2}. \tag{3.2}$$

Another parameter is the *eccentricity* $0 < e < 1$, which is a dimensionless measure of the deviation from a sphere, and given by

$$e = \frac{a}{R_{\parallel}} = \sqrt{1 - \left(\frac{R_{\perp}}{R_{\parallel}}\right)^2}. \tag{3.3}$$

One can also specify a *flattening parameter* $0 \leq \xi_0 < \infty$ given by

$$\xi_0 = \frac{R_{\perp}}{a} = \frac{R_{\perp}}{eR_{\parallel}} = \frac{R_{\perp}}{\sqrt{R_{\parallel}^2 - R_{\perp}^2}}. \tag{3.4}$$

The behavior of these parameters in the limiting cases of a sphere and a circular disc are as follows:

$$\begin{aligned} \text{Sphere}: &\quad a \to 0,\ e \to 0,\ \xi_0 \to \infty,\ a\xi_0 \to R \\ \text{Disc}: &\quad a \to R,\ e \to 1,\ \xi_0 \to 0, \end{aligned} \tag{3.5}$$

where R is the radius of the sphere or disc. One might ask why one bothers to introduce a parameter such as ξ_0. As will be detailed later, it turns out that in the oblate spheroidal coordinate system (ξ, η, ϕ) which will be used here, surfaces of constant $\xi = \xi_0$ are oblate spheroids with a ξ_0 of this value.

Figure 3.1 illustrates a vertical section through the center of an oblate spheroid, and some relationships between the parameters. Here another feature is also introduced, namely *truncation* by a substrate surface placed at $z = d$. Characterizing this island truncation requires an additional third parameter called the *truncation ratio*, given by

$$t_r \equiv \frac{d}{R_{\perp}} = \frac{d}{a\xi_0}, \tag{3.6}$$

where one has $0 \leq t_r \leq 1$ when the center is above the substrate and $-1 \leq t_r \leq 0$ when the center is below the substrate.

3.2. Concentric spheroids

When the aim is to calculate the properties of spheroidal nanoparticles with one or more coating layers, a question arises about what constraints one should put on the shapes of these concentric spheroids. Lets say that one is free to specify any spheroid as the outermost interface. May the interface between the

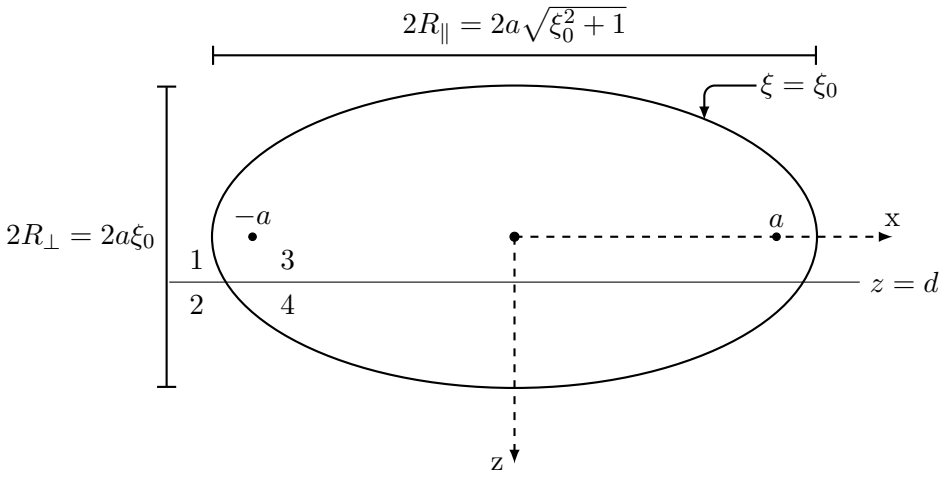

Figure 3.1.: Illustration of a vertical section through the center of an oblate spheroid, also specifying a right handed Cartesian coordinate system. Here the substrate surface is also indicated, placed in the plane $z = d$. Note that if the origin (and center of the spheroid) was below the substrate surface, the parameter d would be negative. The media in this example are labelled 1 through 4 for later reference.

first coating and the next be any spheroid as long as it is contained within the outer interface? It turns out that one constraint simplifies the mathematics of satisfying the boundary conditions between different media considerably. As will be shown in the next section, making all the spheroidal interfaces have the same focal radius a will ensure that all of them are surfaces of constant ξ in the same spheroidal coordinate system. An example of such a set of concentric spheroids may be seen in Fig. 3.2. The spheroidal interfaces are numbered as indicated, with the outermost always being the first one. Generally each of the interfaces has a number $s = 1, .., S$, where $S \geq 1$ is the total number of spheroidal interfaces. The number of coating layers on the inner particles is thus $S - 1$. The media around a spheroidal interface are labelled as shown in Fig. 3.3. Interface s separates medium $2s - 1$ from medium $2s + 1$ above the substrate surface, and $2s$ from $2s + 2$ below the substrate surface. Each interface has its own parameters, like the radii $R_{\parallel,s}$ and $R_{\perp,s}$, though as mentioned always within the constraint that they all have the same focal radius a. To completely specify the geometry one might do the following: Give the horizontal and vertical radii of the outermost surface, $R_{\parallel,1}$ and $R_{\perp,1}$. Based on this one can calculate the focal radius a through Eq. 3.2. One must also

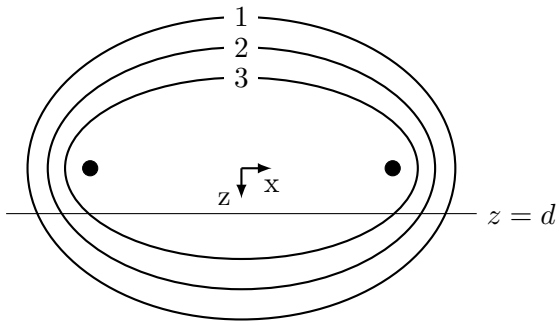

Figure 3.2.: An example case of concentric spheroids with $S = 3$. All of the spheroids have the same focal ring, indicated here by the black dots on the x-axis. In this case all spheroids are truncated, so there are $2S+2$ different media present. In this example the outer spheroid has a flattening parameter ξ_0 equal to one.

specify the truncation ratio of the outer interface ($t_r^{(1)}$), as defined in Eq. 3.6. Because of the constraint of having a common focal ring, each of the inner interfaces $s > 1$ may now be specified by a single parameter. This parameter might be a *radius ratio*, given by

$$\chi_s \equiv \frac{R_{\perp,s}}{R_{\perp,1}} < 1. \tag{3.7}$$

Other parameters of interface s may then be calculated at will:

$$R_{\perp,s} = \chi_s R_{\perp,1} \tag{3.8}$$

$$R_{\parallel,s} = \sqrt{a^2 + \chi_s^2 R_{\perp,1}^2} = \sqrt{R_{\parallel,1}^2 - (1-\chi_s^2)\, R_{\perp,1}^2} \tag{3.9}$$

$$t_r^{(s)} = \frac{t_r^{(1)}}{\chi_s} \tag{3.10}$$

$$\xi_{0,s} = \chi_s \xi_{0,1} = \chi_s \frac{R_{\perp,1}}{\sqrt{R_{\parallel,1}^2 - R_{\perp,1}^2}}. \tag{3.11}$$

The number of different media (N) depends on the truncation ratios, considering that the substrate potentially separates the spheroids in two. Without considering truncation, there are $S + 2$ media: One for each interface, in addition to the ambient and the substrate. When letting the substrate surface enter the island, one gets an additional medium for each spheroidal interface where $|t_r^{(s)}| < 1$, *i.e.* where $\chi_s > |t_r^{(1)}|$. This means that generally the number of media N satisfies

$$S + 2 \leq N \leq 2S + 2. \tag{3.12}$$

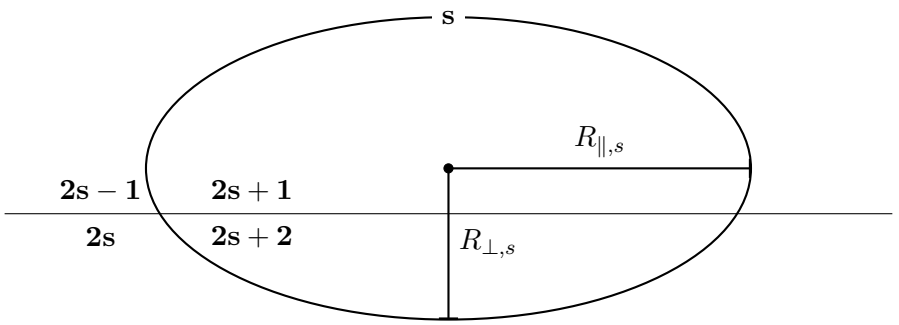

Figure 3.3.: Illustration of how the numbering of media relates to the numbering of their separating spheroidal interface.

Figure 3.2 illustrates a case where $N = 2S + 2$.

3.3. Oblate spheroidal coordinate system

When solving differential equations with boundary conditions on spheroids, as will be the case here, it can be helpful to use a *spheroidal coordinate system*. One such oblate spheroidal coordinate system has variables (ξ, η, ϕ) which map to the Cartesian coordinates (x, y, z) as [17]

$$\begin{aligned} x &= a\left[(1+\xi^2)(1-\eta^2)\right]^{1/2}\cos\phi \\ y &= a\left[(1+\xi^2)(1-\eta^2)\right]^{1/2}\sin\phi \\ z &= a\xi\eta. \end{aligned} \tag{3.13}$$

The inverse of this transformation is [17]

$$\xi = \left[\left(\frac{\rho_1+\rho_2}{2a}\right)^2 - 1\right]^{1/2}, \tag{3.14}$$

$$\eta = \pm\left[1 - \left(\frac{\rho_1-\rho_2}{2a}\right)^2\right]^{1/2}, \tag{3.15}$$

$$\phi = \arctan\left(\frac{y}{x}\right), \tag{3.16}$$

where ρ_1 and ρ_2 are given by

$$\begin{aligned} \rho_1 &\equiv \sqrt{z^2 + (x + a\cos\phi)^2 + (y + a\sin\phi)^2} \\ \rho_2 &\equiv \sqrt{z^2 + (x - a\cos\phi)^2 + (y - \sin\phi)^2}. \end{aligned} \tag{3.17}$$

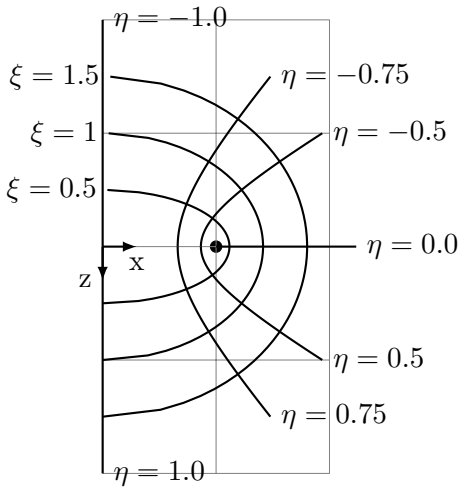

Figure 3.4.: Illustration of an oblate spheroidal coordinate system with the focal point parameter $a = 1$. The azimuth angle ϕ is simply kept at zero, although a figure with constant ϕ would be identical at any value because of symmetry. The surfaces of constant ξ form oblate spheroids all with the same focal ring of radius a. The surfaces of constant η form halves of two-sheet hyperboloids. Note how the lines of constant ξ are always perpendicular to the lines of constant η, making it an orthogonal coordinate system.

See Fig. 3.4 for an illustration of this coordinate system. The positive sign in Eq.(3.15) should be used if $z > 0$ and the negative sign if $z < 0$. The spheroidal coordinates have the following domain:

$$\begin{aligned} 0 \leq\ & \xi < \infty \\ -1 \leq\ & \eta \leq 1 \\ 0 \leq\ & \phi < 2\pi. \end{aligned} \tag{3.18}$$

The value of a is a parameter of this coordinate system. As mentioned, surfaces of constant ξ are spheroids, and all of them share the same focal ring of radius a. Spheroids of with a different focal ring will not be of constant ξ in this coordinate system. They will be surfaces of constant ξ in a new system with the the parameter a set to its radius of focus however.

An important property of a coordinate transformation is how an infinitesimal distance $\mathrm{d}s^2$ depends on infinitesimal changes in the new coordinates. This can be expressed in terms of the *metric tensor* as follows:

$$\mathrm{d}s^2 = g_{\xi\xi}\mathrm{d}\xi^2 + g_{\eta\eta}\mathrm{d}\eta^2 + g_{\phi\phi}\mathrm{d}\phi^2, \tag{3.19}$$

where the diagonal elements of the *metric tensor* are found to be [26]

$$g_{\xi\xi} = h_\xi^2 = \left(\frac{\partial x}{\partial \xi}\right)^2 + \left(\frac{\partial y}{\partial \xi}\right)^2 + \left(\frac{\partial z}{\partial \xi}\right)^2 = a^2 \frac{\xi^2 + \eta^2}{1 + \xi^2} \tag{3.20}$$

$$g_{\eta\eta} = h_\eta^2 = \left(\frac{\partial x}{\partial \eta}\right)^2 + \left(\frac{\partial y}{\partial \eta}\right)^2 + \left(\frac{\partial z}{\partial \eta}\right)^2 = a^2 \frac{\xi^2 + \eta^2}{1 - \eta^2} \tag{3.21}$$

$$g_{\phi\phi} = h_\phi^2 = \left(\frac{\partial x}{\partial \phi}\right)^2 + \left(\frac{\partial y}{\partial \phi}\right)^2 + \left(\frac{\partial z}{\partial \phi}\right)^2 = a^2 \left(1 + \xi^2\right)\left(1 - \eta^2\right). \tag{3.22}$$

Here h_{q_i} is the *scale factor* of coordinate q_i. All off-diagonal entries of the metric tensor are zero, since the spheroidal coordinates are orthogonal.

In the upcoming derivations it will be necessary to specify the positions of the boundaries between the media in the new set of coordinates. The boundaries seen in Fig. 3.1 are given by [17]

$$\begin{aligned}
\Omega_{1,3}: &\quad \xi = \xi_0, \quad -1 \leq \eta \leq t_r \\
\Omega_{2,4}: &\quad \xi = \xi_0, \quad t_r \leq \eta \leq 1 \\
\Omega_{1,2}: &\quad \eta = \frac{\xi_0 t_r}{\xi}, \quad \xi_0 \leq \xi \leq \infty \\
\Omega_{3,4}: &\quad \eta = \frac{\xi_0 t_r}{\xi}, \quad \xi_0 |t_r| \leq \xi \leq \xi_0,
\end{aligned} \tag{3.23}$$

where $\Omega_{i,j}$ is the boundary between medium i and medium j.

Expressing the normal derivative of the substrate surface in the new coordinates will also be needed. Given that the z-axis is by definition normal to the substrate surface, this derivative is simply the derivative with respect to z, which can be found to be:

$$\begin{aligned}
\frac{\partial}{\partial z} &= \frac{\partial \xi}{\partial z}\frac{\partial}{\partial \xi} + \frac{\partial \eta}{\partial z}\frac{\partial}{\partial \eta} + \frac{\partial \phi}{\partial z}\frac{\partial}{\partial \phi} \\
&= \frac{\eta}{a}\left(\frac{1 + \xi^2}{\xi^2 + \eta^2}\right)\frac{\partial}{\partial \xi} + \frac{\xi}{a}\left(\frac{1 - \eta^2}{\xi^2 + \eta^2}\right)\frac{\partial}{\partial \eta}.
\end{aligned} \tag{3.24}$$

More than one spheroidal coordinate system will be used in the upcoming derivations, but they will all have a common z-axis, orientation and parameter a. In other words they are identical except for having their origins displaced a distance Δz along the z-axis. This means that the coordinate z' in the displaced system is given by $z' = z - \Delta z$, while $x' = x$ and $y' = y$. The question is how the spheroidal coordinates in such a displaced coordinate system will relate to the spheroidal coordinates in the main coordinate system. Since they have equal z-axes and orientations, ϕ' is simply equal to ϕ. The relations for

the other two parameters are more complicated though, and are given by [17]

$$\xi'[\Delta z, a](\xi,\eta) = \frac{\xi}{\sqrt{2}}\Bigg\{1 + \left(\frac{\Delta z}{a\xi}\right)^2 - 2\frac{\Delta z}{a\xi}\eta - \frac{\eta^2}{\xi^2} + \left[\left(1 + \left(\frac{\Delta z}{a\xi}\right)^2 - 2\frac{\Delta z}{a\xi}\eta - \frac{\eta^2}{\xi^2}\right)^2 + \frac{4}{\xi^2}\left(\frac{\Delta z}{a\xi} - \eta\right)^2\right]^{1/2}\Bigg\}^{1/2}, \tag{3.25}$$

and

$$\eta'[\Delta z, a](\xi,\eta) = \sqrt{2}\left(\eta - \frac{\Delta z}{a\xi}\right)\Bigg\{1 + \left(\frac{\Delta z}{a\xi}\right)^2 - 2\frac{\Delta z}{a\xi}\eta - \frac{\eta^2}{\xi^2} + \left[\left(1 + \left(\frac{\Delta z}{a\xi}\right)^2 - 2\frac{\Delta z}{a\xi}\eta - \frac{\eta^2}{\xi^2}\right)^2 + \frac{4}{\xi^2}\left(\frac{\Delta z}{a\xi} - \eta\right)^2\right]^{1/2}\Bigg\}^{-1/2}. \tag{3.26}$$

3.4. Finding the polarizabilities

If the sizes of the islands are small compared to the wavelength of the incident radiation, one may neglect retardation effects. This allows one to work in the quasi-static limit when calculating the polarizabilities of the film, *i.e.* one can use the Laplace equation as a starting point [17]:

$$\nabla^2\psi(\mathbf{r}) = 0, \tag{3.27}$$

where ψ is the electrostatic potential, which is related to the electrostatic field $\mathbf{E}$ by

$$\mathbf{E}(\mathbf{r}) = -\nabla\psi(\mathbf{r}). \tag{3.28}$$

The Laplace equation (3.27) will need to be solved for a system such as the one shown in Fig. 3.2 in the case of an externally applied homogeneous electric field. At the boundaries between the different materials, care must be taken to satisfy the boundary conditions implied by Maxwell's equations (2.1) in the electrostatic limit. These can be formulated as

$$\psi_i(\mathbf{r}) = \psi_j(\mathbf{r}) \tag{3.29a}$$

$$\epsilon_i(\omega)\partial_n\psi_i(\mathbf{r}) = \epsilon_j(\omega)\partial_n\psi_j(\mathbf{r}) \tag{3.29b}$$

$$\forall\ \mathbf{r} \in \partial\Omega_{ij},$$

where ψ_k is the electrostatic potential for region k, ϵ_k is the complex dielectric function of region k, $\partial\Omega_{ij}$ is the boundary between medium i and medium j, and ∂_n is the normal derivative at this boundary. Equation (3.29) should be made valid at all the boundaries between different homogeneous media.

3.4.1. General solution of Laplace's equation

It turns out that Laplace's equation (3.27) is separable in the spheroidal coordinates described in Sec. 3.3, giving two kinds of general solutions [17]:

$$P_\ell^m(i\xi)Y_\ell^m(\arccos\eta,\phi) \tag{3.30}$$

and

$$Q_\ell^m(i\xi)Y_\ell^m(\arccos\eta,\phi), \tag{3.31}$$

where in both cases ℓ and m can attain the following values:

$$\begin{aligned} \ell &= 0, 1, 2, ... \\ m &= 0, \pm1, \pm2, ... \pm\ell. \end{aligned} \tag{3.32}$$

The functions P_ℓ^m are *associated Legendre functions of the first kind*, of degree ℓ and order m, and are given by [17]

$$P_\ell^m(z) \equiv \frac{(1-z^2)^{m/2}}{2^\ell \ell!}\left(\frac{\mathrm{d}}{\mathrm{d}z}\right)^{\ell+m}(z^2-1)^\ell \tag{3.33}$$

for $m \geq 0$, and

$$P_\ell^m(z) = (-1)^m\frac{(\ell+m)!}{(\ell-m)!}P_\ell^{-m}(z) \tag{3.34}$$

for $m < 0$. These functions have the following symmetry property:

$$P_\ell^m(-z) = (-1)^{\ell+m}P_\ell^m(z). \tag{3.35}$$

Along the imaginary axis one has

$$P_\ell^m(i\xi) = (-1)^m i^{\ell+m}\frac{\left(1+\xi^2\right)^{m/2}}{2^\ell\ell!}\left(\frac{\mathrm{d}}{\mathrm{d}\xi}\right)^{\ell+m}\left(\xi^2+1\right)^\ell. \tag{3.36}$$

The functions Q_ℓ^m are *associated Legendre functions of the second kind*, of degree ℓ and order m, and are along the imaginary axis given by [17]

$$\begin{aligned} Q_\ell^m(i\xi) = (-1)^{m+1}i^{\ell+1}&\frac{\left(1+\xi^2\right)^{m/2}}{2^\ell\ell!}\left(\frac{\mathrm{d}}{\mathrm{d}\xi}\right)^m \\ &\left\{2\left(\frac{\mathrm{d}}{\mathrm{d}\xi}\right)^\ell \arctan\left(\frac{1}{\xi}\right)(1+\xi^2)^\ell - \arctan\left(\frac{1}{\xi}\right)\left(\frac{\mathrm{d}}{\mathrm{d}\xi}\right)^\ell(1+\xi^2)^\ell\right\} \end{aligned} \tag{3.37}$$

for $m \leq 0$, and

$$Q_\ell^m(i\xi) = \frac{(\ell+m)!}{(\ell-m)!} Q_\ell^{-m}(i\xi) \tag{3.38}$$

for $m < 0$. The functions Q_ℓ^m will not be needed outside the imaginary axis here.

The functions Y_ℓ^m are the *spherical harmonics*, given by [17]

$$Y_\ell^m(\arccos\eta, \phi) \equiv \left[\frac{2\ell+1}{4\pi}\frac{(\ell-m)!}{(\ell+m)!}\right]^{1/2} P_\ell^m(\eta)(-1)^m e^{im\phi} \tag{3.39}$$

Using Eq. (3.35) they can be shown to have the following symmetry property for the coordinate η:

$$Y_\ell^m(\arccos[-\eta], \phi) = (-1)^{\ell+m} Y_\ell^m(\arccos\eta, \phi) \tag{3.40}$$

The spherical harmonics Y_ℓ^m form an orthonormal set [17], such that

$$\int_{-1}^{1} \mathrm{d}\eta \int_0^{2\pi} \mathrm{d}\phi \left[Y_\ell^m(\arccos\eta, \phi)\right]^* Y_{\ell'}^{m'}(\arccos\eta, \phi) = \delta_{\ell\ell'}\delta_{mm'} \tag{3.41}$$

where δ_{ij} is the Kronecker delta. It will also often be used that

$$\int_0^{2\pi} \mathrm{d}\phi \left[Y_\ell^m(\arccos\eta, \phi)\right]^* Y_{\ell'}^{m'}(\arccos\eta', \phi) = \delta_{mm'}\zeta_{\ell\ell'}^m P_\ell^m(\eta) P_{\ell'}^{m'}(\eta'), \tag{3.42}$$

which follows from the orthogonality relation

$$\int_0^{2\pi} \mathrm{d}\phi \ \mathrm{e}^{i(m'-m)\phi} = 2\pi\delta_{m'm}. \tag{3.43}$$

The quantity $\zeta_{\ell\ell'}^m$ is defined by:

$$\zeta_{\ell\ell'}^m \equiv \frac{1}{2}\sqrt{\frac{(2\ell+1)(2\ell'+1)(\ell-m)!(\ell'-m)!}{(\ell+m)!(\ell'+m)!}}. \tag{3.44}$$

The prime on η' indicates that it may belong to a different spheroidal coordinate system than η.

For convenience the following two functions will be introduced as part of the general solutions:

$$X_\ell^m(\xi, a) \equiv i^{m-\ell}\frac{(\ell-m)!}{(2\ell-1)!!} a^\ell P_\ell^m(i\xi) \tag{3.45}$$

and

$$Z_\ell^m(\xi, a) \equiv i^{\ell+1}\frac{(2\ell+1)!!}{(\ell+m)!} a^{-\ell-1} Q_\ell^m(i\xi), \tag{3.46}$$

where $(n)!!$ is the *double factorial* given by

$$(n)!! = \begin{cases} 1 \cdot 3 \cdot 5 \cdot ... \cdot (n-2) \cdot n & \text{odd } n > 0 \\ 2 \cdot 4 \cdot 6 \cdot ... \cdot (n-2) \cdot n & \text{even } n > 0 \\ 1 & n = -1, 0 \end{cases}. \tag{3.47}$$

By inspecting Eqs. (3.36) and (3.37) one can see that X_ℓ^m and Z_ℓ^m will always be real. There are many ways to define functions of P_ℓ^m and Q_ℓ^m which are guaranteed to be real however, so why exactly these definitions? It turns out that in the spherical limit ($\xi \to \infty,\ a \to 0,\ a\xi \to r$), the asymptotic behaviors of $X_\ell^m(\xi, a)$ and $Z_\ell^m(\xi, a)$ are [17]

$$\begin{aligned} X_\ell^m(\xi, a) &\simeq r^\ell \\ Z_\ell^m(\xi, a) &\simeq r^{-\ell-1}, \end{aligned} \tag{3.48}$$

which can be recognized as the radial parts of a *spherical* multipole expansion [17]. Using these functions X_ℓ^m and Z_ℓ^m as the "radial" (ξ dependent) part of the spheroidal multipole expansion thus allows similar interpretation of the multipole coefficients as in the spherical case, without needing to convert via some ℓ and m dependent factor.

Solutions of the first kind (3.30), on the form of $X_\ell^m(\xi, a)Y_\ell^m(\arccos\eta, \phi)$, satisfy the Laplace equation (3.27) everywhere, but do not approach zero as $\xi \to \infty$. These kinds of solutions may then not be used to represent the potential in media where ξ is limitless, *i.e.* in the ambient or the substrate. Solutions of the second kind (3.31), on the form of $Z_\ell^m(\xi, a)Y_\ell^m(\arccos\eta, \phi)$, reach zero as $\xi \to \infty$, but satisfy the Laplace equation only for $\xi > 0$ [17]. These kinds of solutions may then not be used to represent the potential in media containing the origin of the coordinate system used.

The question now is how one should proceed to use these general solutions to construct a correct solution for the problem at hand. The Laplace equation (3.27) is linear and homogeneous, and thus any linear combination of the terms in Eqs. (3.30) and (3.31) are also guaranteed to be solutions. The potential in each homogeneous region may then be represented as a linear combination of all possible general solution terms. The task is then to figure out what the coefficients in the linear combinations need to be in order to satisfy the boundary conditions (3.29) at all boundaries between the regions. For the potential representing the polarization response of the island one would also require that it is finite everywhere, as well as approaching zero as one moves infinitely far away from the island. The only potentials allowed to be nonzero far away from the island are the ones representing the incoming and transmitted homogeneous electric fields.

A linear combination of the general solutions in Eqs. (3.30) and (3.31) is called a *spheroidal multipole expansion* [17], which is said to have its source at

the origin of the coordinate system used in this particular expansion. Such a source will be called a *spheroidal multipole*. Two such multipoles will be used to represent the response of the system, both restricted to be placed along the z-axis: One is placed somewhere inside the island, and represents the potential due to its induced charge distribution. This multipole is labelled μ. The other is placed at the mirror point of the first one across the substrate surface, and represents the image charge distribution induced in the substrate below the island. This multipole is labelled $\bar{\mu}$. In terms of the main coordinate system with its origin at the center of the spheroidal island, multipole μ is located at

$$\mathbf{P}_\mu = (0, 0, \mu_z). \tag{3.49}$$

The second multipole must then be located at

$$\mathbf{P}_{\bar{\mu}} = (0, 0, \bar{\mu}_z) = (0, 0, 2d - \mu_z), \tag{3.50}$$

which is valid for both positive and negative μ_z. Each multipole will have its

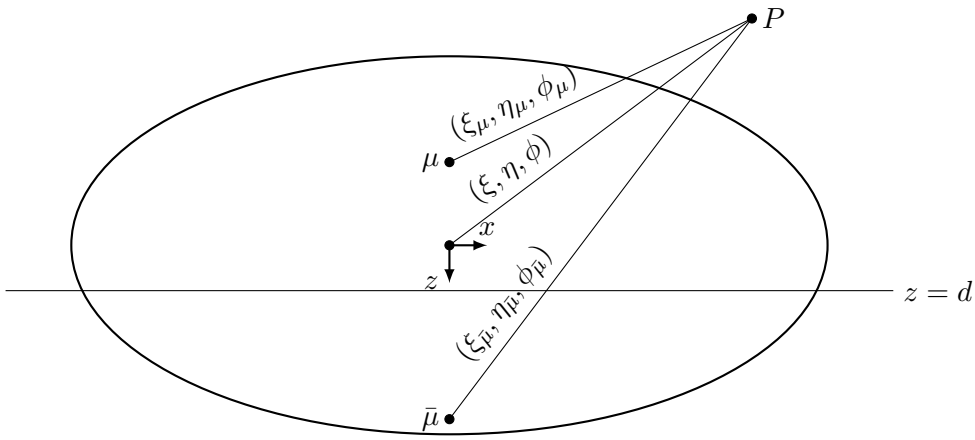

Figure 3.5.: Illustration of the three coordinate systems used, indicating the different sets of coordinates used to represent the same point P. The main coordinate system (ξ, η, ϕ) has its origin at the center of the spheroids. A different coordinate system μ $(\xi_\mu, \eta_\mu, \phi)$ has its origin at $z = \mu_z$, which is the position of the multipole in the island. Equidistant from the substrate surface is another coordinate system $\bar{\mu}$ $(\xi_{\bar{\mu}}, \eta_{\bar{\mu}}, \phi_{\bar{\mu}})$ with its origin at $z = 2d - \mu_z$, which is the position of the image multipole. Note that because all three coordinate systems share the same z-axis, $\phi_{\bar{\mu}} = \phi_\mu = \phi$.

own spheroidal coordinate system with the same label. For an illustration of

the three coordinate systems, see Fig. 3.5. As shown, the same point P will of course be specified by different values for the coordinates depending on the coordinate system. In the main coordinate system it is specified by (ξ, η, ϕ), in the μ coordinate system it is specified by $(\xi_\mu, \eta_\mu, \phi_\mu)$, while in the $\bar{\mu}$ coordinate system it is specified by $(\xi_{\bar{\mu}}, \eta_{\bar{\mu}}, \phi_{\bar{\mu}})$. All three coordinate systems share the same parameter a. The different coordinates for the same point are related in the following way:

$$\begin{aligned}
\xi_\mu &= \xi'[\Delta z = \mu_z, a](\xi, \eta) \\
\xi_{\bar{\mu}} &= \xi'[\Delta z = 2d - \mu_z, a](\xi, \eta) \\
\eta_\mu &= \eta'[\Delta z = \mu_z, a](\xi, \eta) \\
\eta_{\bar{\mu}} &= \eta'[\Delta z = 2d - \mu_z, a](\xi, \eta) \\
\phi_\mu &= \phi_{\bar{\mu}} = \phi
\end{aligned} \tag{3.51}$$

where $\xi'[\Delta z, a](\xi, \eta)$ and $\eta'[\Delta z, a](\xi, \eta)$ are given by Eqs. (3.25) and (3.26).

In some cases intermediate results will be derived generally for both μ and $\bar{\mu}$. In these cases the symbol κ will be used as a generic placeholder, which should be replaced by either μ or $\bar{\mu}$ when applying the expressions.

A general solution of Laplace's equation (3.27) in any region i above the substrate surface may now be written as

$$\begin{aligned}
\psi_i(\mathbf{r}) = \psi_0^{(i)} &\\
&+ {\sum_{\ell m}}' \left[A_{\ell m}^{(i)} Z_\ell^m(\xi_\mu, a) + B_{\ell m}^{(i)} X_\ell^m(\xi_\mu, a) \right] Y_\ell^m(\arccos \eta_\mu, \phi_\mu) \\
&+ {\sum_{\ell m}}' \left[\bar{A}_{\ell m}^{(i)} Z_\ell^m(\xi_{\bar{\mu}}, a) + \bar{B}_{\ell m}^{(i)} X_\ell^m(\xi_{\bar{\mu}}, a) \right] Y_\ell^m(\arccos \eta_{\bar{\mu}}, \phi_{\bar{\mu}}) \\
&+ \delta_{i,1} \psi_{\text{inc}}(\xi, \eta, \phi),
\end{aligned} \tag{3.52}$$

where i must be odd, according to the numbering convention illustrated in Fig. 3.3. The prime on top of the summations denotes the exclusion of the $\ell = 0$ term in the sum. This may be done because the total charge of the system is assumed to be zero [17]. Besides this, ℓ and m in the summations follow the rules of Eq. (3.32), such that they in principle go to infinite ℓ. This solution is a linear combination of multipole terms from both multipole μ and multipole $\bar{\mu}$, with unknown coefficients $A_{\ell m}^{(i)}$, $B_{\ell m}^{(i)}$, $\bar{A}_{\ell m}^{(i)}$ and $\bar{B}_{\ell m}^{(i)}$. It also adds the potential corresponding to the applied homogeneous electric field (ψ_{inc}) in the case when $i = 1$, *i.e.* when ψ_i is the potential in the ambient outside the island.

A general solution of Laplace's equation (3.27) in any region $i+1$ below the

substrate surface may now be written as

$$\begin{aligned}\psi_{i+1}(\mathbf{r}) = \psi_0^{(i+1)} \\ &+ \sum_{\ell m}{}' \left[A_{\ell m}^{(i+1)} Z_\ell^m(\xi_\mu, a) + B_{\ell m}^{(i+1)} X_\ell^m(\xi_\mu, a) \right] Y_\ell^m(\arccos \eta_\mu, \phi_\mu) \\ &+ \delta_{i,1} \psi_{\mathrm{tr}}(\xi, \eta, \phi). \end{aligned} \tag{3.53}$$

This solution is a linear combination of multipole terms from multipole μ only, with unknown coefficients $A_{\ell m}^{(i+1)}$ and $B_{\ell m}^{(i+1)}$. It also adds the potential corresponding to the transmitted homogeneous electric field (ψ_{tr}) in the case when $i = 1$, *i.e.* when ψ_{i+1} is the potential in the substrate outside the island. Multipole $\bar{\mu}$ is not a part of this solution, as by the principles of the *image method* [27], virtual image charges should not be used to represent the potential in the region where these image charges are located. In both Eqs. (3.52) and (3.53), be aware of the fact that the variables may belong to different coordinate systems, depending on the subscript or lack thereof.

If the form of the general solutions in Eqs. (3.52) and (3.53) seem somewhat unjustified and arbitrary, note the following: The goal is to find functions which are solutions to Laplace's equation (3.27) in all regions of the geometry, while satisfying the necessary boundary conditions (3.29) at all interfaces. The *uniqueness theorem* [27] guarantees that there is only one unique function which satisfy these requirements. Therefore, if one by some trick or clever guess is able to discover such a function, it must be the correct solution. Hence, the form of the general solutions here do not really have to be justified. If they were missing some crucial term, one would not end up with an incorrect solution, one would simply not be able to satisfy all the boundary conditions.

The multipoles μ and $\bar{\mu}$ could in principle be placed anywhere, but constraining them as done here might make the solution converge at lower multipole orders. Within the z-axis constraint, some positions might also give better convergence than others. Requiring $\bar{\mu}$ to be at the mirror point of μ makes it especially simple to satisfy the boundary conditions at the substrate surface, as will be shown in the next section.

3.4.2. Boundary conditions at the substrate surface

First one can attempt to satisfy the boundary conditions (3.29) at the flat $z = d$ boundaries between mediums i and $i + 1$ (i odd). The potentials ψ_{inc} and ψ_{tr} should alone satisfy these conditions by definition, and thus they might be eliminated immediately. For all points on the plane equidistant from the

coordinate systems μ and $\bar{\mu}$ (the substrate surface), we have the relations

$$\begin{aligned}
\xi_{\bar{\mu}} &= \xi_{\mu} \\
\eta_{\bar{\mu}} &= -\,\eta_{\mu} \\
\phi_{\bar{\mu}} &= \phi_{\mu} \\
&\text{when } z = d.
\end{aligned} \tag{3.54}$$

Using Eqs. (3.40), (3.54), and the linear independence of the general solution terms in Eqs. (3.52) and (3.53), satisfying the boundary condition in (3.29a) leads to the following relations:

$$\begin{aligned}
\psi_0^{(i+1)} &= \psi_0^{(i)} \\
A_{\ell m}^{(i+1)} &= A_{\ell m}^{(i)} + (-1)^{\ell+m} \bar{A}_{\ell m}^{(i)} \\
B_{\ell m}^{(i+1)} &= B_{\ell m}^{(i)} + (-1)^{\ell+m} \bar{B}_{\ell m}^{(i)}.
\end{aligned} \tag{3.55}$$

Another set of relations between the coefficients can be found by satisfying the boundary condition in (3.29b). Using Eqs. (3.24), (3.40) and (3.54) one finds that

$$\begin{aligned}
&\frac{\partial}{\partial z}\left[Z_\ell^m(\xi_{\bar{\mu}}, a) Y_\ell^m(\arccos \eta_{\bar{\mu}}, \phi_{\bar{\mu}})\right]\big|_{z=d} \\
&= (-1)(-1)^{\ell+m} \frac{\partial}{\partial z}\left[Z_\ell^m(\xi_{\mu}, a) Y_\ell^m(\arccos \eta_{\mu}, \phi_{\mu})\right]\big|_{z=d} \\
&\frac{\partial}{\partial z}\left[X_\ell^m(\xi_{\bar{\mu}}, a) Y_\ell^m(\arccos \eta_{\bar{\mu}}, \phi_{\bar{\mu}})\right]\big|_{z=d} \\
&= (-1)(-1)^{\ell+m} \frac{\partial}{\partial z}\left[X_\ell^m(\xi_{\mu}, a) Y_\ell^m(\arccos \eta_{\mu}, \phi_{\mu})\right]\big|_{z=d}.
\end{aligned} \tag{3.56}$$

Combining Eq. (3.56) with the linear independence of terms appearing in Eqs. (3.52) and (3.53), one finds the addition set of relations to be

$$\begin{aligned}
\epsilon_{i+1} A_{\ell m}^{(i+1)} &= \epsilon_i A_{\ell m}^{(i)} - (-1)^{\ell+m} \epsilon_i \bar{A}_{\ell m}^{(i)}, \\
\epsilon_{i+1} B_{\ell m}^{(i+1)} &= \epsilon_i B_{\ell m}^{(i)} - (-1)^{\ell+m} \epsilon_i \bar{B}_{\ell m}^{(i)}.
\end{aligned} \tag{3.57}$$

Equations (3.55) and (3.57) may now be combined into the following relations

$$\begin{aligned}
\bar{A}_{\ell m}^{(i)} &= (-1)^{\ell+m} \frac{\epsilon_i - \epsilon_{i+1}}{\epsilon_i + \epsilon_{i+1}} A_{\ell m}^{(i)}, \\
A_{\ell m}^{(i+1)} &= \frac{2\epsilon_i}{\epsilon_i + \epsilon_{i+1}} A_{\ell m}^{(i)}, \\
\bar{B}_{\ell m}^{(i)} &= (-1)^{\ell+m} \frac{\epsilon_i - \epsilon_{i+1}}{\epsilon_i + \epsilon_{i+1}} B_{\ell m}^{(i)}, \\
B_{\ell m}^{(i+1)} &= \frac{2\epsilon_i}{\epsilon_i + \epsilon_{i+1}} B_{\ell m}^{(i)},
\end{aligned} \tag{3.58}$$

thus reducing the unknown coefficients to only $A_{\ell m}^{(i)}$ and $B_{\ell m}^{(i)}$, with only odd i. Beware that these relations, and the relation from the top of Eq. (3.55) ($\psi_0^{(i+1)} = \psi_0^{(i)}$), may only be used when i and $i+1$ refer to neighboring media separated by the flat substrate surface. In other words they only apply when i is odd, according to the numbering convention for media introduced in Sec. 3.2. The general solutions in Eqs. (3.52) and (3.53) may now be rewritten in terms of only the remaining unknown coefficients:

$$\begin{aligned}\psi_i(\mathbf{r}) = \psi_0^{(i)} &\\ &+ {\sum_{\ell m}}' A_{\ell m}^{(i)} \Big[Z_\ell^m(\xi_\mu, a) Y_\ell^m(\arccos\eta_\mu, \phi_\mu) \\ &\qquad + (-1)^{\ell+m} \mathcal{R}_i Z_\ell^m(\xi_{\bar{\mu}}, a) Y_\ell^m(\arccos\eta_{\bar{\mu}}, \phi_{\bar{\mu}}) \Big] \\ &+ {\sum_{\ell m}}' B_{\ell m}^{(i)} \Big[X_\ell^m(\xi_\mu, a) Y_\ell^m(\arccos\eta_\mu, \phi_\mu) \\ &\qquad + (-1)^{\ell+m} \mathcal{R}_i X_\ell^m(\xi_{\bar{\mu}}, a) Y_\ell^m(\arccos\eta_{\bar{\mu}}, \phi_{\bar{\mu}}) \Big] \\ &+ \delta_{i,1} \psi_{\mathrm{inc}}(\xi, \eta, \phi),\end{aligned} \tag{3.59}$$

and

$$\begin{aligned}\psi_{i+1}(\mathbf{r}) = \psi_0^{(i+1)} &\\ &+ \mathcal{T}_i {\sum_{\ell m}}' \left[A_{\ell m}^{(i)} Z_\ell^m(\xi_\mu, a) + B_{\ell m}^{(i)} X_\ell^m(\xi_\mu, a) \right] Y_\ell^m(\arccos\eta_\mu, \phi_\mu) \\ &+ \delta_{i,1} \psi_{\mathrm{tr}}(\xi, \eta, \phi),\end{aligned} \tag{3.60}$$

where

$$\mathcal{R}_i \equiv \frac{\epsilon_i - \epsilon_{i+1}}{\epsilon_i + \epsilon_{i+1}}, \tag{3.61}$$

and

$$\mathcal{T}_i \equiv \frac{2\epsilon_i}{\epsilon_i + \epsilon_{i+1}}. \tag{3.62}$$

3.4.3. Boundary conditions at the spheroidal interfaces

What remains now is to find the coefficients $A_{\ell m}^{(i)}$ and $B_{\ell m}^{(i)}$ which make the general solutions in Eqs. (3.59) and (3.60) satisfy the boundary conditions (3.29) at every spheroidal interface $s = 1, ..., S$.

While the boundary conditions should in principle be satisfied at every single point on the spheroids, one may instead try to impose the *weak formulation* of these conditions [17]. This implies not strictly demanding that the boundary

conditions in Eq. (3.29) are satisfied everywhere at the boundaries, but instead demanding that integrals of these conditions multiplied by a *test function* are satisfied. The integrals are made across the entire spheroidal interface, but will have to be separated into parts above and below the substrate surface:

$$\int_{\bigcirc_s} = \int_{\bigcap_s} + \int_{\bigcup_s}, \tag{3.63}$$

where $\bigcirc_s$ indicates integration over the entire spheroidal interface s, while $\bigcap_s$ and $\bigcup_s$ are its parts above and below the substrate surface respectively.

The test functions for this weak formulation will be the complex conjugated spherical harmonics $Y_\ell^m(\arccos\eta, \phi)^*$ centered at the origin of the main coordinate system. The conditions should be satisfied for all spherical harmonics, with ℓ and m obeying the rules in Eq. (3.32). The integrals used in this weak formulation will be

$$\begin{aligned}
\int_{\bigcirc_s} &= \int_{-1}^{1} \mathrm{d}\eta \int_0^{2\pi} \mathrm{d}\phi \\
\int_{\bigcap_s} &= \int_{-1}^{t_r^{(s)}} \mathrm{d}\eta \int_0^{2\pi} \mathrm{d}\phi \\
\int_{\bigcup_s} &= \int_{t_r^{(s)}}^{1} \mathrm{d}\eta \int_0^{2\pi} \mathrm{d}\phi,
\end{aligned} \tag{3.64}$$

which allows the convenient use of the orthonormal property of the test functions, as seen in Eq. (3.41), and the relation displayed in Eq. (3.42). The limits of integration for the last two integrals were found using Eq. (3.23).

First boundary condition

The weak formulation of the boundary condition in Eq. (3.29a) may be written as

$$\begin{aligned}
&\int_{-1}^{t_r^{(s)}} \mathrm{d}\eta \int_0^{2\pi} \mathrm{d}\phi \, [Y_\ell^m(\arccos\eta, \phi)]^* \, (\psi_{2s-1} - \psi_{2s+1})|_{\xi=\xi_0} \\
+ &\int_{t_r^{(s)}}^{1} \mathrm{d}\eta \int_0^{2\pi} \mathrm{d}\phi \, [Y_\ell^m(\arccos\eta, \phi)]^* \, (\psi_{2s} - \psi_{2s+2})|_{\xi=\xi_0} = 0 \\
&\forall \quad s = 1, 2, 3, ..., S; \;\; \ell = 0, 1, 2, ...; \;\; m = 0, \pm 1, \pm 2, ..., \pm \ell.
\end{aligned} \tag{3.65}$$

For convenience, dimensionless versions of the functions X and Z are defined, identified by the lack of the parameter a in their parameter list:

$$X_\ell^m(\xi) \equiv X_\ell^m(\xi, a) a^{-\ell}, \tag{3.66}$$

$$Z_\ell^m(\xi) \equiv Z_\ell^m(\xi, a)a^{\ell+1}. \tag{3.67}$$

These functions are part of the definitions of two classes of integrals V and W, which are given by

$$V_{\ell\ell'}^m[\kappa_z, \xi](\eta_1, \eta_2) \equiv \int_{\eta_1}^{\eta_2} \mathrm{d}\eta P_\ell^m(\eta) P_{\ell'}^m(\eta_\kappa(\xi, \eta)) Z_{\ell'}^m(\xi_\kappa(\xi, \eta)), \tag{3.68}$$

and

$$W_{\ell\ell'}^m[\kappa_z, \xi](\eta_1, \eta_2) \equiv \int_{\eta_1}^{\eta_2} \mathrm{d}\eta P_\ell^m(\eta) P_{\ell'}^m(\eta_\kappa(\xi, \eta)) X_{\ell'}^m(\xi_\kappa(\xi, \eta)). \tag{3.69}$$

Here κ is used as a placeholder for either μ or $\bar{\mu}$, indicating the replacement of the coordinates $(\xi_\kappa, \eta_\kappa)$ with either (ξ_μ, η_μ) or $(\xi_{\bar{\mu}}, \eta_{\bar{\mu}})$.

Using Eqs. (3.66) – (3.69) and (3.42), it may now be shown that

$$\int_{\eta_1}^{\eta_2} \mathrm{d}\eta \int_0^{2\pi} \mathrm{d}\phi \, [Y_\ell^m(\arccos\eta, \phi)]^* \, Z_{\ell'}^{m'}(\xi_\kappa, a) Y_{\ell'}^{m'}(\arccos\eta_\kappa, \phi_\kappa)\Big|_{\xi=\xi_{0,s}} = \delta_{mm'}\zeta_{\ell\ell'}^m a^{-\ell'-1} V_{\ell\ell'}^m[\kappa_z, \xi_{0,s}](\eta_1, \eta_2), \tag{3.70}$$

and

$$\int_{\eta_1}^{\eta_2} \mathrm{d}\eta \int_0^{2\pi} \mathrm{d}\phi \, [Y_\ell^m(\arccos\eta, \phi)]^* \, X_{\ell'}^{m'}(\xi_\kappa, a) Y_{\ell'}^{m'}(\arccos\eta_\kappa, \phi_\kappa)\Big|_{\xi=\xi_{0,s}} = \delta_{mm'}\zeta_{\ell\ell'}^m a^{\ell'} W_{\ell\ell'}^m[\kappa_z, \xi_{0,s}](\eta_1, \eta_2). \tag{3.71}$$

Also, since $1 = 2\sqrt{\pi}Y_0^0$, one may by using the orthonormality of spherical harmonics (3.41) show that:

$$\int_{-1}^{1} \mathrm{d}\eta \int_0^{2\pi} \mathrm{d}\phi \, [Y_\ell^m(\,\eta, \phi)]^* \psi_0^{(2s-1)} = 2\sqrt{\pi}\psi_0^{(2s-1)}\delta_{\ell 0}\delta_{m0} \tag{3.72}$$

Inserting the general solutions in Eqs. (3.59) and (3.60) into the left side of the weak formulation of the boundary condition (3.65), while using the

relations in Eqs. (3.70), (3.71) and (3.72), leads to the following equation:

$$
\begin{aligned}
&\int_{-1}^{t_r^{(s)}} \mathrm{d}\eta \int_0^{2\pi} \mathrm{d}\phi \, [Y_\ell^m(\arccos\eta,\phi)]^* \, (\psi_{2s-1} - \psi_{2s+1})|_{\xi=\xi_0} \\
&+ \int_{t_r^{(s)}}^{1} \mathrm{d}\eta \int_0^{2\pi} \mathrm{d}\phi \, [Y_\ell^m(\arccos\eta,\phi)]^* \, (\psi_{2s} - \psi_{2s+2})|_{\xi=\xi_0} \\
&= \; 2\sqrt{\pi}\left[\psi_0^{(2s-1)} - \psi_0^{(2s+1)}\right]\delta_{\ell 0}\delta_{m0} \\
&+ {\sum_{\ell' m'}}' A_{\ell' m'}^{(2s-1)} \delta_{mm'} \zeta_{\ell\ell'}^m a^{-\ell'-1} \Big[V_{\ell\ell'}^m[\mu_z, \xi_{0,s}](-1, t_r^{(s)}) \\
&\quad + (-1)^{\ell'+m} \mathcal{R}_{2s-1} V_{\ell\ell'}^m[\bar{\mu}_z, \xi_{0,s}](-1, t_r^{(s)}) + \mathcal{T}_{2s-1} V_{\ell\ell'}^m[\mu_z, \xi_{0,s}](t_r^{(s)}, 1) \Big] \\
&- {\sum_{\ell' m'}}' A_{\ell' m'}^{(2s+1)} \delta_{mm'} \zeta_{\ell\ell'}^m a^{-\ell'-1} \Big[V_{\ell\ell'}^m[\mu_z, \xi_{0,s}](-1, t_r^{(s)}) \\
&\quad + (-1)^{\ell'+m} \mathcal{R}_{2s+1} V_{\ell\ell'}^m[\bar{\mu}_z, \xi_{0,s}](-1, t_r^{(s)}) + \mathcal{T}_{2s+1} V_{\ell\ell'}^m[\mu_z, \xi_{0,s}](t_r^{(s)}, 1) \Big] \\
&+ {\sum_{\ell' m'}}' B_{\ell' m'}^{(2s-1)} \delta_{mm'} \zeta_{\ell\ell'}^m a^{\ell'} \Big[W_{\ell\ell'}^m[\mu_z, \xi_{0,s}](-1, t_r^{(s)}) \\
&\quad + (-1)^{\ell'+m} \mathcal{R}_{2s-1} W_{\ell\ell'}^m[\bar{\mu}_z, \xi_{0,s}](-1, t_r^{(s)}) + \mathcal{T}_{2s-1} W_{\ell\ell'}^m[\mu_z, \xi_{0,s}](t_r^{(s)}, 1) \Big] \\
&- {\sum_{\ell' m'}}' B_{\ell' m'}^{(2s+1)} \delta_{mm'} \zeta_{\ell\ell'}^m a^{\ell'} \Big[W_{\ell\ell'}^m[\mu_z, \xi_{0,s}](-1, t_r^{(s)}) \\
&\quad + (-1)^{\ell'+m} \mathcal{R}_{2s+1} W_{\ell\ell'}^m[\bar{\mu}_z, \xi_{0,s}](-1, t_r^{(s)}) + \mathcal{T}_{2s+1} W_{\ell\ell'}^m[\mu_z, \xi_{0,s}](t_r^{(s)}, 1) \Big] \\
&+ \delta_{s1} \int_{-1}^{t_r^{(1)}} \mathrm{d}\eta \int_0^{2\pi} \mathrm{d}\phi \, [Y_\ell^m(\arccos\eta,\phi)]^* \, \psi_{\mathrm{inc}}(\xi,\eta,\phi)|_{\xi=\xi_{0,1}} \\
&+ \delta_{s1} \int_{t_r^{(1)}}^{1} \mathrm{d}\eta \int_0^{2\pi} \mathrm{d}\phi \, [Y_\ell^m(\arccos\eta,\phi)]^* \, \psi_{\mathrm{tr}}(\xi,\eta,\phi)|_{\xi=\xi_{0,1}} \, .
\end{aligned}
\tag{3.73}
$$

By introducing shorthands $\mathcal{I}$ and $\mathcal{K}$:

$$
\begin{aligned}
\mathcal{I}_{\ell\ell'}^{m(i)}(t_r, \xi_0) &\equiv \xi_0^{\ell'+1} \Big\{ V_{\ell\ell'}^m[\mu_z, \xi_0](-1, t_r) + (-1)^{\ell'+m} \mathcal{R}_i V_{\ell\ell'}^m[\bar{\mu}_z, \xi_0](-1, t_r) \\
&\qquad + \mathcal{T}_i V_{\ell\ell'}^m[\mu_z, \xi_0](t_r, 1) \Big\} \\
&= \xi_0^{\ell'+1} \mathcal{R}_i \Big[- V_{\ell\ell'}^m[\mu_z, \xi_0](-1, t_r) + (-1)^{\ell'+m} V_{\ell\ell'}^m[\bar{\mu}_z, \xi_0](-1, t_r) \\
&\qquad + \frac{2\epsilon_i}{\epsilon_i - \epsilon_{i+1}} V_{\ell\ell'}^m[\mu_z, \xi_0](-1, 1) \Big],
\end{aligned}
\tag{3.74}
$$

$$\begin{aligned}\mathcal{K}^{m(i)}_{\ell\ell'}(t_r,\xi_0) &\equiv \xi_0^{-\ell'}\Big\{W^m_{\ell\ell'}[\mu_z,\xi_0](-1,t_r)+(-1)^{\ell'+m}\mathcal{R}_i W^m_{\ell\ell'}[\bar{\mu}_z,\xi_0](-1,t_r)\\ &\quad+\mathcal{T}_i W^m_{\ell\ell'}[\mu_z,\xi_0](t_r,1)\Big\}\\ &=\xi_0^{-\ell'}\mathcal{R}_i\Big[-W^m_{\ell\ell'}[\mu_z,\xi_0](-1,t_r)+(-1)^{\ell'+m}W^m_{\ell\ell'}[\bar{\mu}_z,\xi_0](-1,t_r)\\ &\quad+\frac{2\epsilon_i}{\epsilon_i-\epsilon_{i+1}}W^m_{\ell\ell'}[\mu_z,\xi_0](-1,1)\Big],\end{aligned}\tag{3.75}$$

where it in the second step has been used that $1-\mathcal{T}_i=-\mathcal{R}_i$. The weak formulation of the boundary condition (3.65) may now be written as

$$\begin{aligned}&2\sqrt{\pi}\left[\psi_0^{(2s-1)}-\psi_0^{(2s+1)}\right]\delta_{\ell 0}\delta_{m0}\\ &+\sum_{\ell'=|m|}{}'\,\zeta^m_{\ell\ell'}R^{-\ell'-1}_{\perp,s}\left[\mathcal{I}^{m(2s-1)}_{\ell\ell'}(t_r^{(s)},\xi_{0,s})A^{(2s-1)}_{\ell' m}-\mathcal{I}^{m(2s+1)}_{\ell\ell'}(t_r^{(s)},\xi_{0,s})A^{(2s+1)}_{\ell' m}\right]\\ &+\sum_{\ell'=|m|}{}'\,\zeta^m_{\ell\ell'}R^{\ell'}_{\perp,s}\left[\mathcal{K}^{m(2s-1)}_{\ell\ell'}(t_r^{(s)},\xi_{0,s})B^{(2s-1)}_{\ell' m}-\mathcal{K}^{m(2s+1)}_{\ell\ell'}(t_r^{(s)},\xi_{0,s})B^{(2s+1)}_{\ell' m}\right]\\ &+\delta_{s1}\int_{-1}^{t_r^{(1)}}\mathrm{d}\eta\int_0^{2\pi}\mathrm{d}\phi\,[Y^m_\ell(\arccos\eta,\phi)]^*\,\psi_{\mathrm{inc}}(\xi,\eta,\phi)\big|_{\xi=\xi_{0,1}}\\ &+\delta_{s1}\int_{t_r^{(1)}}^{1}\mathrm{d}\eta\int_0^{2\pi}\mathrm{d}\phi\,[Y^m_\ell(\arccos\eta,\phi)]^*\,\psi_{\mathrm{tr}}(\xi,\eta,\phi)\big|_{\xi=\xi_{0,1}}=0\\ &\forall\quad s=1,2,3,...,S;\ \ell=0,1,2,...;\ m=0,\pm1,\pm2,...,\pm\ell.\end{aligned}\tag{3.76}$$

Thus the first boundary condition (3.29a), in the weak formulation, has been reduced to a set of linear equations for the unknown multipole coefficients $A^{(i)}_{\ell m}$ and $B^{(i)}_{\ell m}$ (odd i).

Second boundary condition

Similarly, the weak formulation of the boundary condition in Eq. (3.29b) may be written as:

$$\begin{aligned}&\int_{-1}^{t_r^{(s)}}\mathrm{d}\eta\int_0^{2\pi}\mathrm{d}\phi\,[Y^m_\ell(\arccos\eta,\phi)]^*\left[\frac{\partial}{\partial\xi}\left(\epsilon_{2s-1}\psi_{2s-1}-\epsilon_{2s+1}\psi_{2s+1}\right)\right]\Big|_{\xi=\xi_0}\\ &+\int_{t_r^{(s)}}^{1}\mathrm{d}\eta\int_0^{2\pi}\mathrm{d}\phi\,[Y^m_\ell(\arccos\eta,\phi)]^*\left[\frac{\partial}{\partial\xi}\left(\epsilon_{2s}\psi_{2s}-\epsilon_{2s+2}\psi_{2s+2}\right)\right]\Big|_{\xi=\xi_0}=0\\ &\forall\quad s=1,2,3,...,S;\ \ell=0,1,2,...;\ m=0,\pm1,\pm2,...,\pm\ell.\end{aligned}\tag{3.77}$$

Using Eqs. (3.66) – (3.69) and (3.42), it may be shown that

$$\int_{\eta_1}^{\eta_2} \mathrm{d}\eta \int_0^{2\pi} \mathrm{d}\phi \, [Y_\ell^m(\arccos\eta,\phi)]^* \, \frac{\partial}{\partial \xi} \left\{ Z_{\ell'}^{m'}(\xi_\kappa, a) Y_{\ell'}^{m'}(\arccos\eta_\kappa, \phi_\kappa) \right\} \Big|_{\xi=\xi_{0,s}} = \delta_{mm'} \zeta_{\ell\ell'}^m a^{-\ell'-1} \frac{\partial}{\partial \xi} \left\{ V_{\ell\ell'}^m[\kappa_z, \xi_{0,s}](\eta_1, \eta_2) \right\} \Big|_{\xi=\xi_{0,s}}, \tag{3.78}$$

and

$$\int_{\eta_1}^{\eta_2} \mathrm{d}\eta \int_0^{2\pi} \mathrm{d}\phi \, [Y_\ell^m(\arccos\eta,\phi)]^* \, \frac{\partial}{\partial \xi} \left\{ X_{\ell'}^{m'}(\xi_\kappa, a) Y_{\ell'}^{m'}(\arccos\eta_\kappa, \phi_\kappa) \right\} \Big|_{\xi=\xi_{0,s}} = \delta_{mm'} \zeta_{\ell\ell'}^m a^{\ell'} \frac{\partial}{\partial \xi} \left\{ W_{\ell\ell'}^m[\kappa_z, \xi_{0,s}](\eta_1, \eta_2) \right\} \Big|_{\xi=\xi_{0,s}}. \tag{3.79}$$

Inserting the general solutions in Eqs. (3.59) and (3.60) into the left side of the weak formulation of the boundary condition (3.77), while using the relations

in Eqs. (3.78) and (3.79), leads to the following equation:

$$
\begin{aligned}
&\int_{-1}^{t_r^{(s)}} \mathrm{d}\eta \int_0^{2\pi} \mathrm{d}\phi \, [Y_\ell^m(\arccos\eta,\phi)]^* \left[\frac{\partial}{\partial \xi} \left(\epsilon_{2s-1}\psi_{2s-1} - \epsilon_{2s+1}\psi_{2s+1} \right) \right] \Big|_{\xi=\xi_0} \\
&+ \int_{t_r^{(s)}}^{1} \mathrm{d}\eta \int_0^{2\pi} \mathrm{d}\phi \, [Y_\ell^m(\arccos\eta,\phi)]^* \left[\frac{\partial}{\partial \xi} \left(\epsilon_{2s}\psi_{2s} - \epsilon_{2s+2}\psi_{2s+2} \right) \right] \Big|_{\xi=\xi_0} \\
&= \sum_{\ell' m'}{}' A^{(2s-1)}_{\ell' m'} \delta_{m m'} \zeta^m_{\ell \ell'} a^{-\ell'-1} \Big[\epsilon_{2s-1} \frac{\partial}{\partial \xi} \left\{ V^m_{\ell \ell'}[\mu_z, \xi](-1, t_r^{(s)}) \right\} \Big|_{\xi=\xi_{0,s}} \\
&\quad + \epsilon_{2s-1}(-1)^{\ell'+m} \mathcal{R}_{2s-1} \frac{\partial}{\partial \xi} \left\{ V^m_{\ell \ell'}[\bar{\mu}_z, \xi](-1, t_r^{(s)}) \right\} \Big|_{\xi=\xi_{0,s}} \\
&\quad + \epsilon_{2s} \mathcal{T}_{2s-1} \frac{\partial}{\partial \xi} \left\{ V^m_{\ell \ell'}[\mu_z, \xi](t_r^{(s)}, 1) \right\} \Big|_{\xi=\xi_{0,s}} \Big] \\
&\quad - \sum_{\ell' m'}{}' A^{(2s+1)}_{\ell' m'} \delta_{m m'} \zeta^m_{\ell \ell'} a^{-\ell'-1} \Big[\epsilon_{2s+1} \frac{\partial}{\partial \xi} \left\{ V^m_{\ell \ell'}[\mu_z, \xi](-1, t_r^{(s)}) \right\} \Big|_{\xi=\xi_{0,s}} \\
&\quad + \epsilon_{2s+1}(-1)^{\ell'+m} \mathcal{R}_{2s+1} \frac{\partial}{\partial \xi} \left\{ V^m_{\ell \ell'}[\bar{\mu}_z, \xi](-1, t_r^{(s)}) \right\} \Big|_{\xi=\xi_{0,s}} \\
&\quad + \epsilon_{2s+2} \mathcal{T}_{2s+1} \frac{\partial}{\partial \xi} \left\{ V^m_{\ell \ell'}[\mu_z, \xi](t_r^{(s)}, 1) \right\} \Big|_{\xi=\xi_{0,s}} \Big] \\
&\quad + \sum_{\ell' m'}{}' B^{(2s-1)}_{\ell' m'} \delta_{m m'} \zeta^m_{\ell \ell'} a^{\ell'} \Big[\epsilon_{2s-1} \frac{\partial}{\partial \xi} \left\{ W^m_{\ell \ell'}[\mu_z, \xi](-1, t_r^{(s)}) \right\} \Big|_{\xi=\xi_{0,s}} \\
&\quad + \epsilon_{2s-1}(-1)^{\ell'+m} \mathcal{R}_{2s-1} \frac{\partial}{\partial \xi} \left\{ W^m_{\ell \ell'}[\bar{\mu}_z, \xi](-1, t_r^{(s)}) \right\} \Big|_{\xi=\xi_{0,s}} \\
&\quad + \epsilon_{2s} \mathcal{T}_{2s-1} \frac{\partial}{\partial \xi} \left\{ W^m_{\ell \ell'}[\mu_z, \xi](t_r^{(s)}, 1) \right\} \Big|_{\xi=\xi_{0,s}} \Big] \\
&\quad - \sum_{\ell' m'}{}' B^{(2s+1)}_{\ell' m'} \delta_{m m'} \zeta^m_{\ell \ell'} a^{\ell'} \Big[\epsilon_{2s+1} \frac{\partial}{\partial \xi} \left\{ W^m_{\ell \ell'}[\mu_z, \xi](-1, t_r^{(s)}) \right\} \Big|_{\xi=\xi_{0,s}} \\
&\quad + \epsilon_{2s+1}(-1)^{\ell'+m} \mathcal{R}_{2s+1} \frac{\partial}{\partial \xi} \left\{ W^m_{\ell \ell'}[\bar{\mu}_z, \xi](-1, t_r^{(s)}) \right\} \Big|_{\xi=\xi_{0,s}} \\
&\quad + \epsilon_{2s+2} \mathcal{T}_{2s+1} \frac{\partial}{\partial \xi} \left\{ W^m_{\ell \ell'}[\mu_z, \xi](t_r^{(s)}, 1) \right\} \Big|_{\xi=\xi_{0,s}} \Big] \\
&\quad + \delta_{s1}\epsilon_1 \int_{-1}^{t_r^{(1)}} \mathrm{d}\eta \int_0^{2\pi} \mathrm{d}\phi \, [Y_\ell^m(\arccos\eta,\phi)]^* \frac{\partial}{\partial \xi} \left\{ \psi_{\mathrm{inc}}(\xi,\eta,\phi) \right\} \Big|_{\xi=\xi_{0,1}} \\
&\quad + \delta_{s1}\epsilon_2 \int_{t_r^{(1)}}^{1} \mathrm{d}\eta \int_0^{2\pi} \mathrm{d}\phi \, [Y_\ell^m(\arccos\eta,\phi)]^* \frac{\partial}{\partial \xi} \left\{ \psi_{\mathrm{tr}}(\xi,\eta,\phi) \right\} \Big|_{\xi=\xi_{0,1}} . \qquad (3.80)
\end{aligned}
$$

By introducing shorthands $\mathcal{J}$ and $\mathcal{L}$:

$$\begin{aligned}
\mathcal{J}^{m(i)}_{\ell\ell'}(t_r,\xi_0) \equiv\ & \xi_0^{\ell'+1}\Big\{\epsilon_i\frac{\partial}{\partial\xi}\,\{V^m_{\ell\ell'}[\mu_z,\xi](-1,t_r)\}|_{\xi=\xi_0} \\
& + \epsilon_i(-1)^{\ell'+m}\mathcal{R}_i\frac{\partial}{\partial\xi}\,\{V^m_{\ell\ell'}[\bar{\mu}_z,\xi](-1,t_r)\}|_{\xi=\xi_0} \\
& + \epsilon_{i+1}\mathcal{T}_i\frac{\partial}{\partial\xi}\,\{V^m_{\ell\ell'}[\mu_z,\xi](t_r,1)\}|_{\xi=\xi_0}\Big\} \\
=\ & \xi_0^{\ell'+1}\epsilon_i\mathcal{R}_i\Big[\frac{\partial}{\partial\xi}\,\{V^m_{\ell\ell'}[\mu_z,\xi](-1,t_r)\}|_{\xi=\xi_0} \\
& + (-1)^{\ell'+m}\frac{\partial}{\partial\xi}\,\{V^m_{\ell\ell'}[\bar{\mu}_z,\xi](-1,t_r)\}|_{\xi=\xi_0} \\
& + 2\frac{\epsilon_{i+1}}{\epsilon_i-\epsilon_{i+1}}\frac{\partial}{\partial\xi}\,\{V^m_{\ell\ell'}[\mu_z,\xi](-1,1)\}|_{\xi=\xi_0}\Big], \qquad (3.81)
\end{aligned}$$

and

$$\begin{aligned}
\mathcal{L}^{m(i)}_{\ell\ell'}(t_r,\xi_0) \equiv\ & \xi_0^{-\ell'}\Big\{\epsilon_i\frac{\partial}{\partial\xi}\,\{W^m_{\ell\ell'}[\mu_z,\xi](-1,t_r)\}|_{\xi=\xi_0} \\
& + \epsilon_i(-1)^{\ell'+m}\mathcal{R}_i\frac{\partial}{\partial\xi}\,\{W^m_{\ell\ell'}[\bar{\mu}_z,\xi](-1,t_r)\}|_{\xi=\xi_0} \\
& + \epsilon_{i+1}\mathcal{T}_i\frac{\partial}{\partial\xi}\,\{W^m_{\ell\ell'}[\mu_z,\xi](t_r,1)\}|_{\xi=\xi_0}\Big\} \\
=\ & \xi_0^{-\ell'}\epsilon_i\mathcal{R}_i\Big[\frac{\partial}{\partial\xi}\,\{W^m_{\ell\ell'}[\mu_z,\xi](-1,t_r)\}|_{\xi=\xi_0} \\
& + (-1)^{\ell'+m}\frac{\partial}{\partial\xi}\,\{W^m_{\ell\ell'}[\bar{\mu}_z,\xi](-1,t_r)\}|_{\xi=\xi_0} \\
& + 2\frac{\epsilon_{i+1}}{\epsilon_i-\epsilon_{i+1}}\frac{\partial}{\partial\xi}\,\{W^m_{\ell\ell'}[\mu_z,\xi](-1,1)\}|_{\xi=\xi_0}\Big], \qquad (3.82)
\end{aligned}$$

where it in the second step has been used that $\epsilon_i - \epsilon_{i+1}\mathcal{T} = \epsilon_i\mathcal{R}$, the weak formulation of the boundary condition (3.77) may now be written as

$$
\begin{aligned}
&\sum_{l'=|m|}^{\prime} \zeta_{\ell\ell'}^{m} R_{\perp,s}^{-\ell'-1} \left[\mathcal{J}_{\ell\ell'}^{m(2s-1)}(t_r^{(s)}, \xi_{0,s}) A_{\ell' m}^{(2s-1)} - \mathcal{J}_{\ell\ell'}^{m(2s+1)}(t_r^{(s)}, \xi_{0,s}) A_{\ell' m}^{(2s+1)} \right] \\
&+ \sum_{l'=|m|}^{\prime} \zeta_{\ell\ell'}^{m} R_{\perp,s}^{\ell'} \left[\mathcal{L}_{\ell\ell'}^{m(2s-1)}(t_r^{(s)}, \xi_{0,s}) B_{\ell' m}^{(2s-1)} - \mathcal{L}_{\ell\ell'}^{m(2s+1)}(t_r^{(s)}, \xi_{0,s}) B_{\ell' m}^{(2s+1)} \right] \\
&+ \delta_{s1}\epsilon_1 \int_{-1}^{t_r^{(1)}} \mathrm{d}\eta \int_0^{2\pi} \mathrm{d}\phi \, [Y_\ell^m(\arccos\eta, \phi)]^* \, \frac{\partial}{\partial \xi} \left\{ \psi_{\mathrm{inc}}(\xi, \eta, \phi) \right\} \Big|_{\xi=\xi_{0,1}} \\
&+ \delta_{s1}\epsilon_2 \int_{t_r^{(1)}}^{1} \mathrm{d}\eta \int_0^{2\pi} \mathrm{d}\phi \, [Y_\ell^m(\arccos\eta, \phi)]^* \, \frac{\partial}{\partial \xi} \left\{ \psi_{\mathrm{tr}}(\xi, \eta, \phi) \right\} \Big|_{\xi=\xi_{0,1}} = 0 \\
&\forall \quad s = 1, 2, 3, ..., S; \;\; \ell = 0, 1, 2, ...; \;\; m = 0, \pm 1, \pm 2, ..., \pm \ell.
\end{aligned}
\tag{3.83}
$$

Thus the second boundary condition (3.29b), in the weak formulation, has also been reduced to a set of linear equations for the unknown multipole coefficients $A_{\ell m}^{(i)}$ and $B_{\ell m}^{(i)}$ (odd i).

3.4.4. Incident and transmitted potentials

The main results so far, Eqs. (3.76) and (3.83), both have two final terms with integrals involving the incident potential ψ_{inc} and the transmitted potential ψ_{tr}. These potentials will now be defined, and these final terms will be expressed in terms of simpler integrals.

The incident electric field is assumed to be homogeneous, and thus in the Cartesian coordinate system given by:

$$
\begin{aligned}
\mathbf{E_0} &= [E_{0,x}, E_{0,y}, E_{0,z}] \\
&= E_0 \left[\sin\theta_0 \cos\phi_0, \sin\theta_0 \sin\phi_0, \cos\theta_0 \right].
\end{aligned}
\tag{3.84}
$$

Here θ_0 is the angle of $\mathbf{E_0}$ with the positive z-axis, and ϕ_0 is the angle between the projection of $\mathbf{E_0}$ on the substrate and the positive x-axis. Beware that these angles are *not* the same as the angles of incidence found in Fig. 2.1 and in Eqs. (2.14)– (2.17) for the reflection and transmission amplitudes. In fact, the multipole polarizabilities (and surface susceptibilities) found in this chapter are completely independent of $\mathbf{E_0}$ [1], and it is only introduced intermediately for convenience. If the goal is not only to find the surface susceptibilities, but also examining the electrostatic potential itself, this would obviously require specifying an incident electric field. Given an incident radiation (θ_i and ϕ_i)

[1] As long as $\mathbf{E_0}$ is kept constant, *i.e.* a homogeneous incident field.

and a polarization type (p or s) relative to the substrate, there are two possible directions for the electric field, both along the same line. Simply picking one of these directions gives the following relations, which ensure that $\theta_0 \in [0, \pi]$ and $\phi_0 \in [0, 2\pi)$:

$$\theta_0 = \begin{cases} \pi/2 - \theta_i & \text{p-polarization, } \theta_i < \pi/2 \\ \theta_i - \pi/2 & \text{p-polarization, } \theta_i > \pi/2 \\ \pi/2 & \text{s-polarization, any } \theta_i \end{cases}, \tag{3.85}$$

$$\phi_0 = \begin{cases} \phi_i + \pi & \text{p-polarization, } \phi_i < \pi \\ \phi_i - \pi & \text{p-polarization, } \phi_i > \pi \\ \phi_i + \pi/2 & \text{s-polarization, } \phi_i < 3\pi/2 \\ \phi_i - 3\pi/2 & \text{s-polarization, } \phi_i > 3\pi/2 \end{cases}. \tag{3.86}$$

It can be shown [17] that the electrostatic potential corresponding to the electrostatic field in Eq. (3.84) can be expressed in the oblate spheroidal coordinate system as:

$$\begin{aligned} \psi_{\text{inc}}(\mathbf{r}) =& -\mathbf{r} \cdot \mathbf{E_0} \\ =& \sqrt{\frac{2\pi}{3}} E_0 \Big[-\sqrt{2} \cos\theta_0 X_1^0(\xi, a) Y_1^0(\arccos\eta, \phi) \\ &+ \sin\theta_0 \mathrm{e}^{-i\phi_0} X_1^1(\xi, a) Y_1^1(\arccos\eta, \phi) \\ &- \sin\theta_0 \mathrm{e}^{i\phi_0} X_1^{-1}(\xi, a) Y_1^{-1}(\arccos\eta, \phi) \Big]. \end{aligned} \tag{3.87}$$

The potential of a transmitted field in the region $z > d$ satisfying the boundary conditions with ψ_{inc} across a sharp planar surface at $z = d$ is then [17]:

$$\begin{aligned} \psi_{\text{tr}}(\mathbf{r}) =& \, d \left(\frac{\epsilon_1}{\epsilon_2} - 1 \right) E_0 \cos\theta_0 \\ &+ \sqrt{\frac{2\pi}{3}} E_0 \Bigg\{ -\sqrt{2} \frac{\epsilon_1}{\epsilon_2} \cos\theta_0 X_1^0(\xi, a) Y_1^0(\arccos\eta, \phi) \\ &+ \sin\theta_0 \mathrm{e}^{-i\phi_0} X_1^1(\xi, a) Y_1^1(\arccos\eta, \phi) \\ &- \sin\theta_0 \mathrm{e}^{i\phi_0} X_1^{-1}(\xi, a) Y_1^{-1}(\arccos\eta, \phi) \Bigg\}, \end{aligned} \tag{3.88}$$

where ϵ_1 is the dielectric function of the ambient (region 1) and ϵ_2 is the dielectric function of the substrate (region 2).

In this section a new shorthand for a class of integrals will be introduced, defined by

$$Q^m_{\ell\ell'}(\eta_1,\eta_2) \equiv \int_{\eta_1}^{\eta_2} \mathrm{d}\eta P^m_\ell(\eta) P^m_{\ell'}(\eta), \tag{3.89}$$

which has the following orthogonality property:

$$Q^m_{\ell\ell'}(-1,1) = \frac{2}{2\ell+1}\frac{(\ell+m)!}{(\ell-m)!}\delta_{\ell\ell'} = \frac{\delta_{\ell\ell'}}{\zeta^m_{\ell\ell}}. \tag{3.90}$$

Do not confuse these integrals with the functions $Q^m_\ell(i\xi)$, which are the associated Legendre functions of the second kind, and given by Eq. (3.37).

Using Eq. (3.87) for the incident potential, Eq. (3.88) for the transmitted potential, together with Eqs. (3.42), (3.66) and (3.90), one may show that

$$\begin{aligned}
&\int_{-1}^{t_r^{(1)}} \mathrm{d}\eta \int_0^{2\pi} \mathrm{d}\phi \, [Y^m_\ell(\arccos\eta,\phi)]^* \, \psi_{\mathrm{inc}}(\xi,\eta,\phi)|_{\xi=\xi_{0,1}} \\
&= \sqrt{\frac{2\pi}{3}} a E_0 \Big\{ -\sqrt{2}\cos\theta_0 X^0_1(\xi_{0,1})\zeta^0_{\ell 1} Q^0_{\ell 1}(-1,t_r^{(1)})\delta_{m0} \\
&+ \sin\theta_0 \mathrm{e}^{-i\phi_0} X^1_1(\xi_{0,1})\zeta^1_{\ell 1} Q^1_{\ell 1}(-1,t_r^{(1)})\delta_{m1} \\
&- \sin\theta_0 \mathrm{e}^{i\phi_0} X^{-1}_1(\xi_{0,1})\zeta^{-1}_{\ell 1} Q^{-1}_{\ell 1}(-1,t_r^{(1)})\delta_{m,-1} \Big\}
\end{aligned} \tag{3.91}$$

and

$$\begin{aligned}
&\int_{t_r^{(1)}}^{1} \mathrm{d}\eta \int_0^{2\pi} \mathrm{d}\phi \, [Y^m_\ell(\arccos\eta,\phi)]^* \, \psi_{\mathrm{tr}}(\xi,\eta,\phi)|_{\xi=\xi_{0,1}} \\
&= \sqrt{\frac{4\pi}{3}} E_0 \cos\theta_0 \Bigg[\sqrt{3} d \left(\frac{\epsilon_1}{\epsilon_2} - 1\right) \zeta^0_{\ell 0} \left(\frac{\delta_{\ell 0}}{\zeta^0_{00}} - Q^0_{\ell 0}(-1,t_r^{(1)}) \right) \\
&- a\frac{\epsilon_1}{\epsilon_2} X^0_1(\xi_{0,1})\zeta^0_{\ell 1} \left(\frac{\delta_{\ell 1}}{\zeta^0_{11}} - Q^0_{\ell 1}(-1,t_r^{(1)}) \right) \Bigg] \delta_{m0} \\
&+ \sqrt{\frac{2\pi}{3}} a E_0 \sin\theta_0 \mathrm{e}^{-i\phi_0} X^1_1(\xi_{0,1})\zeta^1_{\ell 1} \left(\frac{\delta_{\ell 1}}{\zeta^1_{11}} - Q^1_{\ell 1}(-1,t_r^{(1)}) \right) \delta_{m1} \\
&- \sqrt{\frac{2\pi}{3}} a E_0 \sin\theta_0 \mathrm{e}^{i\phi_0} X^{-1}_1(\xi_{0,1})\zeta^{-1}_{\ell 1} \left(\frac{\delta_{\ell 1}}{\zeta^{-1}_{11}} - Q^{-1}_{\ell 1}(-1,t_r^{(1)}) \right) \delta_{m,-1}.
\end{aligned} \tag{3.92}$$

Combining Eqs. (3.91) and (3.92), while using that $a = R_{\perp,s}/\xi_{0,s}$ and $d =$

$R_{\perp,s}t_r^{(s)}$ for any s, leads to the following equation:

$$
\begin{aligned}
&\int_{-1}^{t_r^{(1)}} \mathrm{d}\eta \int_0^{2\pi} \mathrm{d}\phi \, [Y_\ell^m(\arccos\eta,\phi)]^* \, \psi_{\mathrm{inc}}(\xi,\eta,\phi)|_{\xi=\xi_{0,1}} \\
&+ \int_{t_r^{(1)}}^{1} \mathrm{d}\eta \int_0^{2\pi} \mathrm{d}\phi \, [Y_\ell^m(\arccos\eta,\phi)]^* \, \psi_{\mathrm{tr}}(\xi,\eta,\phi)|_{\xi=\xi_{0,1}} \\
&= - R_{\perp,s} E_0 \cos\theta_0 \sqrt{\frac{4\pi}{3}} \Bigg\{ \frac{\epsilon_1}{\epsilon_2} \xi_{0,s}^{-1} X_1^0(\xi_{0,1}) \delta_{\ell 1} + \left(\frac{\epsilon_1}{\epsilon_2} - 1 \right) \Big[\sqrt{3} t_r^{(1)} \zeta_{\ell 0}^0 Q_{\ell 0}^0(-1, t_r^{(1)}) \\
&\quad - \xi_{0,s}^{-1} X_1^0(\xi_{0,1}) \zeta_{\ell 1}^0 Q_{\ell 1}^0(-1, t_r^{(1)}) - \sqrt{3} t_r^{(1)} \delta_{\ell 0} \Big] \Bigg\} \delta_{m0} \\
&\quad + R_{\perp,s} \sqrt{\frac{2\pi}{3}} E_0 \sin\theta_0 \mathrm{e}^{-i\phi_0} \xi_{0,s}^{-1} X_1^1(\xi_{0,1}) \delta_{\ell 1} \delta_{m1} \\
&\quad - R_{\perp,s} \sqrt{\frac{2\pi}{3}} E_0 \sin\theta_0 \mathrm{e}^{i\phi_0} \xi_{0,s}^{-1} X_1^{-1}(\xi_{0,1}) \delta_{\ell 1} \delta_{m,-1}.
\end{aligned} \tag{3.93}
$$

Similarly one may show that

$$
\begin{aligned}
&\int_{-1}^{t_r^{(1)}} \mathrm{d}\eta \int_0^{2\pi} \mathrm{d}\phi \, [Y_\ell^m(\arccos\eta,\phi)]^* \, \frac{\partial}{\partial\xi} \left\{ \psi_{\mathrm{inc}}(\xi,\eta,\phi) \right\} \Big|_{\xi=\xi_{0,1}} \\
&= \sqrt{\frac{2\pi}{3}} a E_0 \Bigg\{ - \sqrt{2} \cos\theta_0 \, \frac{\partial X_1^0(\xi)}{\partial\xi} \Big|_{\xi=\xi_{0,1}} \zeta_{\ell 1}^0 Q_{\ell 1}^0(-1, t_r^{(1)}) \delta_{m0} \\
&\quad + \sin\theta_0 \mathrm{e}^{-i\phi_0} \, \frac{\partial X_1^1(\xi)}{\partial\xi} \Big|_{\xi=\xi_{0,1}} \zeta_{\ell 1}^1 Q_{\ell 1}^1(-1, t_r^{(1)}) \delta_{m1} \\
&\quad - \sin\theta_0 \mathrm{e}^{i\phi_0} \, \frac{\partial X_1^{-1}(\xi)}{\partial\xi} \Big|_{\xi=\xi_{0,1}} \zeta_{\ell 1}^{-1} Q_{\ell 1}^{-1}(-1, t_r^{(1)}) \delta_{m,-1} \Bigg\},
\end{aligned} \tag{3.94}
$$

and

$$
\begin{aligned}
&\int_{t_r^{(1)}}^{1} \mathrm{d}\eta \int_0^{2\pi} \mathrm{d}\phi \, [Y_\ell^m(\arccos\eta,\phi)]^* \, \frac{\partial}{\partial\xi} \left\{ \psi_{\mathrm{tr}}(\xi,\eta,\phi) \right\} \Big|_{\xi=\xi_{0,1}} \\
&= \sqrt{\frac{2\pi}{3}} a E_0 \Bigg\{ - \sqrt{2} \frac{\epsilon_1}{\epsilon_2} \cos\theta_0 \, \frac{\partial X_1^0(\xi)}{\partial\xi} \Big|_{\xi=\xi_{0,1}} \zeta_{\ell 1}^0 \left[\frac{\delta_{\ell 1}}{\zeta_{11}^0} - Q_{\ell 1}^0(-1, t_r^{(1)}) \right] \delta_{m0} \\
&\quad + \sin\theta_0 \mathrm{e}^{-i\phi_0} \, \frac{\partial X_1^1(\xi)}{\partial\xi} \Big|_{\xi=\xi_{0,1}} \zeta_{\ell 1}^1 \left[\frac{\delta_{\ell 1}}{\zeta_{11}^1} - Q_{\ell 1}^1(-1, t_r^{(1)}) \right] \delta_{m1} \\
&\quad - \sin\theta_0 \mathrm{e}^{i\phi_0} \, \frac{\partial X_1^{-1}(\xi)}{\partial\xi} \Big|_{\xi=\xi_{0,1}} \zeta_{\ell 1}^{-1} \left[\frac{\delta_{\ell 1}}{\zeta_{11}^{-1}} - Q_{\ell 1}^{-1}(-1, t_r^{(1)}) \right] \delta_{m,-1} \Bigg\},
\end{aligned} \tag{3.95}
$$

which may be combined into the following equation:

$$
\begin{aligned}
&\epsilon_1 \int_{-1}^{t_r^{(1)}} \mathrm{d}\eta \int_0^{2\pi} \mathrm{d}\phi \, [Y_\ell^m(\arccos\eta,\phi)]^* \, \frac{\partial}{\partial\xi} \left\{ \psi_{\mathrm{inc}}(\xi,\eta,\phi) \right\} \Big|_{\xi=\xi_{0,1}} \\
+&\epsilon_2 \int_{t_r^{(1)}}^{1} \mathrm{d}\eta \int_0^{2\pi} \mathrm{d}\phi \, [Y_\ell^m(\arccos\eta,\phi)]^* \, \frac{\partial}{\partial\xi} \left\{ \psi_{\mathrm{tr}}(\xi,\eta,\phi) \right\} \Big|_{\xi=\xi_{0,1}} \\
&= -R_{\perp,s}\xi_{0,s}^{-1} \sqrt{\frac{4\pi}{3}} E_0 \cos\theta_0 \epsilon_1 \, \frac{\partial X_1^0(\xi)}{\partial\xi}\bigg|_{\xi=\xi_{0,1}} \delta_{\ell 1}\delta_{m0} \\
&+ R_{\perp,s}\xi_{0,s}^{-1} \sqrt{\frac{2\pi}{3}} E_0 \sin\theta_0 \mathrm{e}^{-i\phi_0} \, \frac{\partial X_1^1(\xi)}{\partial\xi}\bigg|_{\xi=\xi_{0,1}} \\
&\qquad \times \left\{ (\epsilon_1-\epsilon_2)\zeta_{\ell 1}^1 Q_{\ell 1}^1(-1,t_r^{(1)}) + \epsilon_2\delta_{\ell 1} \right\} \delta_{m1} \\
&- R_{\perp,s}\xi_{0,s}^{-1} \sqrt{\frac{2\pi}{3}} E_0 \sin\theta_0 \mathrm{e}^{i\phi_0} \, \frac{\partial X_1^{-1}(\xi)}{\partial\xi}\bigg|_{\xi=\xi_{0,1}} \\
&\qquad \times \left\{ (\epsilon_1-\epsilon_2)\zeta_{\ell 1}^{-1} Q_{\ell 1}^{-1}(-1,t_r^{(1)}) + \epsilon_2\delta_{\ell 1} \right\} \delta_{m,-1}.
\end{aligned}
\tag{3.96}
$$

3.4.5. Linear set of equations for the expansion coefficients

Equations (3.93) and (3.96) may now be combined with Eqs. (3.76) and (3.83) respectively, to give the following set of equations for the expansion coefficients $A_{\ell m}^{(i)}$ and $B_{\ell m}^{(i)}$ with odd i:

$$
\begin{aligned}
&\sum_{\ell'=|m|}^{\prime} \zeta_{\ell\ell'}^m R_{\perp,s}^{-\ell'-2} \left[\mathcal{I}_{\ell\ell'}^{m(2s-1)}(t_r^{(s)},\xi_{0,s}) A_{\ell' m}^{(2s-1)} - \mathcal{I}_{\ell\ell'}^{m(2s+1)}(t_r^{(s)},\xi_{0,s}) A_{\ell' m}^{(2s+1)} \right] \\
&+ \sum_{\ell'=|m|}^{\prime} \zeta_{\ell\ell'}^m R_{\perp,s}^{\ell'-1} \left[\mathcal{K}_{\ell\ell'}^{m(2s-1)}(t_r^{(s)},\xi_{0,s}) B_{\ell' m}^{(2s-1)} - \mathcal{K}_{\ell\ell'}^{m(2s+1)}(t_r^{(s)},\xi_{0,s}) B_{\ell' m}^{(2s+1)} \right] \\
&= \delta_{s,1} E_0 \Bigg[\cos\theta_0 \sqrt{\frac{4\pi}{3}} \Bigg\{ \frac{\epsilon_1}{\epsilon_2} \xi_{0,1}^{-1} X_1^0(\xi_{0,1}) \delta_{\ell 1} + \left(\frac{\epsilon_1}{\epsilon_2} - 1 \right) \Big[\sqrt{3} t_r^{(1)} \zeta_{\ell 0}^0 Q_{\ell 0}^0(-1,t_r^{(1)}) \\
&- \xi_{0,1}^{-1} X_1^0(\xi_{0,1}) \zeta_{\ell 1}^0 Q_{\ell 1}^0(-1,t_r^{(1)}) - \sqrt{3} t_r^{(1)} \delta_{\ell 0} \Big] \Bigg\} \delta_{m0} \\
&- \sqrt{\frac{2\pi}{3}} \sin\theta_0 \mathrm{e}^{-i\phi_0} \xi_{0,1}^{-1} X_1^1(\xi_{0,1}) \delta_{\ell 1}\delta_{m1} + \sqrt{\frac{2\pi}{3}} \sin\theta_0 \mathrm{e}^{i\phi_0} \xi_{0,1}^{-1} X_1^{-1}(\xi_{0,1}) \delta_{\ell 1}\delta_{m,-1} \Bigg] \\
&+ \frac{2\sqrt{\pi}}{R_{\perp,s}} \left[\psi_0^{(2s+1)} - \psi_0^{(2s-1)} \right] \delta_{\ell 0}\delta_{m0} \\
&\forall \quad s = 1,2,3,...,S; \;\; \ell = 0,1,2,...; \;\; m = 0,\pm1,\pm2,...,\pm\ell,
\end{aligned}
\tag{3.97}
$$

and

$$
\begin{aligned}
&\sum_{l'=|m|}^{\prime} \zeta_{\ell\ell'}^{m} R_{\perp,s}^{-\ell'-2} \left[\mathcal{J}_{\ell\ell'}^{m(2s-1)}(t_r^{(s)}, \xi_{0,s}) A_{\ell' m}^{(2s-1)} - \mathcal{J}_{\ell\ell'}^{m(2s+1)}(t_r^{(s)}, \xi_{0,s}) A_{\ell' m}^{(2s+1)} \right] \\
&+ \sum_{l'=|m|}^{\prime} \zeta_{\ell\ell'}^{m} R_{\perp,s}^{\ell'-1} \left[\mathcal{L}_{\ell\ell'}^{m(2s-1)}(t_r^{(s)}, \xi_{0,s}) B_{\ell' m}^{(2s-1)} - \mathcal{L}_{\ell\ell'}^{m(2s+1)}(t_r^{(s)}, \xi_{0,s}) B_{\ell' m}^{(2s+1)} \right] \\
&= \delta_{s1} \xi_{0,1}^{-1} E_0 \Bigg\{ \sqrt{\frac{4\pi}{3}} \epsilon_1 \cos\theta_0 \left. \frac{\partial X_1^0(\xi)}{\partial \xi} \right|_{\xi=\xi_{0,1}} \delta_{\ell 1} \delta_{m0} \\
&- \sqrt{\frac{2\pi}{3}} \sin\theta_0 \mathrm{e}^{-i\phi_0} \left. \frac{\partial X_1^1(\xi)}{\partial \xi} \right|_{\xi=\xi_{0,1}} \left[(\epsilon_1 - \epsilon_2) \zeta_{\ell 1}^{1} Q_{\ell 1}^{1}(-1, t_r^{(1)}) + \epsilon_2 \delta_{\ell 1} \right] \delta_{m1} \\
&+ \sqrt{\frac{2\pi}{3}} \sin\theta_0 \mathrm{e}^{i\phi_0} \left. \frac{\partial X_1^{-1}(\xi)}{\partial \xi} \right|_{\xi=\xi_{0,1}} \left[(\epsilon_1 - \epsilon_2) \zeta_{\ell 1}^{-1} Q_{\ell 1}^{-1}(-1, t_r^{(1)}) + \epsilon_2 \delta_{\ell 1} \right] \delta_{m,-1} \Bigg\} \\
&\forall \quad s = 1, 2, 3, ..., S; \ \ell = 0, 1, 2, ...; \ m = 0, \pm 1, \pm 2, ..., \pm \ell.
\end{aligned}
\tag{3.98}
$$

First note that there is no coupling between different values of m, and thus a system of equations may be set up for each m separately. Note also that the right hand sides are only nonzero for $m = 0, \pm 1$, because the assumed incident field only contains terms which are nonzero for these values of m. All dependence on the incident electric field strength E_0 is on the right hand sides, and thus the system of equations for the coefficients $A_{\ell m}^{(i)}$ and $B_{\ell m}^{(i)}$ when $|m| > 1$ are independent of E_0. When $E_0 = 0$ one would expect a homogeneous potential[2], making the expansion coefficients zero. Since the coefficients for $|m| > 1$ are independent of E_0, it may then be concluded that for all homogeneous $\mathbf{E_0}$ one has:

$$
\begin{aligned}
A_{\ell m}^{(i)} &= B_{\ell m}^{(i)} = 0 \\
&\text{when } |m| > 1
\end{aligned}
\tag{3.99}
$$

In fact, only the systems for $m = 0$ and $m = 1$ need to be solved, because the coefficients for negative m are related to the corresponding ones for positive m in a simple way. Using Eqs. (3.34) and (3.38), one may show that

$$
\begin{aligned}
\zeta_{\ell\ell'}^{-m} V_{\ell\ell'}^{-m}[\kappa_z, \xi](\eta_1, \eta_2) &= \zeta_{\ell\ell'}^{m} V_{\ell\ell'}^{m}[\kappa_z, \xi](\eta_1, \eta_2) \\
\zeta_{\ell\ell'}^{-m} W_{\ell\ell'}^{-m}[\kappa_z, \xi](\eta_1, \eta_2) &= \zeta_{\ell\ell'}^{m} W_{\ell\ell'}^{m}[\kappa_z, \xi](\eta_1, \eta_2),
\end{aligned}
\tag{3.100}
$$

[2]Still assuming zero net charge in the island.

which may be used to show that

$$\begin{aligned}
\zeta_{\ell\ell'}^{-m}\mathcal{I}_{\ell\ell'}^{-m(i)}(t_r,\xi_0) &= \zeta_{\ell\ell'}^{m}\mathcal{I}_{\ell\ell'}^{m(i)}(t_r,\xi_0)\\
\zeta_{\ell\ell'}^{-m}\mathcal{K}_{\ell\ell'}^{-m(i)}(t_r,\xi_0) &= \zeta_{\ell\ell'}^{m}\mathcal{K}_{\ell\ell'}^{m(i)}(t_r,\xi_0)\\
\zeta_{\ell\ell'}^{-m}\mathcal{J}_{\ell\ell'}^{-m(i)}(t_r,\xi_0) &= \zeta_{\ell\ell'}^{m}\mathcal{J}_{\ell\ell'}^{m(i)}(t_r,\xi_0)\\
\zeta_{\ell\ell'}^{-m}\mathcal{L}_{\ell\ell'}^{-m(i)}(t_r,\xi_0) &= \zeta_{\ell\ell'}^{m}\mathcal{L}_{\ell\ell'}^{m(i)}(t_r,\xi_0).
\end{aligned} \tag{3.101}$$

By inspecting Eqs. (3.97) and (3.98), and using that $X_1^{-1}(\xi) = X_1^1(\xi)$ and $\zeta_{\ell 1}^{-1}Q_{\ell 1}^{-1}(\eta_1,\eta_2) = \zeta_{\ell 1}^{1}Q_{\ell 1}^{1}(\eta_1,\eta_2)$, one finds the following symmetry relations for a change in the sign of m:

$$A_{\ell,-1}^{(i)} = (-1)\mathrm{e}^{i2\phi_0}A_{\ell,1}^{(i)} \tag{3.102}$$

and

$$B_{\ell,-1}^{(i)} = (-1)\mathrm{e}^{i2\phi_0}B_{\ell,1}^{(i)} \tag{3.103}$$

for all $\ell > 0$.

The multipole expansions, and thus the sums in Eqs. (3.97) and (3.98), contain an infinite number of terms. To be able to solve this problem in practice one must neglect all $A_{\ell' m}^{(i)}$ and $B_{\ell' m}^{(i)}$ with $\ell' > M$, where M will be called the *multipole order* of the calculation. To have a matching number of equations for these unknowns, ℓ will then also be restricted to be no larger than M.

As mentioned earlier, because of net charge neutrality there are no multipole coefficients for $\ell' = 0$. There are enough equations in the cases $\ell = 1, ..., M$ of Eqs. (3.97) and (3.98) to solve for all the unknown coefficients, and thus the case of $\ell = 0$ may be treated separately. For $\ell > 0$, one gets the following

system of equations for the unknown coefficients $A_{\ell' m}^{(i)}$ and $B_{\ell' m}^{(i)}$:

$$
\begin{aligned}
&\sum_{\ell'=1}^{M} \zeta_{\ell\ell'}^{m} R_{\perp,s}^{-\ell'-2} \left[\mathcal{I}_{\ell\ell'}^{m(2s-1)}(t_r^{(s)}, \xi_{0,s}) A_{\ell' m}^{(2s-1)} - \mathcal{I}_{\ell\ell'}^{m(2s+1)}(t_r^{(s)}, \xi_{0,s}) A_{\ell' m}^{(2s+1)} \right] \\
&+ \sum_{\ell'=1}^{M} \zeta_{\ell\ell'}^{m} R_{\perp,s}^{\ell'-1} \left[\mathcal{K}_{\ell\ell'}^{m(2s-1)}(t_r^{(s)}, \xi_{0,s}) B_{\ell' m}^{(2s-1)} - \mathcal{K}_{\ell\ell'}^{m(2s+1)}(t_r^{(s)}, \xi_{0,s}) B_{\ell' m}^{(2s+1)} \right] \\
&= \delta_{s1} E_0 \Bigg[\cos\theta_0 \sqrt{\frac{4\pi}{3}} \Bigg\{ \frac{\epsilon_1}{\epsilon_2} \xi_{0,1}^{-1} X_1^0(\xi_{0,1}) \delta_{\ell 1} + \left(\frac{\epsilon_1}{\epsilon_2} - 1 \right) \Big[\sqrt{3} t_r^{(1)} \zeta_{\ell 0}^{0} Q_{\ell 0}^{0}(-1, t_r^{(1)}) \\
&- \xi_{0,1}^{-1} X_1^0(\xi_{0,1}) \zeta_{\ell 1}^{0} Q_{\ell 1}^{0}(-1, t_r^{(1)}) \Big] \Bigg\} \delta_{m0} \\
&- \sqrt{\frac{2\pi}{3}} \sin\theta_0 \mathrm{e}^{-i\phi_0} \xi_{0,1}^{-1} X_1^1(\xi_{0,1}) \delta_{\ell 1} \delta_{m1} \Bigg] \\
&\forall \quad s = 1, 2, 3, ..., S; \ \ell = 1, 2, 3, ..., M; \ m = 0, 1,
\end{aligned}
\tag{3.104}
$$

and

$$
\begin{aligned}
&\sum_{l'=1}^{M} \zeta_{\ell\ell'}^{m} R_{\perp,s}^{-\ell'-2} \left[\mathcal{J}_{\ell\ell'}^{m(2s-1)}(t_r^{(s)}, \xi_{0,s}) A_{\ell' m}^{(2s-1)} - \mathcal{J}_{\ell\ell'}^{m(2s+1)}(t_r^{(s)}, \xi_{0,s}) A_{\ell' m}^{(2s+1)} \right] \\
&+ \sum_{l'=1}^{M} \zeta_{\ell\ell'}^{m} R_{\perp,s}^{\ell'-1} \left[\mathcal{L}_{\ell\ell'}^{m(2s-1)}(t_r^{(s)}, \xi_{0,s}) B_{\ell' m}^{(2s-1)} - \mathcal{L}_{\ell\ell'}^{m(2s+1)}(t_r^{(s)}, \xi_{0,s}) B_{\ell' m}^{(2s+1)} \right] \\
&= \delta_{s1} \xi_{0,1}^{-1} E_0 \Bigg\{ \sqrt{\frac{4\pi}{3}} \epsilon_1 \cos\theta_0 \left. \frac{\partial X_1^0(\xi)}{\partial \xi} \right|_{\xi=\xi_{0,1}} \delta_{\ell 1} \delta_{m0} \\
&- \sqrt{\frac{2\pi}{3}} \sin\theta_0 \mathrm{e}^{-i\phi_0} \left. \frac{\partial X_1^1(\xi)}{\partial \xi} \right|_{\xi=\xi_{0,1}} \left[(\epsilon_1 - \epsilon_2) \zeta_{\ell 1}^{1} Q_{\ell 1}^{1}(-1, t_r^{(1)}) + \epsilon_2 \delta_{\ell 1} \right] \delta_{m1} \Bigg\} \\
&\forall \quad s = 1, 2, 3, ..., S; \ \ell = 1, 2, 3, ..., M; \ m = 0, 1.
\end{aligned}
\tag{3.105}
$$

The case of $\ell = 0$ gives an expression for the difference between the constant terms of the potentials in neighboring media, which may be calculated once the coefficients $A_{\ell' 0}^{(i)}$ and $B_{\ell' 0}^{(i)}$ have been found by solving the system of equations

given by Eqs. (3.104) and (3.105):

$$\begin{aligned}
&\left[\psi_0^{(2s+1)} - \psi_0^{(2s-1)}\right] \\
&= \frac{1}{2\sqrt{\pi}} \sum_{\ell=1}^{M} \zeta_{0\ell}^0 R_{\perp,s}^{-\ell-1} \left[\mathcal{I}_{0\ell}^{0(2s-1)}(t_r^{(s)}, \xi_{0,s}) A_{\ell 0}^{(2s-1)} - \mathcal{I}_{0\ell}^{0(2s+1)}(t_r^{(s)}, \xi_{0,s}) A_{\ell 0}^{(2s+1)}\right] \\
&+ \frac{1}{2\sqrt{\pi}} \sum_{\ell=1}^{M} \zeta_{0\ell}^0 R_{\perp,s}^{\ell} \left[\mathcal{K}_{0\ell}^{0(2s-1)}(t_r^{(s)}, \xi_{0,s}) B_{\ell 0}^{(2s-1)} - \mathcal{K}_{0\ell}^{0(2s+1)}(t_r^{(s)}, \xi_{0,s}) B_{\ell 0}^{(2s+1)}\right] \\
&+ \delta_{s1} E_0 R_{\perp,1} \cos\theta_0 \left(\frac{\epsilon_1}{\epsilon_2} - 1\right) \\
&\quad \times \left\{ \frac{1}{\sqrt{3}} \zeta_{01}^0 Q_{01}^0(-1, t_r^{(1)}) + t_r^{(1)} \left(1 - \zeta_{00}^0 Q_{00}^0(-1, t_r^{(1)})\right) \right\} \\
&\forall \quad s = 1, 2, 3, ..., S,
\end{aligned} \tag{3.106}$$

where it has been used that $\xi^{-1} X_1^0(\xi) = 1$.

Two of the expansion coefficients must be set to zero immediately to ensure that the potential is finite everywhere. By inspecting the general solution for the potential in media above the substrate (3.59), one sees that $A_{\ell m}^{(i)}$ must be set to zero in media where $Z_\ell^m(\xi_\mu, a)$ and/or $Z_\ell^m(\xi_{\bar{\mu}}, a)$ might be invalid as solutions. Similarly, $B_{\ell m}^{(i)}$ must be set to zero in media where $X_\ell^m(\xi_\mu, a)$ and/or $X_\ell^m(\xi_{\bar{\mu}}, a)$ might be invalid as solutions. As mentioned in Sec. 3.4.1, $P_\ell^m(i\xi)$ (and $X_\ell^m(\xi_\mu, a)$) diverges as $\xi \to \infty$, and $Q_\ell^m(i\xi)$ (and $Z_\ell^m(\xi_\mu, a)$) becomes invalid as as $\xi \to 0$. This leads to the immediate elimination of the following coefficients:

$$\begin{aligned}
B_{\ell m}^{(1)} &= 0 \\
A_{\ell m}^{(j)} &= 0,
\end{aligned} \tag{3.107}$$

where medium j is the medium above the substrate containing the area where $\xi_\mu \to 0$. Note that this area is a disc extending to the focal ring, not a point. If the multipole μ has been placed such that this disc is contained within more than one medium, this approach will not be valid.

From Eqs. (3.104) and (3.105) one can see that the number of equations for the coefficients is $2 \times 2 \times M \times S = 4MS$. Obviously the number of unknown coefficients should be the same. The unknown coefficients after taking care of the boundary conditions across the substrate surface (see Sec. 3.4.2) are $A_{\ell m}$ and $B_{\ell m}$ for every medium *above* the substrate. There are always $S + 1$ media above the substrate, and there are initially $2 \times 2 \times M$ coefficients for each of them, taking into account the combinations of ℓ and m for both A and B. According to Eq. (3.107) one must subtract $2 \times 2 \times M$ from this number

however, since these coefficients are know to be zero from the start. In total this gives $2 \times 2 \times M \times (S+1) - 2 \times 2 \times M = 4MS$ unknown coefficients, which is the same as the number of equations. As mentioned, each m may be treated separately. Hence there are two systems of dimension $2MS$ to be solved, one for $m = 0$ and one for $m = 1$.

The reference point for the potential can be set freely, so without loss of generality one may set the constant term in the ambient to zero:

$$\psi_0^{(1)} = 0. \tag{3.108}$$

By use of Eq. (3.106) and the first part of Eq. (3.55), all other constant terms $\psi_0^{(i)}$ may then be calculated, as long as one has found the values $A_{\ell 0}$ and $B_{\ell 0}$ for $\ell = 1, ..., M$.

When the linear systems of Eqs. (3.104) and (3.105) have been solved, the expansion coefficients may be used to calculate the island polarizabilities (Sec. 3.4.6) and subsequently the surface susceptibilities of the film (Sec. 3.5). Additionally one may calculate the potential at any point in space, by inserting the expansion coefficients into the general solutions in Eqs. (3.59) and (3.60), and finding ψ_0 in each region through Eq. (3.106).

3.4.6. Island polarizabilities

The polarizability $\boldsymbol{\alpha}$, assuming a stationary system, is defined by [17]

$$\mathbf{P}(\mathbf{r}, \omega) = \int \boldsymbol{\alpha}(\mathbf{r}, \omega | \mathbf{r}') \cdot \mathbf{E}(\mathbf{r}', \omega) \mathrm{d}\mathbf{r}', \tag{3.109}$$

where $\mathbf{P}$ is the polarization and $\mathbf{E}$ is the electric field. In words, the polarizability matrix $\boldsymbol{\alpha}(\mathbf{r}, \omega | \mathbf{r}')$ is a frequency dependent specification of how the electric field at a point $\mathbf{r}'$ contributes to the polarization at a point $\mathbf{r}$. When one is interested in the effects of the polarization as seen from a place far away from the island compared to its size, it is convenient to expand the polarization in a multipole expansion. When the island has an axis of symmetry perpendicular to the substrate, and one chooses to neglect multipole polarizabilities of higher than quadrupole order, one can essentially describe the polarizability of the island by dipole polarizabilities α_z,$\alpha_\parallel$ and quadrupole polarizabilities α_z^{10},$\alpha_\parallel^{10}$.

For the case considered here, it can be shown that they are given by [17]

$$\begin{aligned}
\alpha_z &= \frac{2\pi\epsilon_1}{\sqrt{\pi/3}E_0\cos\theta_0}A_{10}^{(1)} \\
\alpha_\parallel &= \frac{-4\pi\epsilon_1}{\sqrt{2\pi/3}E_0\sin\theta_0\exp(-i\phi_0)}A_{11}^{(1)} \\
\alpha_z^{10} &= \frac{\pi\epsilon_1}{\sqrt{\pi/5}E_0\cos\theta_0}A_{20}^{(1)} \\
\alpha_\parallel^{10} &= \frac{-4\pi\epsilon_1}{\sqrt{6\pi/5}E_0\sin\theta_0\exp(-i\phi_0)}A_{21}^{(1)}
\end{aligned} \tag{3.110}$$

Notice how these polarizabilities are in fact independent of E_0, θ_0 and ϕ_0, because $A_{\ell 0}^{(i)}$ and $A_{\ell 1}^{(i)}$ are proportional to $[E_0\cos\theta]$ and $[E_0\sin\theta_0\exp(-i\phi_0)]$ respectively.

The fact that the polarizabilities of interest only depend on $A_{\ell m}$ up to quadrupolar order does not mean that one should truncate (3.104) and (3.105) at $M = 2$. The coupling displayed means that $A_{10}^{(1)}$, $A_{11}^{(1)}$, $A_{20}^{(1)}$ and $A_{21}^{(1)}$ will be obtained more and more accurately as $M \to \infty$. In practice one has to find the M which gives the coefficients to the needed accuracy.

3.5. Island films

So far we have found the polarizability of a single island, but the objective is to find the optical properties of a substrate supporting many such islands in an array, such as the ones illustrated in Fig. 3.6. Besides the lattice symmetry, which is assumed to be square or hexagonal, the lattice also has a parameter called the *lattice constant* (L). This is the nearest neighbor distance between islands in the film.

3.5.1. Correcting for island-island interactions

The polarizabilities calculated so far in Eq. (3.110) only account for the response of a single truncated island, while accounting for the interactions with image charges in the substrate. If the lattice constant is very large, these may be appropriate to use when calculating the optical properties of the film, but if that is not the case one should correct for island-island interactions. As a first approximation one may correct only the dipolar response, which has the largest range of effect. It has been shown that the dipolar corrections are given

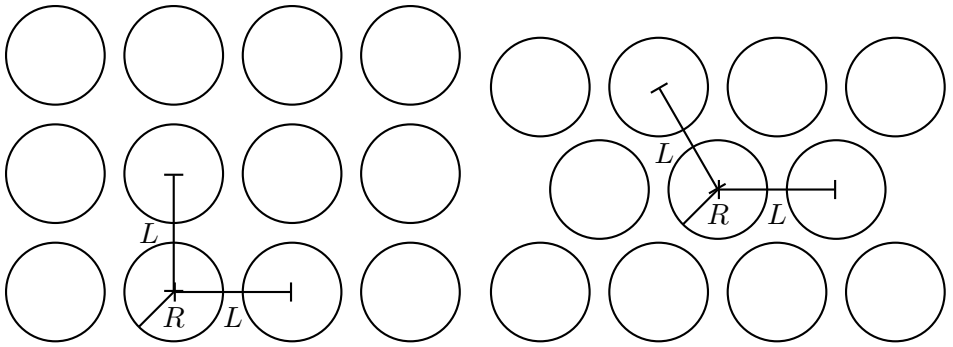

(a) (b)

Figure 3.6.: The lattice types supported by GranFilm: a) Square lattice and b) hexagonal lattice. Both lattices are drawn with the same values for R and L, showing that the hexagonal lattice has a greater coverage given the same parameters.

by [17]

$$\begin{aligned}\alpha_z^I &= \frac{\alpha_z}{1 - 2\alpha_z \frac{1}{\sqrt{20\pi}\epsilon_1 L^3}\left[S_{20} - \left(\frac{\epsilon_1-\epsilon_2}{\epsilon_1+\epsilon_2}\right)\tilde{S}_{20}^r\right]} \\ \alpha_\parallel^I &= \frac{\alpha_\parallel}{1 + \alpha_\parallel \frac{1}{\sqrt{20\pi}\epsilon_1 L^3}\left[S_{20} + \left(\frac{\epsilon_1-\epsilon_2}{\epsilon_1+\epsilon_2}\right)\tilde{S}_{20}^r\right]},\end{aligned} \tag{3.111}$$

for a regular array with a 4- or 6-fold symmetry. Here S_{20} and $\tilde{S}_{20}^r$ are *lattice sums*, depending only on the island lattice and defined by

$$S_{20} \equiv \sum_{i\neq 0}\left(\frac{L}{r}\right)^3 Y_2^0(\theta,\phi)\big|_{\mathbf{r}=\mathbf{R_i}}\,, \tag{3.112}$$

$$\tilde{S}_{20}^r \equiv \sum_{i\neq 0}\left(\frac{L}{r}\right)^3 Y_2^0(\theta,\phi)\big|_{\mathbf{r}=\mathbf{R_i^r}}\,, \tag{3.113}$$

where the sums are made over all other islands except the island centered at the origin. The vectors $\mathbf{R_i}$ and $\mathbf{R_i^r}$ are the positions of the center of island i and its mirror point, respectively.

3.5.2. Surface susceptibilities

As shown in Eqs. (2.14) – (2.17), it is the surface susceptibilities one needs in the end to calculate the film's amplitudes of reflection and transmission. When finding the surface susceptibilities of second order, δ and τ, it is necessary to

take into account the fact that the location of the multipole μ is not necessarily located at the *reference surface* used in the calculations in Sec. 2. Here the reference surface is located at the substrate surface, and the distance from there to the island multipole is $|d-\mu_z|$. It may then be shown that the surface susceptibilities of first and second order are given by [17]

$$\begin{aligned}
\beta &= \rho\alpha_z/\epsilon_1^2 \\
\gamma &= \rho\alpha_\parallel \\
\delta &= \rho\left[\left(|d-\mu_z|\right)\alpha_z + \left(|d-\mu_z|\right)\alpha_\parallel - \alpha_z^{10} - \alpha_\parallel^{10}\right]/\epsilon_1 \\
\tau &= \rho\left[\left(|d-\mu_z|\right)\alpha_\parallel - \alpha_\parallel^{10}\right]
\end{aligned} \tag{3.114}$$

where ρ is the number of islands per unit area (see Sec. 3.5.3). The polarizabilities (α) in Eq. (3.114) may be replaced with versions corrected for island-island interactions (α^I) from *e.g.* Eq. (3.111) if needed.

3.5.3. Derived parameters

In this section useful parameters of the supported island film will be defined, and equations for finding them will be derived.

Island volume and surface area

The volume inside spheroidal interface s and above the substrate may be found by integrating the volume of horizontal circular discs from $-R_\perp$ to d:

$$\begin{aligned}
V_s &= \int_{-R_\perp}^{d} \pi a^2\left(1+\xi_0^2\right)\left(1-\left(\frac{z}{a\xi_0}\right)^2\right)\mathrm{d}z \\
&= \frac{\pi}{3}a^3\xi_{0,s}\left(1+\xi_{0,s}^2\right)\left(2+3t_r^{(s)}-{t_r^{(s)}}^3\right) \\
&= \frac{\pi}{3}R_{\perp,s}R_{\parallel,s}^2\left(2+3t_r^{(s)}-{t_r^{(s)}}^3\right).
\end{aligned} \tag{3.115}$$

The volume of a coating (medium $2s+1$) may then be found as $V_s - V_{s+1}$. Similarly the surface area of a truncated spheroid s, including the area of the flat bottom base, may be found by integrating bands of circumference $2\pi x$ and

width $h_\eta \mathrm{d}\eta$:

$$\begin{aligned} S(R,t_r) =& \pi a^2 \left(1+\xi_{0,s}^2\right)\left(1-{t_r^{(s)}}^2\right) \\ &+ \int_{-1}^{t_r^{(s)}} \left(2\pi a\sqrt{1+\xi_{0,s}^2}\sqrt{1-\eta^2}\right)\left(a\sqrt{\frac{\xi_{0,s}^2+\eta^2}{1-\eta^2}}\right)\mathrm{d}\eta \\ =& \pi a^2\sqrt{\xi_{0,s}^2+1}\Bigg\{\sqrt{\xi_{0,s}^2+1}\left(2-{t_r^{(s)}}^2\right)+t_r^{(s)}\sqrt{{t_r^{(s)}}^2+\xi_{0,s}^2} \\ &+ \xi_{0,s}^2 \ln\left(\frac{\sqrt{{t_r^{(s)}}^2+\xi_{0,s}^2}+t_r^{(s)}}{\sqrt{1+\xi_{0,s}^2}-1}\right)\Bigg\}. \end{aligned} \tag{3.116}$$

This allows the calculation of the surface-to-volume ratio needed in *e.g.* the finite-size corrections to the dielectric function in Sec. 2.3.

Contact angle

The *contact angle* of an island is defined as shown in Fig. 3.7. It may be calculated as the angle between the unit vector in the x-direction and the unit vector in the η-direction at the point of truncation. The latter may be found as [26]

$$\widehat{\eta}|_{\phi=0} = -\widehat{x}\eta\sqrt{\frac{1+\xi^2}{\xi^2+\eta^2}} + \widehat{z}\xi\sqrt{\frac{1-\eta^2}{\xi^2+\eta^2}}, \tag{3.117}$$

allowing the calculation of the contact angle with

$$\cos\theta_c = \left.\frac{\widehat{x}\cdot\widehat{\eta}}{|\widehat{x}||\widehat{\eta}|}\right|_{\xi=\xi_0,\ \eta=t_r,\ \phi=0} = -t_r\sqrt{\frac{\xi_0^2+1}{\xi_0^2+t_r^2}}, \tag{3.118}$$

which reduces to $\cos\theta_c = -t_r$ for spheres ($\xi_0 \to \infty$) as expected.

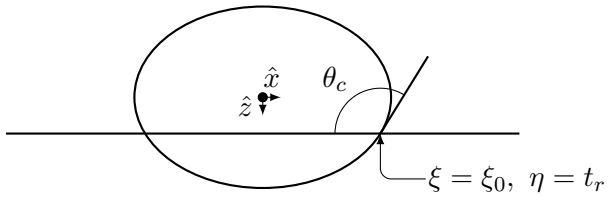

Figure 3.7.: Definition of the contact angle θ_c of a truncated spheroid.

Island density

The density (ρ) is the number of islands per unit area. By considering the geometries of the lattices (Fig. 3.6) it is found to be

$$\rho = \begin{cases} L^{-2} & \text{Square lattice} \\ \frac{2}{\sqrt{3}} L^{-2} & \text{Hexagonal lattice} \end{cases}, \tag{3.119}$$

where L is the center-to-center distance between nearest neighbors, *i.e.* the lattice constant.

Coverage

Coverage is a dimensionless quantity which can be defined as the fraction of the substrate area covered by the islands as seen from above the substrate surface. The area of a single island seen from above is πR_{app}^2, where R_{app} is given by:

$$R_{\text{app}} = \begin{cases} R_{\parallel,1} & t_r^{(1)} \geq 0 \\ R_{\parallel,1}\sqrt{1 - {t_r^{(1)}}^2} & t_r^{(1)} < 0 \end{cases}. \tag{3.120}$$

The coverage (Θ) is then given by:

$$\Theta = \pi R_{\text{app}}^2 \rho = \begin{cases} \pi \left(\frac{R_{\text{app}}}{L}\right)^2 & \text{Square lattice} \\ \frac{2\pi}{\sqrt{3}} \left(\frac{R_{\text{app}}}{L}\right)^2 & \text{Hexagonal lattice} \end{cases} \tag{3.121}$$

The coverage is maximally ($L = 2R_{\text{app}}$) 78.5% and 90.7% for the square and hexagonal lattices respectively. The latter is in fact the closest possible packing of monodisperse circles. In reality an even larger coverage can be achieved because of polydispersity. This high coverage case can probably not be accurately simulated by GranFilm, as the island-island interactions are only taken into account to dipolar (see Sec. 3.5.1) or quadrupolar [17] order.

Equivalent thickness

If the total volume of all the islands in the film was deposited uniformly instead of forming islands, it would form a layer with a certain thickness. This *equivalent thickness* is the total amount of deposited volume, divided by the area deposited on, and may be calculated as:

$$t_{\text{eq,tot}} = \rho V_1. \tag{3.122}$$

This parameter is useful because it is normally a known quantity in a deposition experiment. The equivalent thickness found by fitting the parameters of these calculations to a measured SDRS curve may then be compared with the known number, to assess the correctness of the model fit.

4. Special cases

To help verify the correctness of the theory derived in Sec. 3, it is useful to reduce the results to some special cases which have been calculated by others and see if they agree. In this section the results will be reduced to two different special cases: Section 4.1 will cover the case where the islands have no coatings, and where $\mu_z = 0$. This corresponds to the derivations done in the book by Bedeaux and Vlieger [17]. Section 4.2 reduces the results to the case where the islands are truncated spheres, not truncated spheroids. This must be done analytically, as the spherical limit of spheroids ($\xi_0 \to \infty,\ a \to 0$) can not be reached numerically in practice. The results from this should correspond to what is already implemented in the GranFilm code for coated spherical islands.

4.1. No coatings and centered multipole

With no coatings, the number of spheroidal interfaces is one, and thus the subscripts and superscripts with s will be dropped. With $S = 1$ and a centered island multipole, Eq. 3.107 reduces to

$$\begin{aligned} B^{(1)}_{\ell m} &= 0 \\ A^{(3)}_{\ell m} &= 0, \end{aligned} \tag{4.1}$$

which leaves $A^{(1)}_{\ell m}$ and $B^{(3)}_{\ell m}$ as the remaining unknown coefficients. An island multipole centered in the origin implies the following:

$$\begin{aligned} \mu_z &= 0 \\ \bar{\mu}_z &= 2d \end{aligned} \tag{4.2}$$

In this special case one may easily show that

$$V^m_{\ell\ell'}[\mu_z = 0, \xi](\eta_1, \eta_2) = Z^m_{\ell'}(\xi) Q^m_{\ell\ell'}(\eta_1, \eta_2), \tag{4.3}$$

and

$$W^m_{\ell\ell'}[\mu_z = 0, \xi](\eta_1, \eta_2) = X^m_{\ell'}(\xi) Q^m_{\ell\ell'}(\eta_1, \eta_2), \tag{4.4}$$

which may be used together with Eq. (3.90) to show that

$$\mathcal{I}^{m(1)}_{\ell\ell'}(t_r,\xi_0)=\frac{\xi_0^{\ell'+1}}{\zeta^m_{\ell\ell'}}\Bigg\{\frac{2\epsilon_1}{\epsilon_1+\epsilon_2}Z^m_{\ell'}(\xi_0)\delta_{\ell\ell'} + \frac{\epsilon_1-\epsilon_2}{\epsilon_1+\epsilon_2}\zeta^m_{\ell\ell'}\left[(-1)^{\ell'+m}V^m_{\ell\ell'}[\bar{\mu}_z,\xi_0](-1,t_r)-Z^m_{\ell'}(\xi_0)Q^m_{\ell\ell'}(-1,t_r)\right]\Bigg\}, \tag{4.5}$$

$$\mathcal{K}^{m(3)}_{\ell\ell'}(t_r,\xi_0)=\frac{\xi_0^{-\ell'}}{\zeta^m_{\ell\ell'}}\Bigg\{\frac{2\epsilon_3}{\epsilon_3+\epsilon_4}X^m_{\ell'}(\xi_0)\delta_{\ell\ell'} + \frac{\epsilon_3-\epsilon_4}{\epsilon_3+\epsilon_4}\zeta^m_{\ell\ell'}\left[(-1)^{\ell'+m}W^m_{\ell\ell'}[\bar{\mu}_z,\xi_0](-1,t_r)-X^m_{\ell'}(\xi_0)Q^m_{\ell\ell'}(-1,t_r)\right]\Bigg\}, \tag{4.6}$$

$$\begin{aligned}\mathcal{J}^{m(1)}_{\ell\ell'}(t_r,\xi_0)=\frac{\xi_0^{\ell'+1}}{\zeta^m_{\ell\ell'}}\epsilon_1\Bigg\{&\frac{2\epsilon_2}{\epsilon_1+\epsilon_2}\frac{\partial}{\partial\xi}\left[Z^m_{\ell'}(\xi)\right]|_{\xi=\xi_0}\delta_{\ell\ell'}\\ &+\frac{\epsilon_1-\epsilon_2}{\epsilon_1+\epsilon_2}\zeta^m_{\ell\ell'}\Bigg[\frac{\partial}{\partial\xi}\left[Z^m_{\ell'}(\xi_0)\right]|_{\xi=\xi_0}Q^m_{\ell\ell'}(-1,t_r)\\ &+(-1)^{\ell'+m}\frac{\partial}{\partial\xi}\left[V^m_{\ell\ell'}[\bar{\mu}_z,\xi_0](-1,t_r)\right]|_{\xi=\xi_0}\Bigg]\Bigg\},\end{aligned} \tag{4.7}$$

and

$$\begin{aligned}\mathcal{L}^{m(3)}_{\ell\ell'}(t_r,\xi_0)=\frac{\xi_0^{-\ell'}}{\zeta^m_{\ell\ell'}}\epsilon_3\Bigg\{&\frac{2\epsilon_4}{\epsilon_3+\epsilon_4}\frac{\partial}{\partial\xi}\left[X^m_{\ell'}(\xi)\right]|_{\xi=\xi_0}\delta_{\ell\ell'}\\ &+\frac{\epsilon_3-\epsilon_4}{\epsilon_3+\epsilon_4}\zeta^m_{\ell\ell'}\Bigg[\frac{\partial}{\partial\xi}\left[X^m_{\ell'}(\xi_0)\right]|_{\xi=\xi_0}Q^m_{\ell\ell'}(-1,t_r)\\ &+(-1)^{\ell'+m}\frac{\partial}{\partial\xi}\left[W^m_{\ell\ell'}[\bar{\mu}_z,\xi_0](-1,t_r)\right]|_{\xi=\xi_0}\Bigg]\Bigg\}.\end{aligned} \tag{4.8}$$

The linear systems of equations in Eqs. (3.104) and (3.105) are in this case

reduced to

$$\sum_{\ell'=1}^{M} \zeta_{\ell\ell'}^{m} R_{\perp}^{-\ell'-2} \mathcal{I}_{\ell\ell'}^{m(1)}(t_r,\xi_0) A_{\ell' m}^{(1)} - \sum_{\ell'=1}^{M} \zeta_{\ell\ell'}^{m} R_{\perp}^{\ell'-1} \mathcal{K}_{\ell\ell'}^{m(3)}(t_r,\xi_0) B_{\ell' m}^{(3)}$$
$$= E_0 \Bigg\{ \cos\theta_0 \sqrt{\frac{4\pi}{3}} \Bigg\{ \frac{\epsilon_1}{\epsilon_2} \xi_0^{-1} X_1^0(\xi_0) \delta_{\ell 1} + \left(\frac{\epsilon_1}{\epsilon_2} - 1 \right) \Big[\sqrt{3} t_r \zeta_{\ell 0}^0 Q_{\ell 0}^0(-1,t_r)$$
$$- \xi_0^{-1} X_1^0(\xi_0) \zeta_{\ell 1}^0 Q_{\ell 1}^0(-1,t_r) \Big] \Bigg\} \delta_{m0} - \sqrt{\frac{2\pi}{3}} \sin\theta_0 \mathrm{e}^{-i\phi_0} \xi_0^{-1} X_1^1(\xi_0) \delta_{\ell 1} \delta_{m1} \Bigg\},$$
$$\forall \quad \ell = 1,2,3,...,M; \ m = 0,1 \tag{4.9}$$

and

$$\sum_{\ell'=1}^{M} \zeta_{\ell\ell'}^{m} R_{\perp}^{-\ell'-2} \mathcal{J}_{\ell\ell'}^{m(1)}(t_r,\xi_0) A_{\ell' m}^{(1)} - \sum_{\ell'=1}^{M} \zeta_{\ell\ell'}^{m} R_{\perp}^{\ell'-1} \mathcal{L}_{\ell\ell'}^{m(3)}(t_r,\xi_0) B_{\ell' m}^{(3)}$$
$$= \xi_{0,1}^{-1} E_0 \Bigg\{ \sqrt{\frac{4\pi}{3}} \epsilon_1 \cos\theta_0 \left. \frac{\partial X_1^0(\xi)}{\partial \xi} \right|_{\xi=\xi_{0,1}} \delta_{\ell 1} \delta_{m0}$$
$$- \sqrt{\frac{2\pi}{3}} \sin\theta_0 \mathrm{e}^{-i\phi_0} \left. \frac{\partial X_1^1(\xi)}{\partial \xi} \right|_{\xi=\xi_{0,1}} \Big[(\epsilon_1 - \epsilon_2) \zeta_{\ell 1}^1 Q_{\ell 1}^1(-1,t_r^{(1)}) + \epsilon_2 \delta_{\ell 1} \Big] \delta_{m1} \Bigg\}.$$
$$\forall \quad \ell = 1,2,3,...,M; \ m = 0,1 \tag{4.10}$$

Given only a single spheroidal interface there are only two unknown constant terms, namely $\psi_0^{(1)}$ and $\psi_0^{(3)}$. As usual the former may simply be set to zero, and the latter may then be calculated through Eq. (3.106), which in this case

reduces to

$$\begin{aligned}
\psi_0^{(3)} =& \frac{1}{2\sqrt{\pi}} \sum_{\ell=1}^{M} \zeta_{0\ell}^0 R_\perp^{-\ell-1} \mathcal{I}_{0\ell}^{0(1)}(t_r, \xi_0) A_{\ell 0}^{(1)} - \frac{1}{2\sqrt{\pi}} \sum_{\ell=1}^{M} \zeta_{0\ell}^0 R_\perp^{\ell} \mathcal{K}_{0\ell}^{0(3)}(t_r, \xi_0) B_{\ell 0}^{(3)} \\
& - E_0 \cos\theta_0 R_\perp \left(\frac{\epsilon_1}{\epsilon_2} - 1 \right) \frac{1}{4} (1 - t_r)^2 \\
=& \frac{1}{2\sqrt{\pi}} \sum_{\ell=1}^{M} R_\perp^{-\ell-1} \left(\frac{\epsilon_1 - \epsilon_2}{\epsilon_1 + \epsilon_2} \right) \zeta_{0\ell}^0 \xi_0^{\ell+1} \\
& \quad \times \left[(-1)^\ell V_{0\ell}^0[\bar{\mu}_z, \xi_0](-1, t_r) - Z_\ell^0(\xi_0) Q_{0\ell}^0(-1, t_r) \right] A_{\ell 0}^{(1)} \\
& - \frac{1}{2\sqrt{\pi}} \sum_{\ell=1}^{M} R_\perp^{\ell} \left(\frac{\epsilon_3 - \epsilon_4}{\epsilon_3 + \epsilon_4} \right) \zeta_{0\ell}^0 \xi_0^{-\ell} \\
& \quad \times \left[(-1)^\ell W_{0\ell}^0[\bar{\mu}_z, \xi_0](-1, t_r) - X_\ell^0(\xi_0) Q_{0\ell}^0(-1, t_r) \right] B_{\ell 0}^{(3)} \\
& - E_0 \cos\theta_0 R_\perp \left(\frac{\epsilon_1}{\epsilon_2} - 1 \right) \frac{1}{4} (1 - t_r)^2 . \qquad (4.11)
\end{aligned}$$

These equations, (4.9), (4.10) and (4.11), agree with the results for films of truncated spheroids found in [17], as they should.

4.2. The spherical limit

The spherical limit of a spheroid is given by

$$\begin{aligned}
a &\to 0 \\
\xi_0 &\to \infty \\
a\xi_{0,s} &\to R_s, \qquad (4.12)
\end{aligned}$$

where R_s is the radius of the sphere. The limit of the corresponding spheroidal coordinate system with the same focal radius a is then

$$\begin{aligned}
\xi &\simeq \frac{r}{a} \\
\eta &\simeq \cos\theta \\
\phi &= \phi, \qquad (4.13)
\end{aligned}$$

where (r, θ, ϕ) are the regular coordinates of a spherical coordinate system.

As mentioned in Sec. 3.4.1 it can be shown that[17]

$$\begin{aligned}
X_\ell^m(\xi, a) &\simeq r^\ell \\
Z_\ell^m(\xi, a) &\simeq r^{-\ell-1}, \qquad (4.14)
\end{aligned}$$

which means that the dimensionless versions of Eqs. (3.66) and (3.67) have the following asymptotic behavior:

$$\begin{aligned} X_\ell^m(\xi) &\simeq a^{-\ell} r^\ell \\ Z_\ell^m(\xi) &\simeq a^{\ell+1} r^{-\ell-1}. \end{aligned} \tag{4.15}$$

The above relations may be used to find the following relations in the spherical limit:

$$\begin{aligned} Q_{\ell\ell'}^m(\eta_1,\eta_2) &\simeq \int_{x_1}^{x_2} \mathrm{d}x P_\ell^m(x) P_{\ell'}^m(x) \\ \xi_{0,s}^{\ell'+1} V_{\ell\ell'}^m[\kappa_z,\xi_{0,s}](\eta_1,\eta_2) &\simeq I_{\ell\ell'}^m[R_s,\kappa_z,-\ell'-1](x_1,x_2) \\ \xi_{0,s}^{-\ell'} W_{\ell\ell'}^m[\kappa_z,\xi_{0,s}](\eta_1,\eta_2) &\simeq I_{\ell\ell'}^m[R_s,\kappa_z,\ell'](x_1,x_2) \\ \xi_{0,s}^{\ell'+2} \frac{\partial}{\partial\xi} \left\{V_{\ell\ell'}^m[\kappa_z,\xi](\eta_1,\eta_2)\right\}\big|_{r=R_s} &\simeq J_{\ell\ell'}^m[R_s,\kappa_z,-\ell'-1](x_1,x_2) \\ \xi_{0,s}^{-\ell'+1} \frac{\partial}{\partial\xi} \left\{W_{\ell\ell'}^m[\kappa_z,\xi](\eta_1,\eta_2)\right\}\big|_{r=R_s} &\simeq J_{\ell\ell'}^m[R_s,\kappa_z,\ell'](x_1,x_2). \end{aligned} \tag{4.16}$$

The new integrals I and J are defined as

$$\begin{aligned} I_{\ell\ell'}^m[R_s,\kappa_z,\alpha](x_1,x_2) &\equiv \int_{x_1}^{x_2} \mathrm{d}x P_\ell^m(x) P_{\ell'}^m(x_\kappa) \left(\frac{r_\kappa}{R_s}\right)^\alpha \\ J_{\ell\ell'}^m[R_s,\kappa_z,\alpha](x_1,x_2) &\equiv R_s \frac{\partial}{\partial r} \left\{\int_{x_1}^{x_2} \mathrm{d}x P_\ell^m(x) P_{\ell'}^m(x_\kappa) \left(\frac{r_\kappa}{R_s}\right)^\alpha\right\}\Big|_{r=R_s}, \end{aligned} \tag{4.17}$$

where $x_1 = \cos\theta_1 \simeq \eta_1$ and $x_2 = \cos\theta_2 \simeq \eta_2$. The variable x_κ is equal to $\cos\theta_\kappa$, where $\theta_\kappa = \theta_\kappa(r,\theta)$ is the polar angle of the point (r,θ,ϕ) with respect to coordinate system κ. Similarly, the variable $r_\kappa = r_\kappa(r,\theta)$ is the distance to the point (r,θ,ϕ) from the origin of coordinate system κ. Both depend on the variable of integration x, since $x = \cos\theta$.

Using that $\xi_{0,1}^{-1} X_1^m(\xi_{0,1}) \simeq 1$, the linear systems of equations in Eqs. (3.104)

and (3.105), and Eq. (3.106) for the constant terms, may now be written as

$$\sum_{\ell'=1}^{M}\zeta_{\ell\ell'}^{m}R_s^{-\ell'-2}\left[\mathcal{I}_{\ell\ell'}^{m(2s-1)}(t_r^{(s)},\xi_{0,s})A_{\ell'm}^{(2s-1)}-\mathcal{I}_{\ell\ell'}^{m(2s+1)}(t_r^{(s)},\xi_{0,s})A_{\ell'm}^{(2s+1)}\right]$$
$$+\sum_{\ell'=1}^{M}\zeta_{\ell\ell'}^{m}R_s^{\ell'-1}\left[\mathcal{K}_{\ell\ell'}^{m(2s-1)}(t_r^{(s)},\xi_{0,s})B_{\ell'm}^{(2s-1)}-\mathcal{K}_{\ell\ell'}^{m(2s+1)}(t_r^{(s)},\xi_{0,s})B_{\ell'm}^{(2s+1)}\right]$$
$$=\delta_{s1}E_0\Bigg[\cos\theta_0\sqrt{\frac{4\pi}{3}}\Bigg\{\frac{\epsilon_1}{\epsilon_2}\delta_{\ell1}+\left(\frac{\epsilon_1}{\epsilon_2}-1\right)\left[\sqrt{3}t_r^{(1)}\zeta_{\ell0}^{0}Q_{\ell0}^{0}(-1,t_r^{(1)})\right.$$
$$\left.-\zeta_{\ell1}^{0}Q_{\ell1}^{0}(-1,t_r^{(1)})\right]\Bigg\}\delta_{m0}-\sqrt{\frac{2\pi}{3}}\sin\theta_0\mathrm{e}^{-i\phi_0}\delta_{\ell1}\delta_{m1}\Bigg]$$
$$\forall\quad s=1,2,3,...,S;\ \ell=1,2,3,...,M;\ m=0,1, \tag{4.18}$$

$$\sum_{l'=1}^{M}\zeta_{\ell\ell'}^{m}R_s^{-\ell'-2}\left[\xi_{0,s}\mathcal{J}_{\ell\ell'}^{m(2s-1)}(t_r^{(s)},\xi_{0,s})A_{\ell'm}^{(2s-1)}-\xi_{0,s}\mathcal{J}_{\ell\ell'}^{m(2s+1)}(t_r^{(s)},\xi_{0,s})A_{\ell'm}^{(2s+1)}\right]$$
$$+\sum_{l'=1}^{M}\zeta_{\ell\ell'}^{m}R_s^{\ell'-1}\left[\xi_{0,s}\mathcal{L}_{\ell\ell'}^{m(2s-1)}(t_r^{(s)},\xi_{0,s})B_{\ell'm}^{(2s-1)}-\xi_{0,s}\mathcal{L}_{\ell\ell'}^{m(2s+1)}(t_r^{(s)},\xi_{0,s})B_{\ell'm}^{(2s+1)}\right]$$
$$=\delta_{s1}E_0\Bigg\{\sqrt{\frac{4\pi}{3}}\epsilon_1\cos\theta_0\delta_{\ell1}\delta_{m0}$$
$$-\sqrt{\frac{2\pi}{3}}\sin\theta_0\mathrm{e}^{-i\phi_0}\left[(\epsilon_1-\epsilon_2)\zeta_{\ell1}^{1}Q_{\ell1}^{1}(-1,t_r^{(1)})+\epsilon_2\delta_{\ell1}\right]\delta_{m1}\Bigg\}$$
$$\forall\quad s=1,2,3,...,S;\ \ell=1,2,3,...,M;\ m=0,1, \tag{4.19}$$

and

$$\left[\psi_0^{(2s+1)}-\psi_0^{(2s-1)}\right]$$
$$=\frac{1}{2\sqrt{\pi}}\sum_{\ell=1}^{M}\zeta_{0\ell}^{0}R_s^{-\ell-1}\left[\mathcal{I}_{0\ell}^{0(2s-1)}(t_r^{(s)},\xi_{0,s})A_{\ell0}^{(2s-1)}-\mathcal{I}_{0\ell}^{0(2s+1)}(t_r^{(s)},\xi_{0,s})A_{\ell0}^{(2s+1)}\right]$$
$$+\frac{1}{2\sqrt{\pi}}\sum_{\ell=1}^{M}\zeta_{0\ell}^{0}R_s^{\ell}\left[\mathcal{K}_{0\ell}^{0(2s-1)}(t_r^{(s)},\xi_{0,s})B_{\ell0}^{(2s-1)}-\mathcal{K}_{0\ell}^{0(2s+1)}(t_r^{(s)},\xi_{0,s})B_{\ell0}^{(2s+1)}\right]$$
$$+\delta_{s1}E_0R_1\cos\theta_0\left(\frac{\epsilon_1}{\epsilon_2}-1\right)$$
$$\times\left\{\frac{1}{\sqrt{3}}\zeta_{01}^{0}Q_{01}^{0}(-1,t_r^{(1)})+t_r^{(1)}\left(1-\zeta_{00}^{0}Q_{00}^{0}(-1,t_r^{(1)})\right)\right\}$$
$$\forall\quad s=1,2,3,...,S, \tag{4.20}$$

where

$$\mathcal{I}^{m(i)}_{\ell\ell'}(t^{(s)}_r,\xi_{0,s}) \simeq \mathcal{R}_i\Bigg[- I^m_{\ell\ell'}[R_s,\mu_z,-\ell'-1](-1,t^{(s)}_r) + (-1)^{\ell'+m} I^m_{\ell\ell'}[R_s,\bar{\mu}_z,-\ell'-1](-1,t^{(s)}_r) + \frac{2\epsilon_i}{\epsilon_i-\epsilon_{i+1}} I^m_{\ell\ell'}[R_s,\mu_z,-\ell'-1](-1,1)\Bigg], \tag{4.21}$$

$$\mathcal{K}^{m(i)}_{\ell\ell'}(t^{(s)}_r,\xi_{0,s}) \simeq \mathcal{R}_i\Bigg[- I^m_{\ell\ell'}[R_s,\mu_z,\ell'](-1,t^{(s)}_r) + (-1)^{\ell'+m} I^m_{\ell\ell'}[R_s,\bar{\mu}_z,\ell'](-1,t^{(s)}_r) + \frac{2\epsilon_i}{\epsilon_i-\epsilon_{i+1}} I^m_{\ell\ell'}[R_s,\mu_z,\ell'](-1,1)\Bigg], \tag{4.22}$$

$$\xi_{0,s}\mathcal{J}^{m(i)}_{\ell\ell'}(t^{(s)}_r,\xi_{0,s}) \simeq \epsilon_i\mathcal{R}_i\Bigg[J^m_{\ell\ell'}[R_s,\mu_z,-\ell'-1](-1,t^{(s)}_r) + (-1)^{\ell'+m} J^m_{\ell\ell'}[R_s,\bar{\mu}_z,-\ell'-1](-1,t^{(s)}_r) + \frac{2\epsilon_{i+1}}{\epsilon_i-\epsilon_{i+1}} J^m_{\ell\ell'}[R_s,\mu_z,-\ell'-1](-1,1)\Bigg], \tag{4.23}$$

and

$$\xi_{0,s}\mathcal{L}^{m(i)}_{\ell\ell'}(t^{(s)}_r,\xi_{0,s}) \simeq \epsilon_1\mathcal{R}_i\Bigg[J^m_{\ell\ell'}[R_s,\mu_z,\ell'](-1,t^{(s)}_r) + (-1)^{\ell'+m} J^m_{\ell\ell'}[R_s,\bar{\mu}_z,\ell'](-1,t^{(s)}_r) + \frac{2\epsilon_{i+1}}{\epsilon_i-\epsilon_{i+1}} J^m_{\ell\ell'}[R_s,\mu_z,\ell'](-1,1)\Bigg]. \tag{4.24}$$

The above equations for the spherical limit agrees with the equations previously implemented in GranFilm. Even though the spheroidal equations are a generalization, the equations in this section are still needed in practice since the spherical limit of the spheroidal equations cannot be reached numerically simply by letting $\xi_0 \to \infty,\ a \to 0,\ a\xi_0 \to R$.

5. Numerics

This section begins by covering the numerical implementation of the results derived in Sec. 3 as a part of the GranFilm software[1]. It then proceeds to cover the results from the numerical tests performed to assess the correctness of the implementation.

5.1. Implementation

The equations derived in Sec. 3 were implemented and integrated into the existing framework of the GranFilm 2.0 software, which already supported calculations on coated spherical islands, but not spheroidal ones. Equations (3.104) and (3.105) are implemented in slightly modified dimensionless forms, as detailed in App. A. Firstly, all the integrals up to multipole order M are calculated based on the island geometry (see App. B). The associated Legendre functions and their derivatives are calculated to arbitrary degree and order through the recurrence relations in Eqs. (B.12) and (B.13), while using the spheroidal coordinate transformations (Eqs. (3.25) and (3.26)) and their derivatives (Eq. (B.8)). It is worth noting that the associated Legendre functions of the second kind (Q_ℓ^m) had to be calculated with quadruple precision to get good behavior when approaching the spherical limit, because of severe roundoff errors when calculating $Q_\ell^m(i\xi)$ for large ξ.

When the integrals have been calculated, the systems of equations for $m = 0$ and $m = 1$ shown in Eqs. (A.6) and (A.7) are set up and solved for a range of photon energies. The photon energy comes into play in the equations through the frequency dependence of the dielectric functions ϵ for the different materials.[2] For an illustration on how the matrix is set up, see the example in App. C. After solving these systems of equations one has a set of normalized expansion coefficients $\widehat{A}_{\ell m}^{(i)}$ and $\widehat{B}_{\ell m}^{(i)}$ for each photon energy. These are used to calculate island polarizabilities through Eq. (A.2), which may then be corrected for island-island interactions as shown in Sec. 3.5.1. The polarizabilities are used to find the normalized first order surface susceptibilities $\widehat{\gamma}$ and $\widehat{\beta}$ (A.3), which are finally used to find the amplitudes of reflection and transmission

[1] More technical details on the implementation may be found in the appendices.

[2] The photon energy also comes into play later as ω in the equations relating the surface susceptibilities to the amplitudes of reflection and transmission (2.14) – (2.17).

through Eqs. (2.14) – (2.17).

Calculating and inspecting the SDRS spectrum is not enough to verify the correctness of the implementation though. One should also inspect the potential in the near-field, to check whether or not the boundary conditions have been sufficiently satisfied for the multipole order M chosen. As mentioned in Sec. 3.4.1, the uniqueness theorem guarantees that a potential on the form of a general solution which satisfies all the boundary conditions on the spheroidal interfaces *must* be the one and only correct solution. Thus inspecting the potential serves as the ultimate test for the correctness of the results, within the chosen assumptions. To enable these tests, GranFilm 2.0 was expanded with a module which may use the multipole coefficients of all orders up to M to calculate the potential at any set of points the user specifies, at any photon energy the user wishes to inspect the potential at. This allows for both plotting of the potential in a plane and specifically calculating the errors in the boundary conditions. See App. D for details involving the implementation of this.

5.2. Numerical tests

In this section a test case consisting of truncated coated spheroidal islands supported on a dielectric substrate is selected, and the newly expanded GranFilm software is used to simulate the SDRS response. The test case consists of islands of shape $R_{\perp,1} = 6.0\,\text{nm}$ and $R_{\parallel,1} = 8.0\,\text{nm}$ arranged in a hexagonal array with lattice constant $L = 20\,\text{nm}$. The islands consist of an Ag core with a size such that $\chi_2 = 0.7$, coated with Ag_2O (See Sec. 6.1). The islands are supported on an Al_2O_3 substrate and truncated by $t_r^{(1)} = 0.25$. The incoming radiation is p-polarized, with incident angles $\theta = 45°$ and $\phi = 0°$. In this test no finite-size corrections are made to the dielectric functions, nor are the polarizabilities corrected for island-island interactions. These corrections are not needed here as the point of this test is to verify the correctness of the code, not to compare with experimental data.

The differential reflectivity (SDRS) calculated for this test case with a multipole order $M = 16$ may be seen in Fig. 5.1. Further, the calculated polarizabilities are presented in Figs. 5.2 (dipolar) and 5.3 (quadrupolar).

To assess whether or not these results may be trusted, a number of inspections and numerical tests will follow. This section will mainly define the tests and present their results, while most of the interpretations and discussions will be left for Sec. 7. In Sec. 5.2.1 the potential is inspected at key energies to verify that its continuity looks reasonable. In Sec. 5.2.2 concrete measures of the errors in the boundary conditions at a given point on one of the spheroidal interfaces are defined. These measures $\mathcal{E}_\psi$ and $\mathcal{E}_{\partial_n\psi}$ are used in following sec-

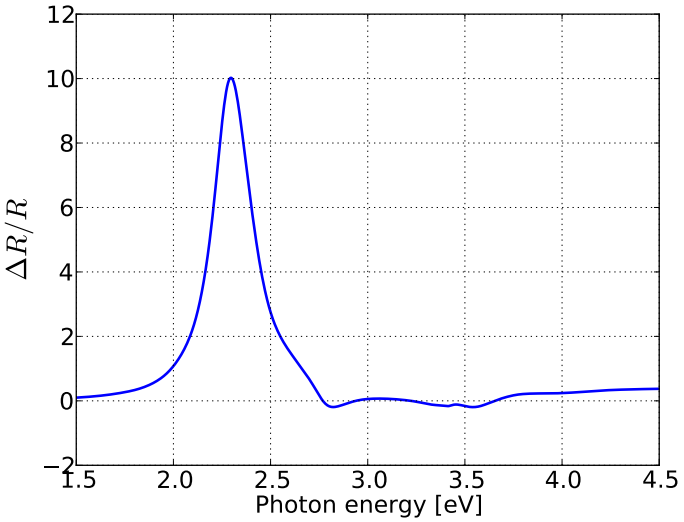

Figure 5.1.: The SDRS curve calculated for the test case.

tions to analyze the errors in a more rigorous way than simple inspection. In Sec. 5.2.3 the precise values for ψ and $\epsilon\partial_n\psi$ at the main resonance on both sides of the spheroidal interfaces are shown, as well as the corresponding boundary condition errors. How the average of these errors develop as the multipole order M of the calculation increases is examined in Sec. 5.2.4. The magnitude of these errors depends greatly on whether or not one is at a resonance energy. Section 5.2.5 examines this behavior across the energy range of interest. In Sec. 5.2.6, it is verified that the SDRS curve calculated for spheroidal islands agrees with what one gets from the existing code for spherical islands, as the islands get more and more spherical.

5.2.1. Inspecting the potential

In this section the potential in the $y = 0$ plane is plotted for photon energies where one or more of the polarizabilities have an especially large magnitude (see Figs. 5.2 and 5.3). This is done to reveal what kind of resonances create the features of the polarizability curves, and thus eventually the measurable SDRS curve.

Figure 5.4 shows the real part of the potential at the energy of the peak positive value of the real part of the parallel dipolar polarizability (2.225 eV). This also coincides with the peak of the real part of the parallel quadrupolar polarizability. Figure 5.5 shows real part of the potential at the energy of the peak negative values of the same two polarizabilities (2.380 eV), which corresponds to the same resonance, but with reversed polarization. Figure 5.6

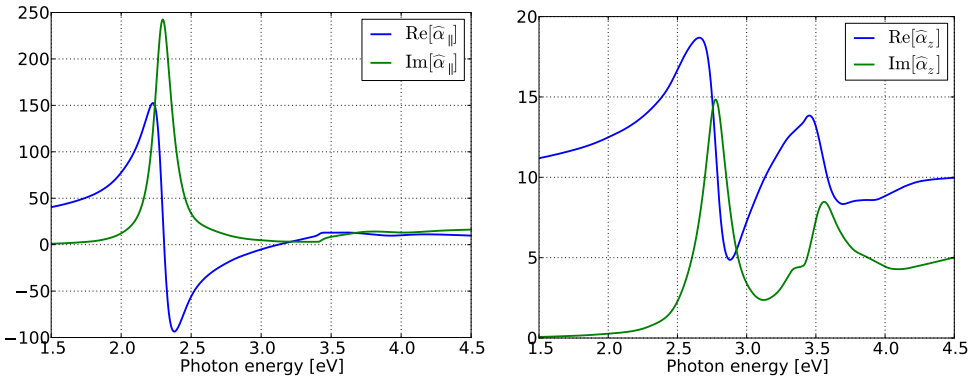

(a) (b)

Figure 5.2.: The (a) parallel and (b) perpendicular dipolar island polarizabilities calculated for the test case, normalized as shown in Eq. (A.2).

shows equivalent plots for the resonance of the perpendicular polarizabilities (2.660 eV and 2.880 eV).

At the center of the frequency area of the resonance, the imaginary part of the corresponding polarizability has its peak value. The imaginary part of the potential at the energy of the peak value of the imaginary part of the parallel and perpendicular polarizabilities are plotted in Figs. 5.7 and 5.8 respectively.

The lack of any notable quadrupolar excitations visible in most of the potential plots raises the question of whether this was caused by the elongated spheroidal shape of the island. To answer this, a spherical case which is similar to the above test case is run, where both radii are 6 nm. A visibly quadrupolar response in Re[ψ] for this spherical case may be seen in Fig. 5.9.

5.2.2. Measures of error in boundary conditions

Since a potential which satisfies the boundary conditions (3.29) everywhere at all the spheroidal interfaces is theoretically the one and only correct potential, the degree to which the boundary conditions are satisfied by a calculation to a finite multipole order M is a measure of the calculation's correctness. In this section a nondimensional measure of the errors in the two boundary conditions at a point on one of the spheroidal interfaces will be introduced. They are similar to the measures used in [28], though here generalized for use with coated islands as well. The measures of errors for the first (3.29a) and

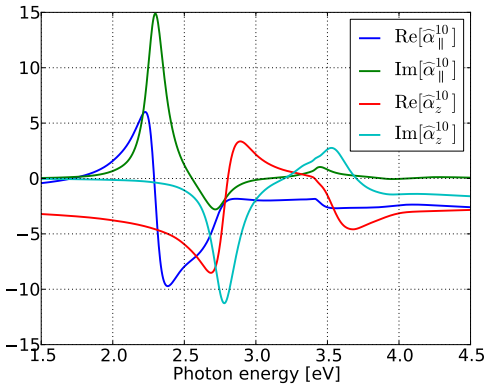

Figure 5.3.: The parallel and perpendicular quadrupolar island polarizabilities calculated for the test case, normalized as shown in Eq. (A.2).

second (3.29b) boundary conditions are as follows:

$$\begin{aligned}\mathcal{E}_{\psi}(\mathbf{r}_s) &= \frac{\psi_+(\mathbf{r}_s) - \psi_-(\mathbf{r}_s)}{\max_{\mathbf{r}_1} |\psi_{\mathrm{inc}}(\mathbf{r}_1)|}, \\ \mathcal{E}_{\partial_n\psi}(\mathbf{r}_s) &= \frac{\epsilon_+\partial_n\psi_+(\mathbf{r}_s) - \epsilon_-\partial_n\psi_-(\mathbf{r}_s)}{\max_{\mathbf{r}_1} |\epsilon_1\partial_n\psi_{\mathrm{inc}}(\mathbf{r}_1)|},\end{aligned} \tag{5.1}$$

where $\mathbf{r}_s$ is a point on spheroidal interface s ($\xi = \xi_{0,s}$). The subscripts $+$ and $-$ indicate quantities just outside and just inside the spheroidal interface respectively. The fact that the incident potential ψ_{inc} is used to construct denominators does not make $\mathcal{E}_{\psi}$ and $\mathcal{E}_{\partial_n\psi}$ any measures of relative error, but they are nondimensional measures which are independent of the strength of the incident field E_0, and are useful for examining *e.g.* convergence.

The question now is how one may calculate these denominators. If $t_r^{(1)} > 0$, which will be the case for all these tests, the point on the island with the largest value of ψ_{inc} will have the coordinate η equal to:

$$\eta_{\max} = -\frac{\xi_{0,1}\cos\theta_0}{\sqrt{\sin^2\theta_0 + \xi_{0,1}^2}}. \tag{5.2}$$

This is found as the point on the spheroidal surface above the substrate where the unit vector $\widehat{\eta}$ [26] is perpendicular to $\mathbf{E_0}$. The first denominator in Eq. (5.1) can then be found to be:

$$\begin{aligned}\max_{\mathbf{r}_1} |\psi_{\mathrm{inc}}(\mathbf{r}_1)| &= |\mathbf{r}_{\max}\cdot\mathbf{E}_0| \\ &= |E_0\left(x_{\max}\sin\theta_0\cos\phi_0 + y_{\max}\sin\theta_0\sin\phi_0 + z_{\max}\cos\theta_0\right)|,\end{aligned} \tag{5.3}$$

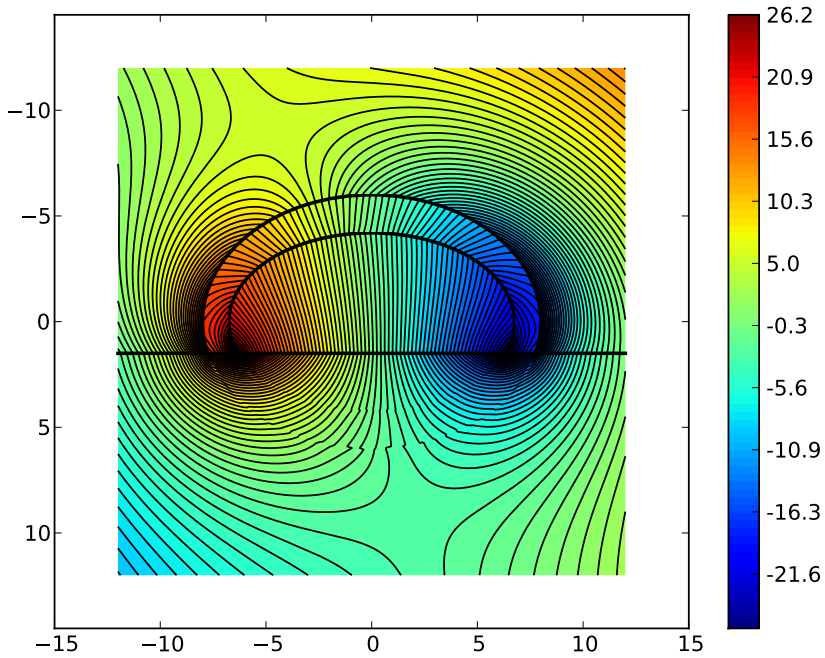

Figure 5.4.: The equipotential lines of $\mathrm{Re}[\psi]$ at photon energy $E = 2.225\,\mathrm{eV}$, which is the position of the peak values of $\mathrm{Re}\left[\alpha_{\parallel}\right]$ and $\mathrm{Re}[\alpha_{\parallel}^{10}]$.

where $x_{\max}, y_{\max}, z_{\max}$ are found from the transformations in Eq. (3.13) using $\xi = \xi_{0,1}$, $\eta = \eta_{\max}$ (5.2) and $\phi = \phi_0$.

Since the incident electric field is constant, the gradient of ψ_{inc} is also constant and equal in magnitude to $\mathbf{E}_0$. The quantity $|\partial_n \psi_{\mathrm{inc}}(\mathbf{r}_1)|$ reaches its maximum at the point defined in Eq. (5.2), when the gradient of the incident potential is perpendicular to the interface. This maximum value is E_0, and thus the second denominator in Eq. (5.1) is given by:

$$\max_{\mathbf{r}_1} |\epsilon_1 \partial_n \psi_{\mathrm{inc}}(\mathbf{r}_1)| = |\epsilon_1| E_0. \tag{5.4}$$

5.2.3. Errors in boundary conditions

Using the new module for calculating the potential at an arbitrary set of points, the error measures may now be evaluated approximately at points along the spheroidal interfaces. The quantity $\mathcal{E}_\psi$ is found by calculating ψ at two points, one just outside the interface and one just inside the interface. The quantity $\mathcal{E}_{\partial_n \psi}$ is found by calculating ψ at four points, two just outside the interface and two just inside, enabling the evaluation of $\partial_n \psi$ at both sides of the interface through a finite-difference approximation. Using a finite-difference approximation should not really be necessary, as the expansions are known analytically

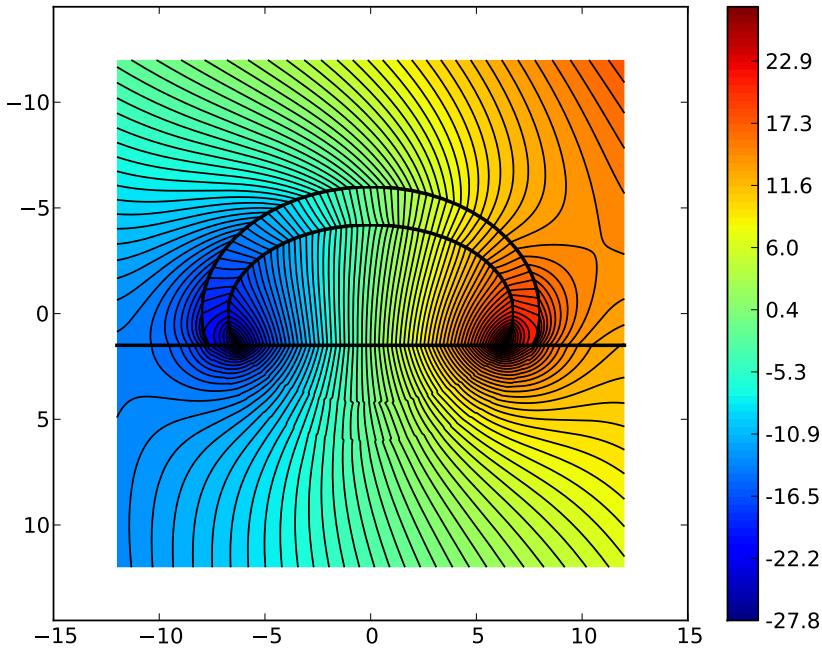

Figure 5.5.: The equipotential lines of $\mathrm{Re}[\psi]$ at photon energy $E = 2.380\,\mathrm{eV}$, which is the position of the peak negative values of $\mathrm{Re}\left[\alpha_{\parallel}\right]$ and $\mathrm{Re}[\alpha_{\parallel}^{10}]$.

given the expansion coefficients. However, the finite-difference approximation was found to be very well behaved, so it was not deemed necessary to spend extra time implementing the exact approach.

To examine the errors in this test case, the quantities ψ, $\epsilon\partial_n\psi$, $\mathcal{E}_\psi$ and $\mathcal{E}_{\partial_n\psi}$ are evaluated along the spheroidal interfaces in the $y = 0$ plane at points evenly spaced in $\arccos\eta$. The multipole order used in the calculations is $M = 16$. Here the errors at the energy corresponding to the peak of $\alpha_{\parallel}$ (2.225 eV) are examined, as this is the main resonance and thus a energy where the most significant error may be expected. Figures 5.10 and 5.11 display the errors in both boundary conditions at the outer air-Ag_2O interface ($s = 1$). Figures 5.12 and 5.13 show the same, but now evaluated at the inner Ag_2O-Ag interface ($s = 2$). These four groups of figures may be compared with Fig. 5.4, as the latter is taken from the exact same simulation case, and also plotted in the $y = 0$ plane. Only the real parts are shown here, but both real and imaginary components of the error will be considered in Sec. 5.2.4.

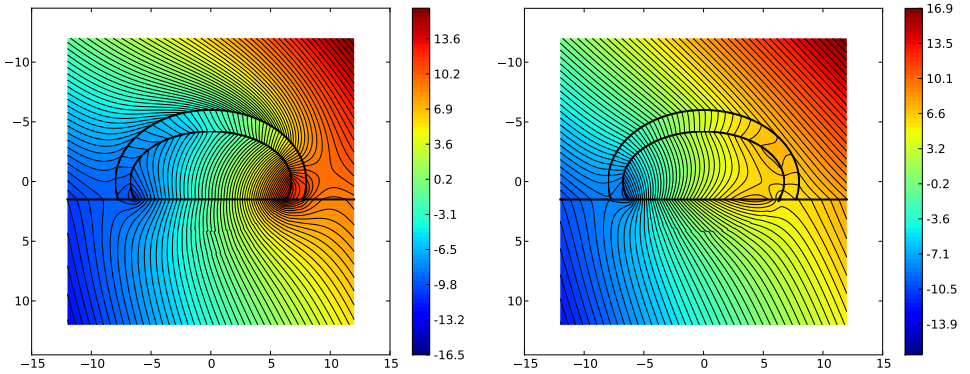

(a) (b)

Figure 5.6.: The equipotential lines of Re[ψ] at photon energy a) $E = 2.660\,\mathrm{eV}$ and b) $E = 2.880\,\mathrm{eV}$, which are the positions of the peak positive and negative values, respectively, of Re $[\alpha_z]$ and Re$[\alpha_z^{10}]$.

5.2.4. Convergence tests

Theoretically the calculated potential should be an exact solution of the Laplace equation (3.27) if one lets the multipole order of the calculation M approach infinity. Doing this is obviously impossible in practice, but one should be able to observe convergence towards an exact solution as M is made larger. Firstly one may verify that the response seen in the far-field (SDRS signal) converges towards a single curve. Such a test is shown in Fig. 5.14, where it is found that the SDRS signal appears to converge quite well within reaching a multipole order of $M = 10$.

Convergence of the SDRS curve is no guarantee that the calculated potential converges towards an exact solution however. Convergence of the latter kind would appear through a decrease in the average absolute errors in both boundary conditions at all spheroidal interfaces as M is increased. This is tested for this case at two different energies by examining the evolution of the quantities $\langle|\mathcal{E}|\rangle$, which is the average of the absolute values of the indicated complex error measure from Eq. (5.1). The average is found by summing the absolute errors at points along the spheroidal interface (in the $y = 0$ plane) evenly spaced in $\arccos\eta$, and dividing by the number of measured points. Firstly the convergence is examined at the main resonance, specifically at $E = 2.225\,\mathrm{eV}$ where $\alpha_{\|}$ has its peak value. This result is shown in Fig. 5.15. Secondly, the same test is performed at $E = 4.5\,\mathrm{eV}$, an energy with some distance from any resonances. This result is shown in Fig. 5.16.

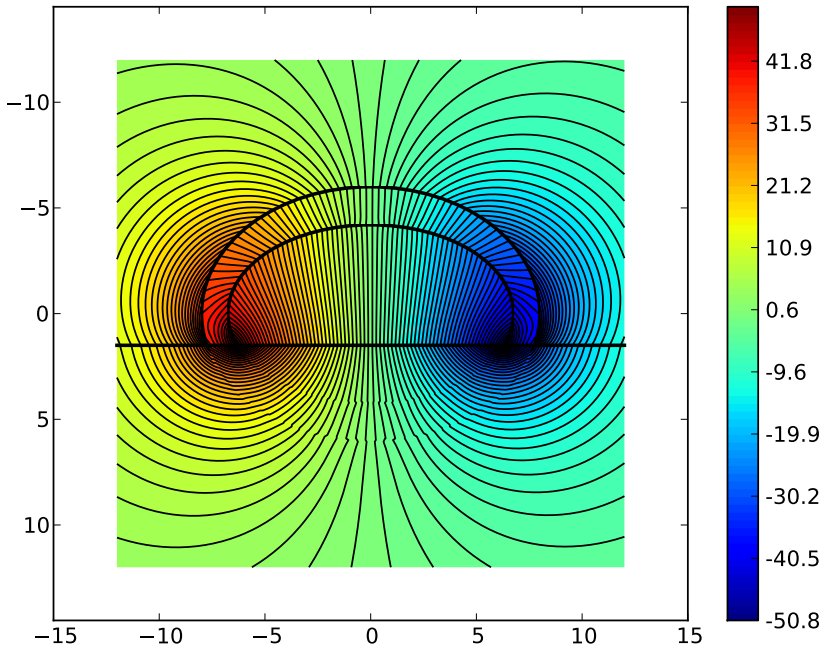

Figure 5.7.: The equipotential lines of $\mathrm{Im}[\psi]$ at photon energy $E = 2.296\,\mathrm{eV}$, which is the position of the peak values of $\mathrm{Im}\left[\alpha_{\parallel}\right]$ and $\mathrm{Im}[\alpha_{\parallel}^{10}]$.

5.2.5. Errors as a function of photon energy

As seen when comparing Figs. 5.15 and 5.16, the magnitude of the errors in the boundary conditions appears to vary greatly depending on which photon energy the calculation is done at. How the errors depend on energy across the entire spectrum is shown in Fig. 5.17. As seen it is verified that the magnitudes of the errors depend greatly on the photon energy, and they appear to peak at values where the polarizabilities were also found to peak.

5.2.6. The spherical limit

It is useful to verify that the simulation implemented here agrees with the results from the code for the spherical special case, in the case when the spheroids are made to approach the spherical limit. The test case used here is a 6 nm spherical Ag island, truncated and supported by an Al_2O_3 substrate. The amount of truncation is $t_r^{(1)} = 0.5$. The SDRS curve for this case is simulated using the code for the spherical special case. This island is then flattened and made gradually more spheroidal, while keeping the silver coverage (3.121) constant. The SDRS curves for these cases are simulated using the new code for the spheroidal case, and compared with the spherical case as implemented

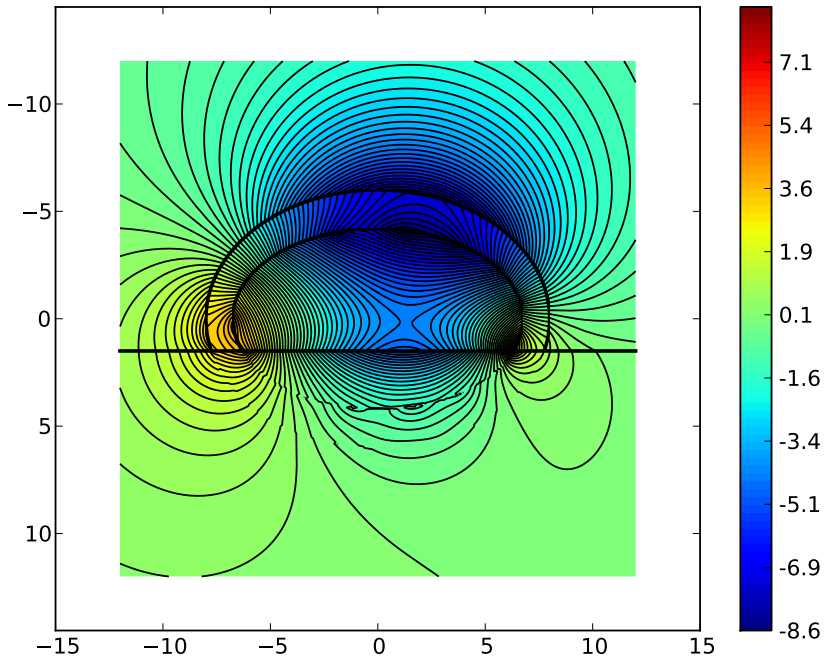

Figure 5.8.: The equipotential lines of $\mathrm{Im}[\psi]$ at photon energy $E = 2.775\,\mathrm{eV}$, which is the position of the peak values of $\mathrm{Im}\,[\alpha_z]$ and $\mathrm{Im}[\alpha_z^{10}]$.

in GranFilm 2.0. The results from these tests can be seen in Figs. 5.18a (no coating) and 5.18b (with oxide coating). The calculations were done to a multipole order $M = 16$. Using a high multipole order while going too far into the spherical limit was found to cause numerical problems, but before this happens an agreement with the purely spherical simulation is apparent. Neither finite-size corrections nor corrections for island-island interactions are used in this test, as it is done to test the spherical limit of the algorithm, not to compare with experimental data.

As seen in Fig. 5.18, the SDRS curve from the spheroidal simulations meet up nicely with the curve from the spherical simulation in the $R_\perp \to R_\parallel$ limit. Note that if one were to include finite-size corrections to the dielectric function of Ag, the increase in peak SDRS signal while flattening the island will not be so great. This is so because the electron mean free path is calculated based on $R_\perp$ (see Sec. 2.3), and as demonstrated in Fig. 2.2b, one of the effects of introducing finite-size corrections to silver is to decrease the magnitude of the SDRS signal.

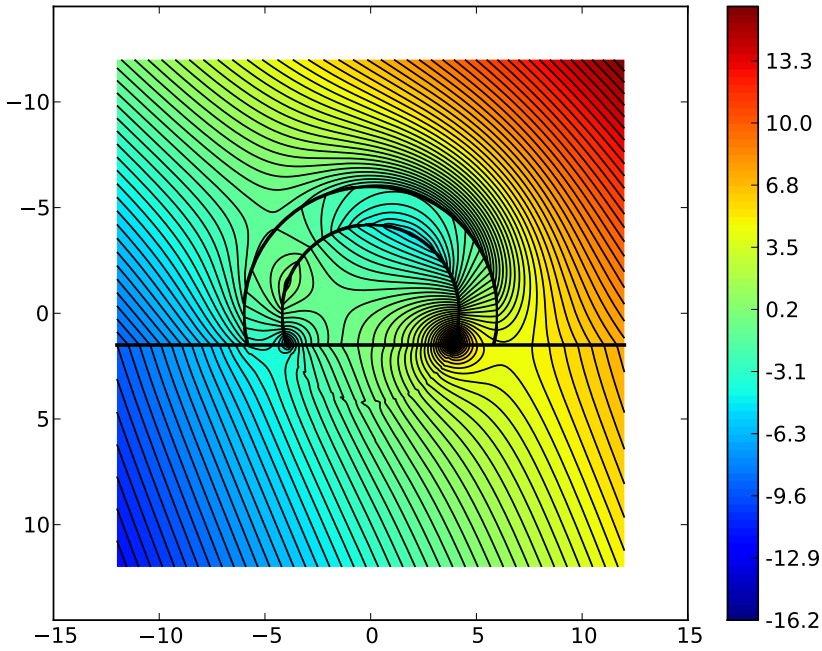

Figure 5.9.: The equipotential lines of Re[ψ] from a spherical version of the test case. The calculation is made at photon energy $E = 2.33\,\mathrm{eV}$, close to the main peak of the SDRS curve for this case.

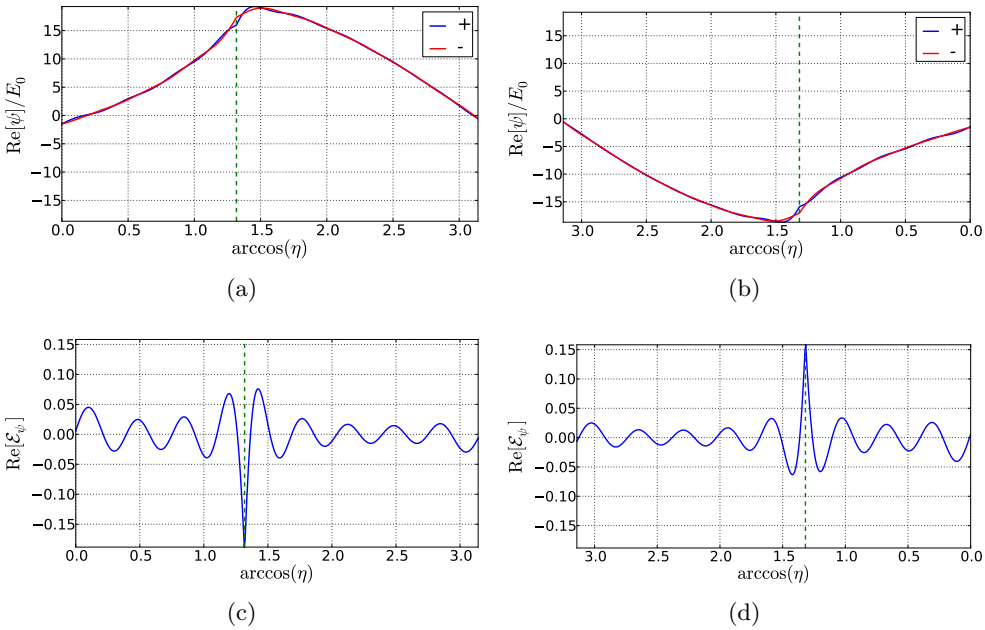

Figure 5.10.: Plots of the real part of ψ just outside (+) and inside (-) the outer spheroidal interface ($s = 1$), on both the a) $\phi = 0$ half and the b) $\phi = \pi$ half of the $y = 0$ plane. Also shown is the real part of the error measure $\mathcal{E}_\psi$ at the corresponding points. The dashed vertical lines show the point of truncation for this interface. The calculations are done at $E = 2.225\,\mathrm{eV}$.

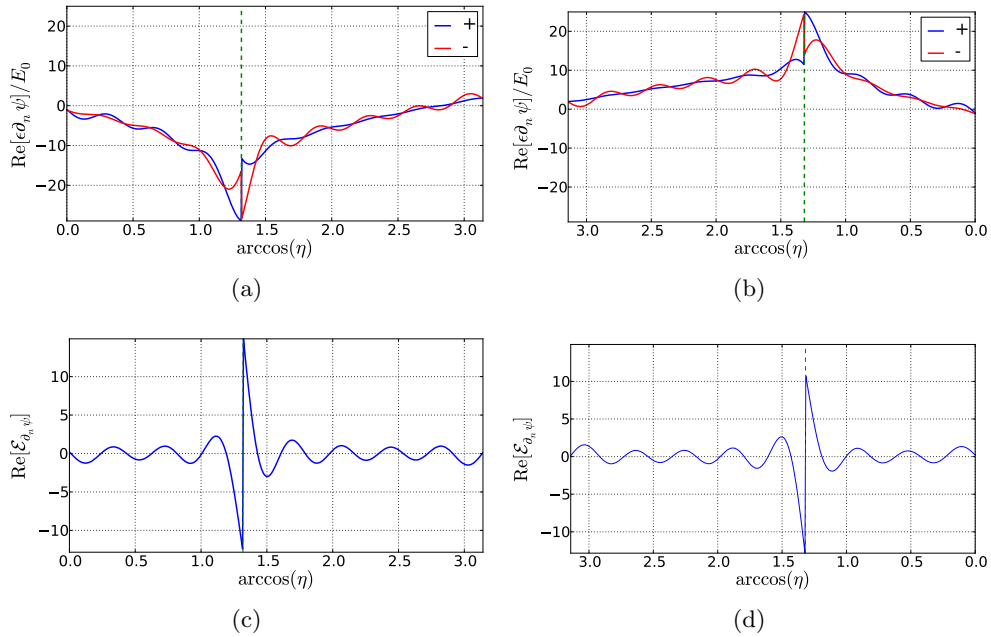

Figure 5.11.: Plots of the real part of $\epsilon\partial_n\psi$ just outside (+) and inside (-) the outer spheroidal interface ($s = 1$), on both the a) $\phi = 0$ half and the b) $\phi = \pi$ half of the $y = 0$ plane. Also shown is the real part of the error measure $\mathcal{E}_{\partial_n\psi}$ at the corresponding points. The dashed vertical lines show the point of truncation for this interface. The calculations are done at $E = 2.225\,\mathrm{eV}$.

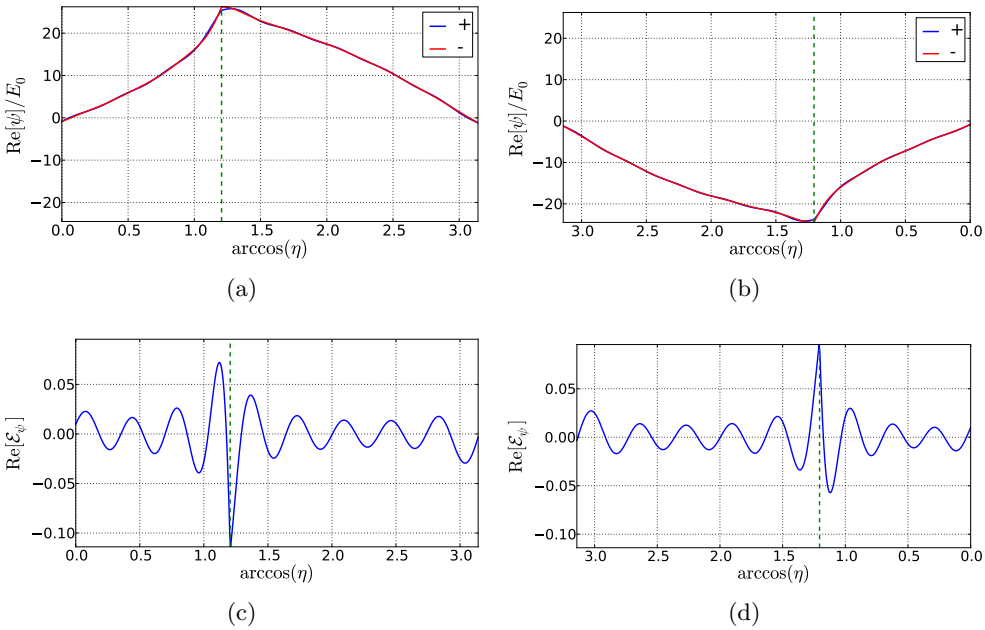

Figure 5.12.: Plots of the real part of ψ just outside (+) and inside (-) the inner spheroidal interface ($s = 2$), on both the a) $\phi = 0$ half and the b) $\phi = \pi$ half of the $y = 0$ plane. Also shown is the real part of the error measure $\mathcal{E}_\psi$ at the corresponding points. The dashed vertical lines show the point of truncation for this interface. The calculations are done at $E = 2.225\,\mathrm{eV}$.

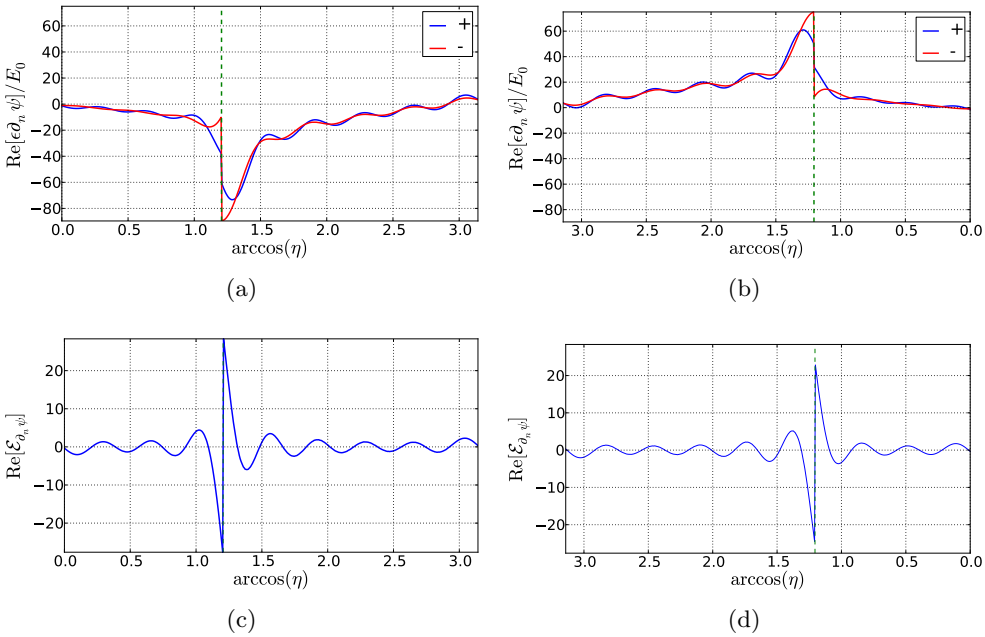

Figure 5.13.: Plots of the real part of $\epsilon\partial_n\psi$ just outside (+) and inside (-) the inner spheroidal interface ($s = 2$), on both the a) $\phi = 0$ half and the b) $\phi = \pi$ half of the $y = 0$ plane. Also shown is the real part of the error measure $\mathcal{E}_{\partial_n\psi}$ at the corresponding points. The dashed vertical lines show the point of truncation for this interface. The calculations are done at $E = 2.225\,\mathrm{eV}$.

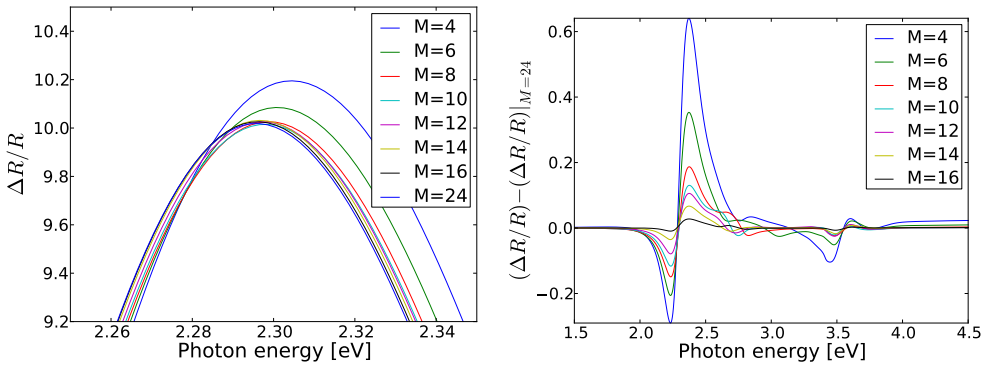

(a) (b)

Figure 5.14.: Convergence test of the SDRS curve calculated for the test case with increasing multipole order M. a) Close up view of the SDRS curves at the main 2.3 eV resonance, where the error is found to be the largest. b) Difference between the SDRS curve calculated for the indicated multipole order M and the "correct" curve gotten from a calculation at $M = 24$.

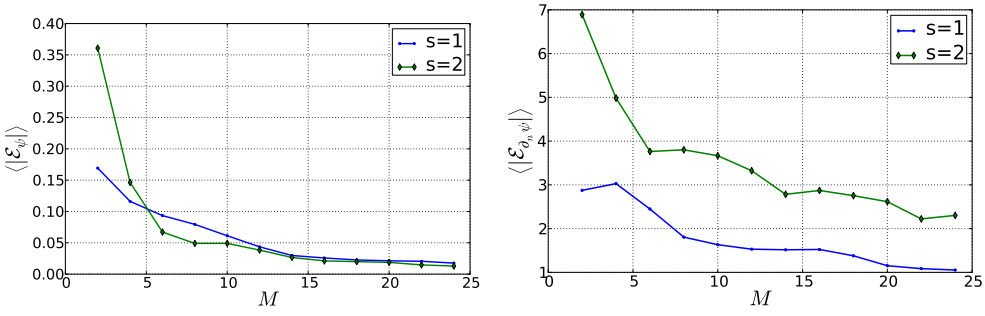

(a) (b)

Figure 5.15.: Convergence of the average absolute errors in boundary conditions for both spheroidal interfaces in the test case, at E=2.225 eV. The average absolute value of errors in the boundary conditions a) (3.29a) and b) (3.29b) are plotted against multipole order M.

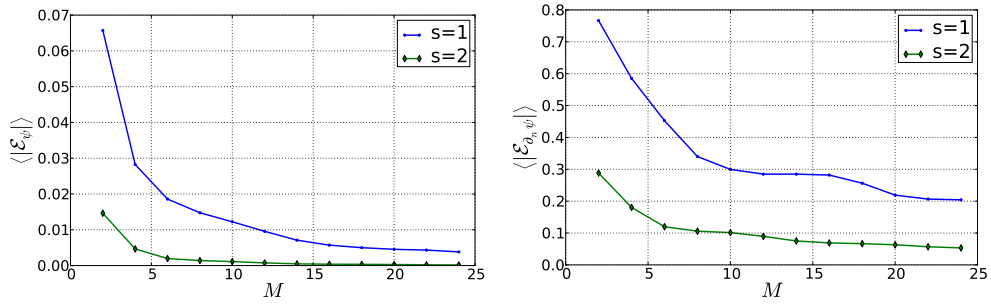

(a) (b)

Figure 5.16.: Convergence of the average absolute errors in boundary conditions for both spheroidal interfaces in the test case, at E=4.5 eV. The average absolute value of errors in the boundary conditions a) (3.29a) and b) (3.29b) are plotted against multipole order M.

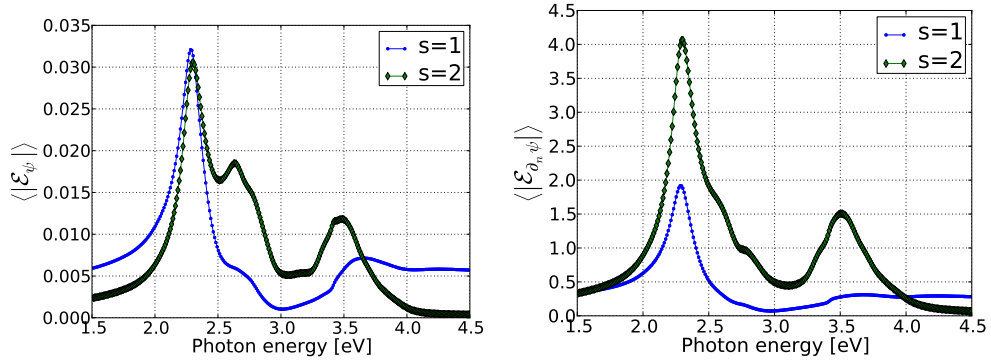

(a) (b)

Figure 5.17.: The average absolute errors in the boundary conditions a) (3.29a) and b) (3.29b) for both spheroidal interfaces in the test case, plotted against photon energy. Calculations are done with a multipole order $M = 16$.

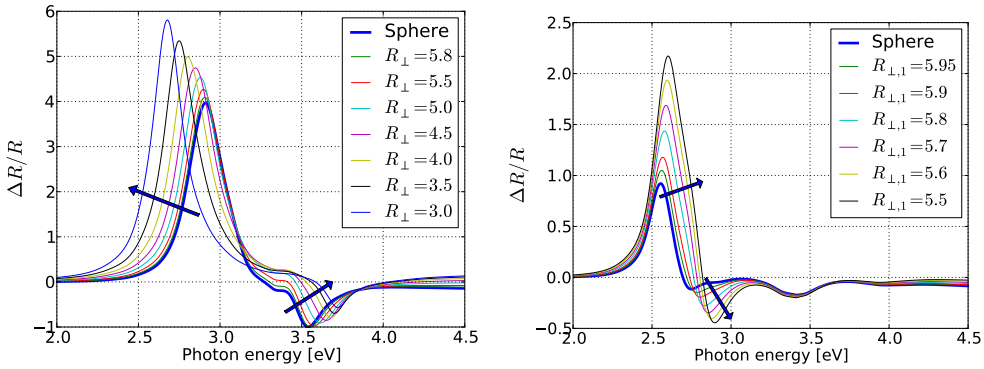

(a) (b)

Figure 5.18.: Comparison of the SDRS curve from a spherical simulation ($R = 6\,\mathrm{nm}$) with curves from spheroidal simulations, while $R_\parallel$ is kept constant. The arrows show the trend with increasing eccentricity. a) Ag island with no coating. b) Ag island with Ag_2O coating.

6. Oxidation of silver nanoparticles

It is not enough for the equations to be numerically well behaved though, they should also be able to at least qualitatively reproduce some experimental data. Some preliminary experiments have been performed by Rémi Lazzari from the Paris Institute of Nanosciences, where a 0.5 nm equivalent thickness deposit of Ag nanoparticles on an Al_2O_3 substrate was exposed to O_2. This could be expected to oxidize the outer layers of the silver particles, creating Ag_2O coated Ag islands, which could be a useful testing ground for the algorithm for coated islands derived and implemented here.

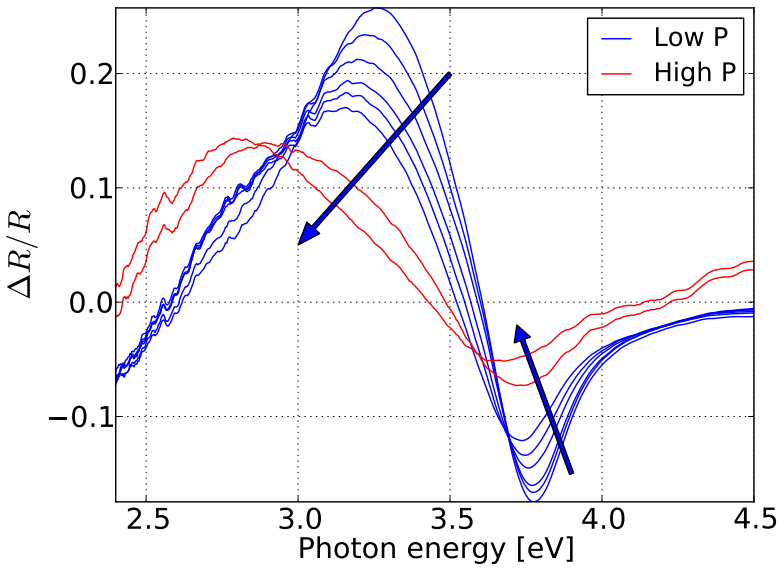

Figure 6.1.: Experimental SDRS data from the O_2 exposure of Ag nanoparticles supported on a Al_2O_3 substrate. As indicated, the O_2 pressure was increased at one point during the experiment. The arrows show the trend for increasing time of exposure.

The O_2 exposure was done in two stages: First at a low O_2 pressure, and then at a higher ($P > 10$ mbar) pressure. During exposure SDRS spectra were measured using p-polarized light at $\theta = 45°$, and this data is presented in Fig. 6.1. Unfortunately the data on the time and pressure corresponding to each curve is not very precise since this is a preliminary experiment, but at

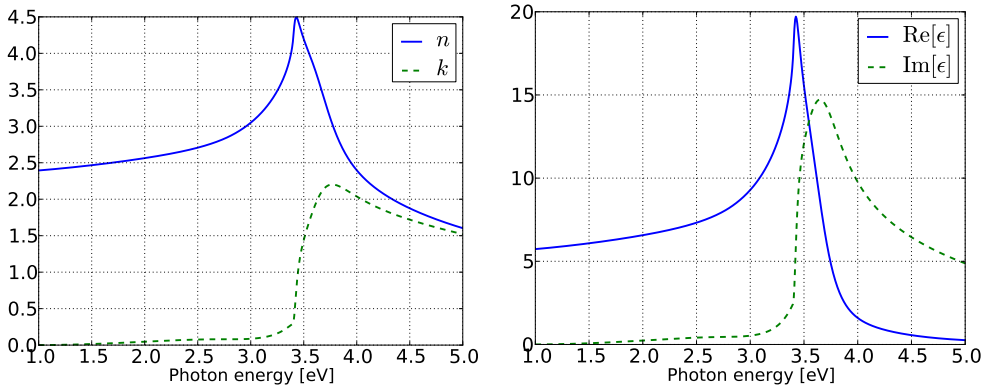

(a) (b)

Figure 6.2.: Data reconstructed from equations and fitted parameters in [29]. a) Refractive index and extinctive coefficient of Ag_2O. b) Real and imaginary part of the dielectric function of Ag_2O.

least a qualitative trend is apparent.

The purpose of this section is to investigate whether the equations implemented here can reproduce the trend displayed in Fig. 6.1. Firstly, the issue of the complex dielectric function of the Ag_2O coating will be covered in Sec. 6.1. Then Sec. 6.2 will go through how the fraction of Ag oxidated relates to the input parameters of the algorithm, mainly the parallel and perpendicular radii of the two spheroidal interfaces. Finally Sec. 6.3 will present the resulting SDRS trends from a simulated oxidation process.

6.1. The complex dielectric function of Ag_2O

While all other materials needed here have their complex dielectric functions in the database included in GranFilm, this is not the case for Ag_2O. The values are obviously needed for a realistic simulation, so data from the work of Gao et al. [29] is used here. This is a triple Tauc-Lorentz model with parameters fitted to spectroscopic ellipsometry measurements. The film was created by magnetron sputtering, which is not the case for the process simulated here, but it should be close enough to find a qualitative trend. The functions reconstructed from the equations and parameters in [29] can be seen in Fig. 6.2.

	M	ρ
Ag	$0.1079\,\mathrm{kg\,mol^{-1}}$	$10\,500\,\mathrm{kg/m^3}$
Ag_2O	$0.2317\,\mathrm{kg\,mol^{-1}}$	$7100\,\mathrm{kg/m^3}$

Table 6.1.: The molecular/atomic weights and densities of silver and silver oxide [30].

6.2. Relating the fraction oxidized to geometry parameters

When simulating the oxidation process of the silver nanoparticles, one can not simply add a growing layer of Ag_2O on the outside and keep the Ag core constant. When creating the oxide, metallic silver will be consumed, while at the same time new matter is added to the islands in the form of oxygen atoms. Exactly how the volume of oxide and silver evolves will depend on the density and atomic weights of both materials, as well as the stoichiometry of the oxide.

Let us first define a parameter f_{ox}, which is the fraction of silver which has been oxidized at a given time. Also, let ρ_{Ag} and $\rho_{\mathrm{Ag_2O}}$ denote the densities of Ag and Ag_2O respectively. Similarly let M_{Ag} and $M_{\mathrm{Ag_2O}}$ denote their atomic/molecular weights. The values of ρ and M for these two materials may be found in Tab. 6.1. Let V_i be the initial volume of the Ag island, such that the volume of the remaining Ag core at a given time is $(1 - f_{\mathrm{ox}})V_i$.

The issue now is to figure out what the parameters of the two spheroidal interfaces in the model must be for a given value of f_{ox}. First of all one might calculate how much volume of oxide is created compared to the volume of silver lost to the oxidation process. This process is outlined in the following equations:

$$
\begin{aligned}
\text{Moles of Ag oxidized} &= \frac{\rho_{\mathrm{Ag}} \cdot V_i \cdot f_{\mathrm{ox}}}{M_{\mathrm{Ag}}} \\
\text{Moles of } Ag_2O \text{ created} &= \frac{\rho_{\mathrm{Ag}} \cdot V_i \cdot f_{\mathrm{ox}}}{2 \cdot M_{\mathrm{Ag}}} \\
\text{Volume of } Ag_2O \text{ created} &= \frac{M_{\mathrm{Ag_2O}} \cdot \rho_{\mathrm{Ag}} \cdot V_i \cdot f_{\mathrm{ox}}}{2 \cdot \rho_{\mathrm{Ag_2O}} \cdot M_{\mathrm{Ag}}} \\
\text{Volume of Ag lost} &= V_i \cdot f_{\mathrm{ox}} \\
\frac{\text{Volume of } Ag_2O \text{ created}}{\text{Volume of Ag lost}} &= \frac{M_{\mathrm{Ag_2O}} \cdot \rho_{\mathrm{Ag}}}{2 \cdot M_{\mathrm{Ag}} \cdot \rho_{\mathrm{Ag_2O}}} \approx 1.59
\end{aligned}
\tag{6.1}
$$

To get from this ratio of volumes to an appropriate set of parameters, one must make some assumptions. Here is is assumed that both the Ag-Ag_2O

and the Ag_2O-Air interfaces stay spheroidal, centered in the origin and with the same focal radius a during the entire oxidation process. Now, since the volumes of both the Ag core and the Ag_2O coating are known, the values of $R_{\perp,1}$ and $R_{\perp,2}$ may be found. This is done by using Eq. (3.115) for the volume contained inside spheroidal interface s.[1] Given a certain volume, and the above assumptions, Eq. (3.115) may be solved for a corresponding ξ_0 using an iterative root finding method. The values of $R_\perp$ may easily be found from values of ξ_0, and through the assumption of a known and constant value of a, $R_{\parallel,1}$ and $R_{\parallel,2}$ may be found. The truncation ratios $t_r^{(1)}$ and $t_r^{(2)}$ are found through the assumptions of a constant center of the spheroids compared to the substrate, *i.e.* a constant d.

To do these calculations it is necessary to have some parameters for the initial islands of pure Ag. As mentioned, it is known from the experiment that the deposited amount of Ag corresponds to an equivalent thickness of $t_{\text{eq}} = 0.5\,\text{nm}$. Using a contact angle for silver on alumina of $125° - 130°$ [22] gives an initial truncation ratio of approximately $t_r = 0.6$. Assuming hexagonal packing and a lattice constant of $L = 10\,\text{nm}$, the given equivalent thickness demands that $R_\perp R_\parallel^2 \approx 11.5\,\text{nm}^3$. A somewhat arbitrary choice which satisfies this is $R_\perp = 2.0$ and $R_\parallel = 2.4$, which will be used in this attempt to qualitatively reproduce the experiment.

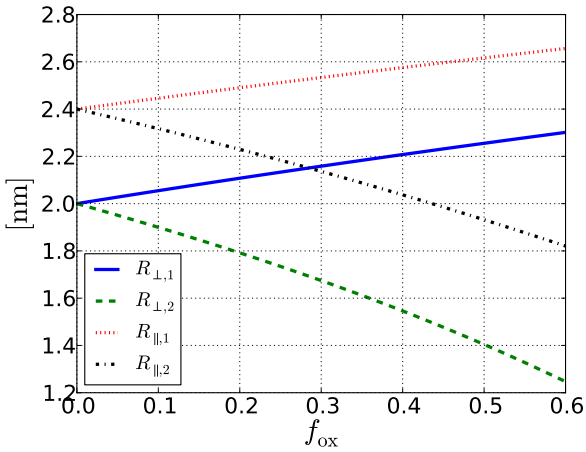

Figure 6.3.: The perpendicular and parallel radii of the two spheroidal interfaces in the simulated oxidation process as calculated in Sec. 6.2, plotted against the fraction of silver oxidized.

Given all the above assumptions and calculations, the radii of the spheroidal interfaces may be found as a function of fraction oxidized, as displayed in

[1] In this case, $V_{\text{Ag}} = V_2$ and $V_{\text{Ag}_2\text{O}} = V_1 - V_2$.

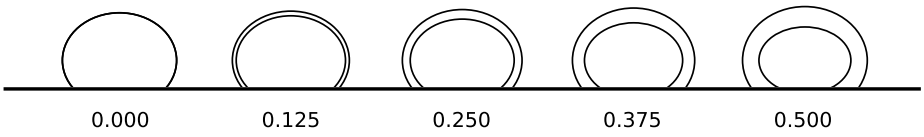

Figure 6.4.: Cross sections of the islands at certain points during the simulated oxidation process, as calculated in Sec. 6.2. The numbers below the islands show the corresponding values of f_{ox}, the fraction of the original Ag which has been oxidized.

Fig. 6.3. The same oxidation process is also illustrated as cross sections of islands in Fig. 6.4, to give a better impression of how the geometry evolves under these assumptions.

6.3. Simulation of the oxidation process

Given the values for the dielectric function of Ag_2O presented in Sec. 6.1, and the calculations and assumptions in Sec. 6.2, it is possible to use the newly extended GranFilm software to simulate the evolution of the SDRS response during the oxidation process. The results from calculations done at a multipole order of $M = 20$ may be seen in Fig. 6.5. Finite-size corrections (Sec. 2.3) were used for the dielectric function of the Ag core, using the parameters listed in the caption of Fig. 2.2. Island-island interactions were corrected for to dipolar order (Sec. 3.5.1), and first order surface susceptibilities were used to calculate the differential reflectance. The degree of agreement with the experimental data will be discussed in Sec. 7.

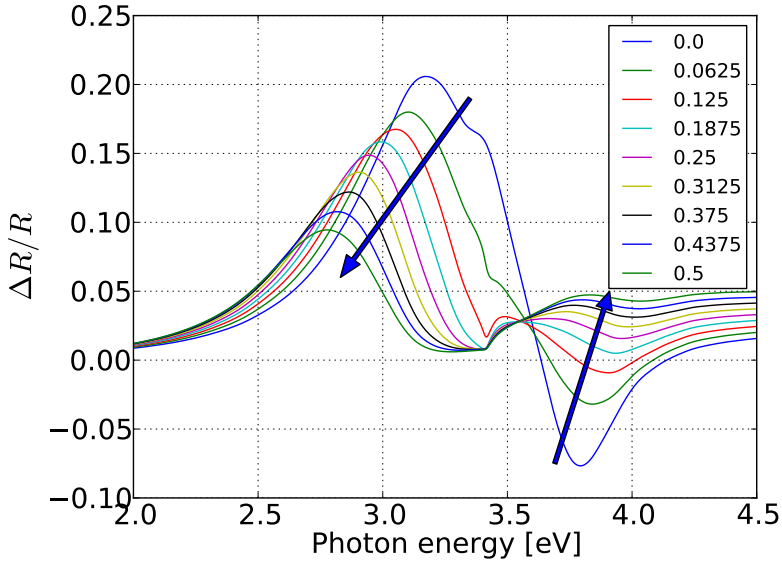

Figure 6.5.: SDRS curves from the simulated oxidation of truncated Ag nanoparticles supported on an Al_2O_3 substrate. The inset shows the values of f_{ox} for a given curve, and the arrows point in the direction of increasing time, *i.e.* increasing f_{ox}.

7. Discussion

Since the main goals of this thesis are the analytical derivation and numerical implementation of the equations in Sec. 3, one of the most important questions to discuss is whether this has been completed without error. As shown in Sec. 4, the analytical results agree with the work of others when reduced to two important special cases. While this is not proof of correctness, it is certainly a good sign.

Analytical correctness does not guarantee that the numerical implementation in GranFilm is without error though. The code was checked for errors thoroughly, and subjected to numerical tests presented in 5.2. Firstly one may note that the SDRS curve (Fig. 5.1) and polarizabilities (Figs. 5.2 and 5.3) look reasonable compared to what one might find in the literature [19]. Also, the cross section plots of the real part of the potential in Figs. 5.4 – 5.8 look like what one would expect from a polarization response in such a particle, with a reasonably continuous $\mathrm{Re}[\psi]$.

Looking reasonable is not a very rigorous test however. A proper test should look more closely at exactly how closely the two boundary conditions in Eq. (3.29) are satisfied. In fact, if they are completely satisfied, the calculated potential is the one and only correct one (*cf.* the uniqueness theorem). Exactly how closely they are satisfied in the test case, and how the errors vary along the spheroidal interfaces, is examined in Sec. 5.2.3. Figures 5.10 – 5.13 show the errors in both boundary conditions along both spheroidal interfaces of the test case in the $y = 0$ plane. Some things may be noted about these results. First of all, the values of ψ appear to be more continuous across the interfaces than $\epsilon\partial_n\psi$. In other words the first condition (3.29a) appears qualitatively to be better satisfied than the second condition (3.29b). Besides this, the errors have some common behavior: They oscillate along the interface, and they have a peak value at the point of truncation, *i.e.* where the spheroidal interfaces meet the substrate surface. As seen in Figs. 5.4, 5.10 and 5.12, these are also approximately the points where the potential has the largest value at the main resonance. With a finite multipole order it is reasonable to expect the errors to be largest where the response is the most dramatic.

Another test of correctness is shown in Sec. 5.2.6 (Fig. 5.18), where it is verified that the SDRS results from the new code for the spheroidal case appears to agree with the results from the existing code for the spherical case. However, it was found that one cannot push the new spheroidal code too far

into the spherical limit, as the limit $\xi \to \infty,\ a \to 0$ is not that well behaved numerically. Still, the test verifies the expected agreement when reasonably far into the limit.

Since the calculations are expected to yield the correct potential as $M \to \infty$, convergence towards this as M increases is tested in Sec. 5.2.4. As shown in Fig. 5.14, the simulated far field SDRS response converges towards a single curve quite quickly. At $M = 10$, the curve appears to have converged well within the accuracy needed to compare with experimental data (Fig. 5.14a), though the errors are not completely gone, as seen in Fig. 5.14b. A convergence test checking the potential itself, and not only its far field effects, is presented in Figs. 5.15 and 5.16. It is seen that the average absolute errors in both boundary conditions decrease every time the multipole order M is increased. Note that most of the errors apparently do not disappear until around $M = 20$, which is much higher than what appeared to be needed for convergence of the SDRS curve. This means that while there are still quite a lot of errors in the boundary conditions at $M = 10$, the dipolar ($\ell = 1$) expansion coefficients are quite correct already. Increasing M beyond 10 has the effect of adjusting the higher order coefficients to make the potential more correct, while only slightly modifying the dipolar coefficients.

It may be tempting to increase M to the thirties or even forties to ensure that everything is correct. Besides making the calculations take an unnecessary amount of time, this may also introduce round-off errors when calculating the needed integrals. This is a purely numerical effect, caused by the way a computer does arithmetics. The consequence is that while one analytically expects the results to become better and better indefinitely as M is increased, in practice one or both of the average errors are seen to increase abruptly as M reaches a value in the area of 30. Exactly at which value of M this happens at depends on the test case.

Convergence is observed at both a resonance energy (Fig. 5.15) and an energy where nothing special happens (Fig. 5.16). Note however that the magnitude of the errors may differ by as much as an order of magnitude between the two energies. In fact, by comparing Fig. 5.17 with Figs. 5.2 – 5.3, the errors have a tendency to peak at the same energies as where the polarizabilities peak. This is not surprising, as more accurately representing the dramatic potential response at a resonance energy is expected to require a higher multipole order M.

Now that it as been verified that both the analytical derivations and the numerical implementation seem correct and well behaved, what might be said about the potential plots resulting from the test case? One apparent issue is that the potential plots appear to be dominated by a dipolar response. With a spherical case (Fig. 5.9), a clearly quadrupolar response can be found close to the main resonance. No such quadrupolar potential can be found in the

real part of the potential close to the main resonance in the spheroidal case. It might appear that the elongated shape promotes dipolar responses, and suppresses most of the quadrupolar responses. In fact, it is observed that the quadrupolar response in Fig. 5.9 gradually changes into a more pure dipolar response as the island eccentricity is increased.

The final goal of this work was to use the newly implemented code in an attempt to reproduce some experimental data. These efforts are detailed in Sec. 6. Comparing the experimental data in Fig. 6.1 to the simulation in Fig. 6.5, it is clear that at least the major features could be reproduced: As the oxidation proceeds, the magnitude of the SDRS signal decreases while the main peak moves to lower energies. However, in the low pressure phase of the experimental data, the shift to lower energies is not as fast compared to the decrease in magnitude. The simulation appears to be slightly more consistent with the high pressure data in this respect. Another discrepancy is the fact that the valley at approximately 3.7 eV moves in opposite directions: In the experimental data it moves to lower energies, while in the simulation results it moves to higher energies. These discrepancies may exist because the real oxidation process does not necessarily happen according to the assumptions in Sec. 6.2 used to calculate the geometry at a given fraction oxidized. There is not really any reason why the focal radius a should stay constant, but some assumptions have to be made at this stage to arrive at a result.

Note also from Fig. 6.5 that as the oxidation proceeds a small feature appears at approximately 3.4 eV which can not be seen in the experimental data (Fig. 6.1). The location of this feature is where the dielectric function of Ag_2O used in the simulation (Fig. 6.2) has a sudden increase in magnitude. The fact that this feature is absent in the experimental data may be an indication that the dielectric function used may not be appropriate for the oxide layer expected in the experiment.

Discrepancies may also arise because of distributions in parameters which in the simulation are assumed to be constant across the island film. The islands are probably not arranged in a perfect hexagonal array, they may not all be of the same size, and they may not all be truncated to the same degree. These distributions in parameters are expected to give a *broadening effect* however [22], and may not explain the valley of the SDRS curve moving in the wrong direction along the energy scale.

8. Conclusion

The first main part of this work was to derive the integrals and sets of equations needed to solve Laplace's equation for a system containing spheroidal islands/nanoparticles with an arbitrary number of coatings, truncated and supported on a substrate surface. Solving Laplace's equation for a quasi static case enables the calculation of the optical properties of a film consisting of many such islands, including the SDRS curve.

This first part was apparently completed successfully, resulting in the systems of equations needed to calculate the multipole coefficients, which could be used to calculate either the quasi-static potential or the optical properties of an island film. To ensure their correctness, the derivations were thoroughly checked for errors, as well as compared with special cases calculated by others. In order to be useful, the new equations had to be integrated into the existing framework of the GranFilm software, a process which was the second main part of this work. Numerical tests verified the probable correctness of this, as the errors in boundary conditions appeared low, and converged as expected when the multipole order of the calculation was increased.

The third main part was to use the new algorithm to reproduce experimental SDRS data from the oxidation of a film of silver islands. While the main features of the SDRS curve's evolution could be reproduced, there were some discrepancies. This may be explained by the fact that much is unknown about the oxidation process, and thus it is hard to make correct assumptions about the evolution of the geometry in the simulation. Also, the experiment used for comparison was quite preliminary, and some parameters were unknown or not under strict control.

Future improvements to the derived equations could attempt to relax some of the assumptions made, such as requiring all spheroidal interfaces of an island to have the same focal radius. This was an assumption which simplified the calculations, but did not really have any physical justification. Future attempts to reproduce experimental data from a silver oxidation process could attempt to use different sets of assumptions regarding the evolution of the geometry, as there was only time to try one in this work. This may uncover the reasons for the discrepancies, as well as possibly enabling a more quantitative analysis of the data. One could also try to obtain new and better data on the dielectric function of the silver oxide film, as the data used here was obtained from a magnetron sputtered film, which might not have been appropriate in this case.

Bibliography

[1] E. Aursand, "Inversion of a nanoplasmonics model for the quantitative analysis of nanoparticle growth." Pre-master's project, Trondheim, 2011.

[2] A. N. Shipway, E. Katz, and I. Willner, "Nanoparticle arrays on surfaces for electronic, optical, and sensor applications," *ChemPhysChem*, vol. 1, no. 1, pp. 18–52, 2000.

[3] C. Bréchignac, P. Houdy, and M. Lahmani, *Nanomaterials and Nanochemistry*. Berlin, Heidelberg: Springer, 2007.

[4] I. Matsui, "Nanoparticles for electronic device applications: A brief review," *Journal of Chemical Engineering of Japan*, vol. 38, no. 8, pp. 535–546, 2005.

[5] O. Salata, "Applications of nanoparticles in biology and medicine," *Journal of Nanobiotechnology*, vol. 2, no. 1, p. 3, 2004.

[6] M. De, P. S. Ghosh, and V. M. Rotello, "Applications of nanoparticles in biology," *Advanced Materials*, vol. 20, no. 22, pp. 4225–4241, 2008.

[7] M. Ahamed, M. S. AlSalhi, and M. Siddiqui, "Silver nanoparticle applications and human health," *Clinica Chimica Acta*, vol. 411, no. 23-24, pp. 1841 – 1848, 2010.

[8] A. M. Schrand, L. K. Braydich-Stolle, J. J. Schlager, L. Dai, and S. M. Hussain, "Can silver nanoparticles be useful as potential biological labels?," *Nanotechnology*, vol. 19, no. 23, p. 235104, 2008.

[9] L. N. Lewis, "Chemical catalysis by colloids and clusters," *Chemical Reviews*, vol. 93, no. 8, pp. 2693–2730, 1993.

[10] P. Chiaradia and R. D. Sole, "Differential-Reflectance Spectroscopy and Reflectance-Anisotropy Spectroscopy on Semiconductor Surfaces," *Surface Review and Letters*, vol. 6, pp. 517–528, 1999.

[11] Y. Borensztein, "Linear Optical Spectroscopies for Surface Studies," *Surface Review and Letters*, vol. 7, pp. 399–410, 2000.

[12] D. D. Brandon and W. D. Kaplan, *Microstructural characterization of materials*. Hoboken, N.J.: Wiley, 2. ed. ed., 2008.

[13] M. I. Stockman, "Nanoplasmonics: The physics behind the applications," *Physics Today*, vol. 64, no. 2, p. 020000, 2011.

[14] J. C. Maxwell Garnett, "Colours in Metal Glasses and in Metallic Films.," *Royal Society of London Proceedings Series I*, vol. 73, pp. 443–445, 1904.

[15] T. Yamaguchi, S. Yoshida, and A. Kinbara, "Anomalous optical absorption of aggregated silver films," *Thin Solid Films*, vol. 18, no. 1, pp. 63 – 70, 1973.

[16] T. Yamaguchi, S. Yoshida, and A. Kinbara, "Optical effect of the substrate on the anomalous absorption of aggregated silver films," *Thin Solid Films*, vol. 21, no. 1, pp. 173 – 187, 1974.

[17] D. Bedeaux and J. Vlieger, *Optical Properties of Surfaces*. London: Imperial College Press, 2002.

[18] F. L. Pedrotti, L. M. Pedrotti, and L. S. Pedrotti, *Introduction to Optics*. New Jersey: Prentice-Hall, 3rd ed., 2007.

[19] R. Lazzari and I. Simonsen, "GranFilm: a software for calculating thin-layer dielectric properties and Fresnel coefficients," *Thin Solid Films*, vol. 419, no. 1-2, pp. 124 – 136, 2002.

[20] J. D. Jackson, *Classical Electrodynamics*. New York: Wiley & Sons, 1975.

[21] M. Haarmans and D. Bedeaux, "The polarizability and the optical properties of lattices and random distributions of small metal spheres on a substrate," *Thin Solid Films*, vol. 224, no. 1, pp. 117 – 131, 1993.

[22] R. Lazzari and J. Jupille, "Quantitative analysis of nanoparticle growth through plasmonics," *Nanotechnology*, vol. 22, no. 44, p. 445703, 2011.

[23] M. Wind, P. Bobbert, J. Vlieger, and D. Bedeaux, "The polarizability of a truncated sphere on a substrate ii," *Physica A: Statistical Mechanics and its Applications*, vol. 143, no. 1-2, pp. 164 – 182, 1987.

[24] A. Liebsch, "Surface-plasmon dispersion and size dependence of mie resonance: Silver versus simple metals," *Phys. Rev. B*, vol. 48, pp. 11317–11328, Oct 1993.

[25] S. Norrman, T. Andersson, C. G. Granqvist, and O. Hunderi, "Optical properties of discontinuous gold films," *Phys. Rev. B*, vol. 18, pp. 674–695, Jul 1978.

[26] K. Rottmann, *Matematische Formelsammlung*. Spektrum, 2003.

[27] D. J. Griffiths, *Introduction to Electrodynamics*. San Francisco: Pearson, 3rd ed., 2008.

[28] I. Simonsen, R. Lazzari, J. Jupille, and S. Roux, "Numerical modeling of the optical response of supported metallic particles," *Phys. Rev. B*, vol. 61, pp. 7722–7733, Mar 2000.

[29] X.-Y. Gao, H.-L. Feng, J.-M. Ma, Z.-Y. Zhang, J.-X. Lu, Y.-S. Chen, S.-E. Yang, and J.-H. Gu, "Analysis of the dielectric constants of the Ag2O film by spectroscopic ellipsometry and single-oscillator model," *Physica B: Condensed Matter*, vol. 405, no. 7, pp. 1922 – 1926, 2010.

[30] G. Aylward and T. Findlay, *SI Chemical Data*. Wiley, 5th ed., 2002.

A. Normalization used in the code

The GranFilm code does not implement the equations derived in Sec. 3 exactly, but rather in slightly modified dimensionless forms. For completeness, and for assistance while reading the code, these alternate forms are detailed in this section.

First of all, note that the expansion coefficient $A_{\ell m}$ has units of $\mathrm{V\,m}^{\ell+1}$, while $B_{\ell m}$ has units of $\mathrm{V\,m}^{-\ell}$. The numerical implementation instead solves for dimensionless expansion coefficients, defined by:

$$\begin{aligned}\widehat{A}^{(i)}_{\ell m} &\equiv \frac{R_{\perp,1}^{-\ell-2}}{E_0} A^{(i)}_{\ell m} \\ \widehat{B}^{(i)}_{\ell m} &\equiv \frac{R_{\perp,1}^{\ell-1}}{E_0} B^{(i)}_{\ell m}.\end{aligned} \tag{A.1}$$

It also calculates dimensionless polarizabilities, defined by:

$$\begin{aligned}\widehat{\alpha}_z &\equiv \frac{2\pi\epsilon_1}{\sqrt{\pi/3}\cos\theta_0}\widehat{A}^{(1)}_{10} = R_{\perp,1}^{-3}\alpha_z \\ \widehat{\alpha}_\parallel &\equiv -\frac{4\pi\epsilon_1}{\sqrt{2\pi/3}\sin\theta_0\exp(-i\phi_0)}\widehat{A}^{(1)}_{11} = R_{\perp,1}^{-3}\alpha_\parallel \\ \widehat{\alpha}^{10}_z &\equiv \frac{\pi\epsilon_1}{\sqrt{\pi/5}\cos\theta_0}\widehat{A}^{(1)}_{20} = R_{\perp,1}^{-4}\alpha^{10}_z \\ \widehat{\alpha}^{10}_\parallel &\equiv -\frac{4\pi\epsilon_1}{\sqrt{6\pi/5}\sin\theta_0\exp(-i\phi_0)}\widehat{A}^{(1)}_{21} = R_{\perp,1}^{-4}\alpha^{10}_\parallel,\end{aligned} \tag{A.2}$$

and dimensionless surface susceptibilities, defined by:

$$\begin{aligned}\widehat{\gamma} &\equiv \widehat{\rho}\widehat{\alpha}_\parallel = R_{\perp,1}^{-1}\gamma \\ \widehat{\beta} &\equiv \widehat{\rho}\widehat{\alpha}_z/\epsilon_1^2 = R_{\perp,1}^{-1}\beta \\ \widehat{\delta} &\equiv \widehat{\rho}\left[\widehat{|d-\mu_z|}\left(\widehat{\alpha}_z+\widehat{\alpha}_\parallel\right) - \left(\widehat{\alpha}^{10}_z+\widehat{\alpha}^{10}_\parallel\right)\right] = R_{\perp,1}^{-2}\delta \\ \widehat{\tau} &\equiv \widehat{\rho}\left[\widehat{|d-\mu_z|}\widehat{\alpha}_\parallel - \widehat{\alpha}^{10}_\parallel\right] = R_{\perp,1}^{-2}\tau.\end{aligned} \tag{A.3}$$

Here the normalized density is given by

$$\widehat{\rho} \equiv R_{\perp,1}^2\rho, \tag{A.4}$$

and the normalized substrate-multipole distance by:

$$\widehat{|d-\mu_z|} \equiv R_{\perp,1}^{-1}|d-\mu_z|. \tag{A.5}$$

The dimensionless versions of Eqs. (3.104) and (3.105) implemented in the code, in terms of the new dimensionless expansion coefficients, is given by:

$$\begin{aligned}
&\sum_{\ell'=1}^{M}\zeta_{\ell\ell'}^{m}\chi_s^{-\ell'-2}\left[\mathcal{I}_{\ell\ell'}^{m(2s-1)}(t_r^{(s)},\xi_{0,s})\widehat{A}_{\ell'm}^{(2s-1)}-\mathcal{I}_{\ell\ell'}^{m(2s+1)}(t_r^{(s)},\xi_{0,s})\widehat{A}_{\ell'm}^{(2s+1)}\right]\\
&+\sum_{\ell'=1}^{M}\zeta_{\ell\ell'}^{m}\chi_s^{\ell'-1}\left[\mathcal{K}_{\ell\ell'}^{m(2s-1)}(t_r^{(s)},\xi_{0,s})\widehat{B}_{\ell'm}^{(2s-1)}-\mathcal{K}_{\ell\ell'}^{m(2s+1)}(t_r^{(s)},\xi_{0,s})\widehat{B}_{\ell'm}^{(2s+1)}\right]\\
&=\delta_{s1}\Bigg[\cos\theta_0\sqrt{\frac{4\pi}{3}}\Bigg\{\frac{\epsilon_1}{\epsilon_2}\delta_{\ell1}+\left(\frac{\epsilon_1-\epsilon_2}{\epsilon_2}\right)\Big[\sqrt{3}t_r^{(1)}\zeta_{\ell0}^{0}Q_{\ell0}^{0}(-1,t_r^{(1)})\\
&-\zeta_{\ell1}^{0}Q_{\ell1}^{0}(-1,t_r^{(1)})\Big]\Bigg\}\delta_{m0}-\sqrt{\frac{2\pi}{3}}\sin\theta_0\mathrm{e}^{-i\phi_0}\sqrt{\xi_{0,1}^{-2}+1}\delta_{\ell1}\delta_{m1}\Bigg]\\
&\forall\quad s=1,2,3,...,S;\ \ell=1,2,3,...,M;\ m=0,1,
\end{aligned}\tag{A.6}$$

and

$$\begin{aligned}
&\sum_{l'=1}^{M}\zeta_{\ell\ell'}^{m}\chi_s^{-\ell'-2}\xi_{0,s}\left[\mathcal{J}_{\ell\ell'}^{m(2s-1)}(t_r^{(s)},\xi_{0,s})\widehat{A}_{\ell'm}^{(2s-1)}-\mathcal{J}_{\ell\ell'}^{m(2s+1)}(t_r^{(s)},\xi_{0,s})\widehat{A}_{\ell'm}^{(2s+1)}\right]\\
&+\sum_{l'=1}^{M}\zeta_{\ell\ell'}^{m}\chi_s^{\ell'-1}\xi_{0,s}\left[\mathcal{L}_{\ell\ell'}^{m(2s-1)}(t_r^{(s)},\xi_{0,s})\widehat{B}_{\ell'm}^{(2s-1)}-\mathcal{L}_{\ell\ell'}^{m(2s+1)}(t_r^{(s)},\xi_{0,s})\widehat{B}_{\ell'm}^{(2s+1)}\right]\\
&=\delta_{s1}\Bigg\{\sqrt{\frac{4\pi}{3}}\epsilon_1\cos\theta_0\delta_{\ell1}\delta_{m0}\\
&-\sqrt{\frac{2\pi}{3}}\sin\theta_0\mathrm{e}^{-i\phi_0}\frac{1}{\sqrt{\xi_{0,1}^{-2}+1}}\left[(\epsilon_1-\epsilon_2)\zeta_{\ell1}^{1}Q_{\ell1}^{1}(-1,t_r^{(1)})+\epsilon_2\delta_{\ell1}\right]\delta_{m1}\Bigg\}\\
&\forall\quad s=1,2,3,...,S;\ \ell=1,2,3,...,M;\ m=0,1.
\end{aligned}\tag{A.7}$$

Note how Eq. (A.7) also has been multiplied by $\xi_{0,s}$ as compared to Eq. (3.105). This was done to enable simpler comparison with the code for non-coated spheroids in an old version of GranFilm.

B. Integrals

This appendix is devoted to details surrounding the calculations of the various integrals needed to solve the systems of equations in Eqs. (3.104) and (3.105). The required integrals are

$$V^m_{\ell\ell'}[\kappa_z,\xi](\eta_1,\eta_2) \equiv \int_{\eta_1}^{\eta_2} \mathrm{d}\eta P^m_\ell(\eta) P^m_{\ell'}(\eta_\kappa(\xi,\eta)) Z^m_{\ell'}(\xi_\kappa(\xi,\eta)), \tag{B.1}$$

and

$$W^m_{\ell\ell'}[\kappa_z,\xi](\eta_1,\eta_2) \equiv \int_{\eta_1}^{\eta_2} \mathrm{d}\eta P^m_\ell(\eta) P^m_{\ell'}(\eta_\kappa(\xi,\eta)) X^m_{\ell'}(\xi_\kappa(\xi,\eta)), \tag{B.2}$$

and their derivatives which may be expressed as:

$$\begin{aligned}\frac{\partial}{\partial\xi}\left\{V^m_{\ell\ell'}[\kappa_z,\xi](\eta_1,\eta_2)\right\}\big|_{\xi=\xi_0} = \int_{\eta_1}^{\eta_2} \mathrm{d}\eta P^m_\ell(\eta)\Bigg\{ &\frac{\partial\eta_\kappa}{\partial\xi}\frac{\partial P^m_{\ell'}(\eta_\kappa)}{\partial\eta_\kappa} Z^m_{\ell'}(\xi_\kappa) \\ &+\frac{\partial\xi_\kappa}{\partial\xi}\frac{\partial Z^m_{\ell'}(\xi_\kappa)}{\partial\xi_\kappa} P^m_{\ell'}(\eta_\kappa)\Bigg\}\Bigg|_{\xi=\xi_0},\end{aligned} \tag{B.3}$$

and

$$\begin{aligned}\frac{\partial}{\partial\xi}\left\{W^m_{\ell\ell'}[\kappa_z,\xi](\eta_1,\eta_2)\right\}\big|_{\xi=\xi_0} = \int_{\eta_1}^{\eta_2} \mathrm{d}\eta P^m_\ell(\eta)\Bigg\{ &\frac{\partial\eta_\kappa}{\partial\xi}\frac{\partial P^m_{\ell'}(\eta_\kappa)}{\partial\eta_\kappa} X^m_{\ell'}(\xi_\kappa) \\ &+\frac{\partial\xi_\kappa}{\partial\xi}\frac{\partial X^m_{\ell'}(\xi_\kappa)}{\partial\xi_\kappa} P^m_{\ell'}(\eta_\kappa)\Bigg\}\Bigg|_{\xi=\xi_0}.\end{aligned} \tag{B.4}$$

The coordinates ξ_κ and η_κ are give by

$$\begin{aligned}\xi_\kappa &= \xi'[\Delta z = \kappa_z](\xi,\eta) \\ \eta_\kappa &= \eta'[\Delta z = \kappa_z](\xi,\eta),\end{aligned} \tag{B.5}$$

where the functions ξ' and η' are given by Eqs. (3.25) and (3.26). The subscript κ is a placeholder for either μ ($\Delta z = \mu_z$) or $\bar{\mu}$ ($\Delta z = 2d - \mu_z$).

The calculation of these integrals requires evaluations of the functions $X^m_\ell(\xi)$ and $Z^m_\ell(\xi)$, which are defined by Eqs. (3.45) and (3.46) respectively. As seen, the definitions contain factorials involving ℓ. It is not practical to calculate the

factorials separately when the arguments are large because of integer overflow, so in practice the fractions are transformed into products as

$$X_\ell^m(\xi) \equiv i^{m-\ell}\frac{(\ell-m)!}{(2\ell-1)!!}P_\ell^m(i\xi) = \begin{cases} i^{-\ell}\displaystyle\prod_{j=1}^{\ell}\left(\frac{j}{2j-1}\right)P_\ell^0(i\xi) & m=0 \\ i^{1-\ell}\frac{1}{\ell}\displaystyle\prod_{j=1}^{\ell}\left(\frac{j}{2j-1}\right)P_\ell^1(i\xi) & m=1 \end{cases} \tag{B.6}$$

and

$$Z_\ell^m(\xi) \equiv i^{\ell+1}\frac{(2\ell+1)!!}{(\ell+m)!}Q_\ell^m(i\xi) = \begin{cases} i^{\ell+1}\displaystyle\prod_{j=1}^{\ell}\left(\frac{2j+1}{j}\right)P_\ell^0(i\xi) & m=0 \\ i^{\ell+1}\frac{1}{\ell+1}\displaystyle\prod_{j=1}^{\ell}\left(\frac{2j+1}{j}\right)P_\ell^1(i\xi) & m>0 \end{cases}. \tag{B.7}$$

The derivatives of the transformed coordinates with respect to the coordinate ξ in the main coordinate system may be found by

$$\begin{aligned} \frac{\partial\xi_\kappa}{\partial\xi} &= \frac{1}{\sqrt{2}}\left[C_7 + \frac{\xi}{2}\left(\frac{C_3+\frac{C_6}{C_5}}{C_7}\right)\right] \\ \frac{\partial\eta_\kappa}{\partial\xi} &= \sqrt{2}\left[\frac{\Delta z}{C_7 a\xi^2} - \frac{1}{2}\left(\eta - \frac{\Delta z}{a\xi}\right)\left(\frac{C_3+\frac{C_6}{C_5}}{C_7^3}\right)\right] \end{aligned} \tag{B.8}$$

where

$$\begin{aligned} C_1 &\equiv 1 + \left(\frac{\Delta z}{a\xi}\right)^2 - 2\frac{\Delta z}{a\xi}\eta - \frac{\eta^2}{\xi^2} \\ C_2 &\equiv \frac{2}{\xi}\left(\frac{\Delta z}{a\xi} - \eta\right) \\ C_3 &\equiv \frac{\partial C_1}{\partial\xi} = -2\left(\frac{\Delta z}{a}\right)^2\frac{1}{\xi^3} + 2\left(\frac{\Delta z}{a}\right)\eta\frac{1}{\xi^2} + 2\eta^2\frac{1}{\xi^3} \\ C_4 &\equiv \frac{\partial C_2}{\partial\xi} = -4\frac{\Delta z}{a}\frac{1}{\xi^3} + 2\eta\frac{1}{\xi^2} \\ C_5 &\equiv \sqrt{C_1^2 + C_2^2} \\ C_6 &\equiv C_1C_3 + C_2C_4 \\ C_7 &\equiv \sqrt{C_1 + C_5}. \end{aligned} \tag{B.9}$$

To evaluate the Legendre functions of first and second kind, P_ℓ^m and Q_ℓ^m, recursion relations are used [26]. These relations require that the functions for

(ℓ, m) equal to $(0,0)$, $(1,0)$, $(1,1)$ and $(2,1)$ are known. These can be found from the definitions in Eqs. (3.33) and (3.37), and are given by

$$\begin{aligned} P_m^m(z) &= (2m-1)!!(1-z^2)^{m/2} \\ P_1^0(z) &= z \\ P_2^1(z) &= 3z\sqrt{1-z^2} \end{aligned} \tag{B.10}$$

for the Legendre functions of the first kind, and

$$\begin{aligned} Q_0^0(iy) &= -i\arctan(1/y) \\ Q_1^0(iy) &= y\arctan(1/y) - 1 \\ Q_1^1(iy) &= -\sqrt{1+y^2}\left[\arctan(1/y) - \frac{y}{1+y^2}\right] \\ Q_2^1(iy) &= i\sqrt{1+y^2}\left[\frac{2+3y^2}{1+y^2} - 3y\arctan(1/y)\right] \end{aligned} \tag{B.11}$$

for the Legendre functions of the second kind. All the other needed Legendre functions are now found by

$$\begin{aligned} P_\ell^m(x) &= \frac{1}{\ell-m}\left[x\,(2\ell-1)\,P_{\ell-1}^m(x) - (\ell+m-1)\,P_{\ell-2}^m(x)\right] \\ P_\ell^m(iy) &= \frac{1}{\ell-m}\left[iy\,(2\ell-1)\,P_{\ell-1}^m(iy) - (\ell+m-1)\,P_{\ell-2}^m(iy)\right] \\ Q_\ell^m(iy) &= \frac{1}{\ell-m}\left[iy\,(2\ell-1)\,Q_{\ell-1}^m(iy) - (\ell+m-1)\,Q_{\ell-2}^m(iy)\right], \end{aligned} \tag{B.12}$$

and their derivatives may also be found by recursion relations given by [26]

$$\begin{aligned} \frac{\partial P_\ell^m(x)}{\partial x} &= \frac{1}{x^2-1}\left[(\ell-m+1)\,P_{\ell+1}^m(x) - (\ell+1)\,xP_\ell^m(x)\right] \\ \frac{\partial P_\ell^m(iy)}{\partial y} &= \frac{-1}{y^2+1}\left[i\,(\ell-m+1)\,P_{\ell+1}^m(iy) + (\ell+1)\,yP_\ell^m(iy)\right] \\ \frac{\partial Q_\ell^m(iy)}{\partial y} &= \frac{-1}{y^2+1}\left[i\,(\ell-m+1)\,Q_{\ell+1}^m(iy) + (\ell+1)\,yQ_\ell^m(iy)\right]. \end{aligned} \tag{B.13}$$

C. Example: One coating, quadrupolar order

To illustrate how the systems in Eqs. (3.104) and (3.105) are solved in GranFilm, and particularly how the matrix is set up, this section will go through a relatively simple example. The example concerns an island with a single coating ($S = 2$), and is illustrated in Fig. C.1. To make it feasible to show the entire matrix for the system of equations, the example calculation is done with a very low multipole order of $M = 2$. First of all, since multipole μ is inside

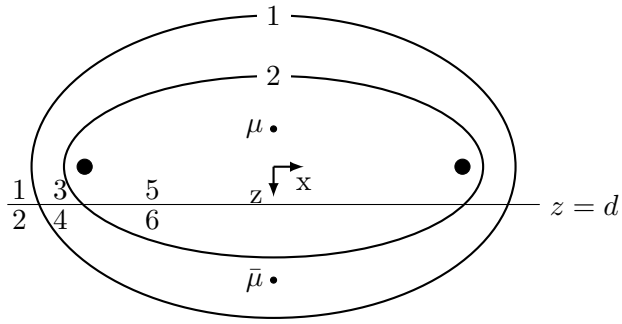

Figure C.1.: An example of a truncated spheroidal island with a single coating ($S = 2$). In this particular illustration, $\xi_{0,1} \approx 0.80$. The spheroids are labelled $s = 1, 2$ at the top, while the media are labelled 1 to 6 on the left side.

medium 5, Eq. (3.107) reduces to

$$\begin{aligned} B_{\ell m}^{(1)} &= 0 \\ A_{\ell m}^{(5)} &= 0. \end{aligned} \tag{C.1}$$

The task now is to solve for the remaining unknown coefficients by solving Eqs. (3.104) and (3.105). This is done by setting up and solving a matrix equation:

$$A_m \mathbf{x}_m = \mathbf{b}_m, \tag{C.2}$$

for $m = 0$ and $m = 1$. The matrix A_m may be set up in many different ways, as long as the vector $\mathbf{b}_m$ and the interpretation of the solution vector $\mathbf{x}_m$ is

adjusted accordingly. The matrix equation set up in the implemented code will be presented here. First of all, some shorthands must be defined to make it feasible to show the matrix:

$$\begin{aligned}
\mathcal{I}^{m,\pm}_{\ell\ell',s} &\equiv \zeta^m_{\ell\ell'}\chi_s^{-\ell'-2}\mathcal{I}^{m(2s\pm1)}_{\ell\ell'}(t^{(s)}_r,\xi_{0,s})\\
\mathcal{J}^{m\pm}_{\ell\ell',s} &\equiv \zeta^m_{\ell\ell'}\chi_s^{-\ell'-2}\xi_{0,s}\mathcal{J}^{m(2s\pm1)}_{\ell\ell'}(t^{(s)}_r,\xi_{0,s})\\
\mathcal{K}^{m\pm}_{\ell\ell',s} &\equiv \zeta^m_{\ell\ell'}\chi_s^{\ell'-1}\mathcal{K}^{m(2s\pm1)}_{\ell\ell'}(t^{(s)}_r,\xi_{0,s})\\
\mathcal{L}^{m\pm}_{\ell\ell',s} &\equiv \zeta^m_{\ell\ell'}\chi_s^{\ell'-1}\xi_{0,s}\mathcal{L}^{m(2s\pm1)}_{\ell\ell'}(t^{(s)}_r,\xi_{0,s}).
\end{aligned} \tag{C.3}$$

The matrix may then be set up as

$$A_m = \begin{bmatrix}
\mathcal{I}^{m,-}_{11,1} & \mathcal{I}^{m,-}_{12,1} & -\mathcal{I}^{m,+}_{11,1} & -\mathcal{I}^{m,+}_{12,1} & -\mathcal{K}^{m,+}_{11,1} & -\mathcal{K}^{m,+}_{12,1} & 0 & 0\\
\mathcal{I}^{m,-}_{21,1} & \mathcal{I}^{m,-}_{22,1} & -\mathcal{I}^{m,+}_{21,1} & -\mathcal{I}^{m,+}_{22,1} & -\mathcal{K}^{m,+}_{21,1} & -\mathcal{K}^{m,+}_{22,1} & 0 & 0\\
\mathcal{J}^{m,-}_{11,1} & \mathcal{J}^{m,-}_{12,1} & -\mathcal{J}^{m,+}_{11,1} & -\mathcal{J}^{m,+}_{12,1} & -\mathcal{L}^{m,+}_{11,1} & -\mathcal{L}^{m,+}_{12,1} & 0 & 0\\
\mathcal{J}^{m,-}_{21,1} & \mathcal{J}^{m,-}_{22,1} & -\mathcal{J}^{m,+}_{21,1} & -\mathcal{J}^{m,+}_{22,1} & -\mathcal{L}^{m,+}_{21,1} & -\mathcal{L}^{m,+}_{22,1} & 0 & 0\\
0 & 0 & \mathcal{I}^{m,-}_{11,2} & \mathcal{I}^{m,-}_{12,2} & \mathcal{K}^{m,-}_{11,2} & \mathcal{K}^{m,-}_{12,2} & -\mathcal{K}^{m,+}_{11,2} & -\mathcal{K}^{m,+}_{12,2}\\
0 & 0 & \mathcal{I}^{m,-}_{21,2} & \mathcal{I}^{m,-}_{22,2} & \mathcal{K}^{m,-}_{21,2} & \mathcal{K}^{m,-}_{22,2} & -\mathcal{K}^{m,+}_{21,2} & -\mathcal{K}^{m,+}_{22,2}\\
0 & 0 & \mathcal{J}^{m,-}_{11,2} & \mathcal{J}^{m,-}_{12,2} & \mathcal{L}^{m,-}_{11,2} & \mathcal{L}^{m,-}_{12,2} & -\mathcal{L}^{m,+}_{11,2} & -\mathcal{L}^{m,+}_{12,2}\\
0 & 0 & \mathcal{J}^{m,-}_{21,2} & \mathcal{J}^{m,-}_{22,2} & \mathcal{L}^{m,-}_{21,2} & \mathcal{L}^{m,-}_{22,2} & -\mathcal{L}^{m,+}_{21,2} & -\mathcal{L}^{m,+}_{22,2}
\end{bmatrix}, \tag{C.4}$$

the dimensionless vector $\mathbf{x}$ is then

$$\mathbf{x}_m = \begin{bmatrix}
R^{-1-2}_{\perp,1}A^{(1)}_{1m}/E_0\\
R^{-2-2}_{\perp,1}A^{(1)}_{2m}/E_0\\
R^{-1-2}_{\perp,1}A^{(3)}_{1m}/E_0\\
R^{-2-2}_{\perp,1}A^{(3)}_{2m}/E_0\\
R^{1-1}_{\perp,1}B^{(3)}_{1m}/E_0\\
R^{2-1}_{\perp,1}B^{(3)}_{2m}/E_0\\
R^{1-1}_{\perp,1}B^{(5)}_{1m}/E_0\\
R^{2-1}_{\perp,1}B^{(5)}_{2m}/E_0
\end{bmatrix} = \begin{bmatrix}
\widehat{A}^{(1)}_{1m}\\
\widehat{A}^{(1)}_{2m}\\
\widehat{A}^{(3)}_{1m}\\
\widehat{A}^{(3)}_{2m}\\
\widehat{B}^{(3)}_{1m}\\
\widehat{B}^{(3)}_{2m}\\
\widehat{B}^{(5)}_{1m}\\
\widehat{B}^{(5)}_{2m}
\end{bmatrix}, \tag{C.5}$$

while the right hand side vector is

$$\mathbf{b}_m = \begin{bmatrix}
b_{m,1}\\
b_{m,2}\\
b_{m,3}\\
b_{m,4}\\
0\\
0\\
0\\
0
\end{bmatrix}. \tag{C.6}$$

In this case the elements of the vector $\mathbf{b}_m$ are

$$b_{m,1} = \sqrt{\frac{4\pi}{3}}\cos\theta_0 \Bigg\{ \frac{\epsilon_1}{\epsilon_2} + \left(\frac{\epsilon_1}{\epsilon_2} - 1\right) \Big[\sqrt{3} t_r^{(1)} \zeta_{10}^0 Q_{10}^0(-1, t_r^{(1)}) - \zeta_{11}^0 Q_{11}^0(-1, t_r^{(1)}) \Big] \Bigg\} \delta_{m0} - \sqrt{\frac{2\pi}{3}} \sin\theta_0 \mathrm{e}^{-i\phi_0} \sqrt{\xi_{0,1}^{-2} + 1}\, \delta_{m1}, \tag{C.7}$$

$$b_{m,2} = \sqrt{\frac{4\pi}{3}}\cos\theta_0 \left(\frac{\epsilon_1}{\epsilon_2} - 1\right) \Big[\sqrt{3} t_r^{(1)} \zeta_{20}^0 Q_{20}^0(-1, t_r^{(1)}) - \zeta_{21}^0 Q_{21}^0(-1, t_r^{(1)}) \Big] \delta_{m0}, \tag{C.8}$$

$$b_{m,3} = \Bigg\{ \sqrt{\frac{4\pi}{3}} \epsilon_1 \cos\theta_0 \delta_{m0} - \sqrt{\frac{2\pi}{3}} \sin\theta_0 \mathrm{e}^{-i\phi_0} \frac{1}{\sqrt{\xi_{0,1}^{-2} + 1}} \Big[(\epsilon_1 - \epsilon_2) \zeta_{11}^1 Q_{11}^1(-1, t_r^{(1)}) + \epsilon_2 \Big] \delta_{m1} \Bigg\} \tag{C.9}$$

and

$$b_{m,4} = -\sqrt{\frac{2\pi}{3}} \sin\theta_0 \mathrm{e}^{-i\phi_0} \frac{1}{\sqrt{\xi_{0,1}^{-2} + 1}} (\epsilon_1 - \epsilon_2) \zeta_{21}^1 Q_{21}^1(-1, t_r^{(1)}) \delta_{m1}. \tag{C.10}$$

The system $A_m \mathbf{x}_m = \mathbf{b}_m$ should then be solved for $m = 0$ and $m = 1$. After this, the constant terms of the potential may be calculated. Setting $\psi_0^{(1)} = 0$ as usual, the first unknown constant term may be found by

$$\begin{aligned} \psi_0^{(3)} = & \frac{R_{\perp,1} E_0}{2\sqrt{\pi}} \\ & \times \Bigg\{ \zeta_{01}^0 \Big(\mathcal{I}_{01}^{0(1)}(t_r^{(1)}, \xi_{0,1}) \widehat{A}_{10}^{(1)} - \mathcal{I}_{01}^{0(3)}(t_r^{(1)}, \xi_{0,1}) \widehat{A}_{10}^{(3)} - \mathcal{K}_{01}^{0(3)}(t_r^{(1)}, \xi_{0,1}) \widehat{B}_{10}^{(3)} \Big) \\ & + \zeta_{02}^0 \Big(\mathcal{I}_{02}^{0(1)}(t_r^{(1)}, \xi_{0,1}) \widehat{A}_{20}^{(1)} - \mathcal{I}_{02}^{0(3)}(t_r^{(1)}, \xi_{0,1}) \widehat{A}_{20}^{(3)} - \mathcal{K}_{02}^{0(3)}(t_r^{(1)}, \xi_{0,1}) \widehat{B}_{20}^{(3)} \Big) \\ & + 2\sqrt{\pi} \cos\theta_0 \left(\frac{\epsilon_1}{\epsilon_2} - 1\right) \frac{1}{4} \left(1 - t_r^{(1)}\right)^2 \Bigg\}, \end{aligned} \tag{C.11}$$

while the second may be found by

$$\begin{aligned}\psi_0^{(5)} =&\psi_0^{(3)} + \frac{R_{\perp,1}E_0}{2\sqrt{\pi}}\\ &\times\Bigg\{\zeta_{01}^0\Big[\chi_2^{-2}\mathcal{I}_{01}^{0(3)}(t_r^{(2)},\xi_{0,2})\widehat{A}_{10}^{(3)} + \mathcal{K}_{01}^{0(3)}(t_r^{(2)},\xi_{0,2})\widehat{B}_{10}^{(3)}\\ &\qquad - \mathcal{K}_{01}^{0(5)}(t_r^{(2)},\xi_{0,2})\widehat{B}_{10}^{(5)}\Big]\\ &\quad + \zeta_{02}^0\Big[\chi_2^{-3}\mathcal{I}_{02}^{0(3)}(t_r^{(2)},\xi_{0,2})\widehat{A}_{20}^{(3)} + \chi_2\mathcal{K}_{02}^{0(3)}(t_r^{(2)},\xi_{0,2})\widehat{B}_{20}^{(3)}\\ &\qquad - \chi_2\mathcal{K}_{02}^{0(5)}(t_r^{(2)},\xi_{0,2})\widehat{B}_{20}^{(5)}\Big]\Bigg\}. \end{aligned} \tag{C.12}$$

D. Calculating the potential

Actually calculating the potential at a given point in space raises a few issues which do not arise when one is simply interested in the polarizabilities of the island. This mostly comes from the fact that the expressions for the potential, Eqs. (3.59) and (3.60), contain terms with $m = -1$, which are not involved when finding the polarizabilities.

The expressions for the potential in terms of the normalized multipole coefficients presented in App. A are

$$\begin{aligned}\psi_i(\mathbf{r}) = \psi_0^{(i)} &\\ &+ E_0 {\sum_{\ell m}}' R_{\perp,1}^{\ell+2} \widehat{A}_{\ell m}^{(i)} \Big[Z_\ell^m(\xi_\mu, a) Y_\ell^m(\arccos\eta_\mu, \phi_\mu) \\ &\qquad + (-1)^{\ell+m} \mathcal{R}_i Z_\ell^m(\xi_{\bar{\mu}}, a) Y_\ell^m(\arccos\eta_{\bar{\mu}}, \phi_{\bar{\mu}}) \Big] \\ &+ E_0 {\sum_{\ell m}}' R_{\perp,1}^{-\ell+1} \widehat{B}_{\ell m}^{(i)} \Big[X_\ell^m(\xi_\mu, a) Y_\ell^m(\arccos\eta_\mu, \phi_\mu) \\ &\qquad + (-1)^{\ell+m} \mathcal{R}_i X_\ell^m(\xi_{\bar{\mu}}, a) Y_\ell^m(\arccos\eta_{\bar{\mu}}, \phi_{\bar{\mu}}) \Big] \\ &+ \delta_{i,1} \psi_{\mathrm{inc}}(\xi, \eta, \phi) \end{aligned} \tag{D.1}$$

for media above the substrate surface, and

$$\begin{aligned}\psi_{i+1}(\mathbf{r}) = \psi_0^{(i+1)} &\\ &+ E_0 \mathcal{T}_i {\sum_{\ell m}}' \Big[R_{\perp,1}^{\ell+2} \widehat{A}_{\ell m}^{(i)} Z_\ell^m(\xi_\mu, a) + R_{\perp,1}^{-\ell+1} \widehat{B}_{\ell m}^{(i)} X_\ell^m(\xi_\mu, a) \Big] \\ &\qquad \times Y_\ell^m(\arccos\eta_\mu, \phi_\mu) \\ &+ \delta_{i,1} \psi_{\mathrm{tr}}(\xi, \eta, \phi) \end{aligned} \tag{D.2}$$

for media below the substrate surface.

The multipole coefficients A_ℓ^m and B_ℓ^m for $m = -1$ may be found through Eqs. (3.102) and (3.103). What remains is to find the functions X_ℓ^m, Z_ℓ^m and Y_ℓ^m. Using the definitions of P_ℓ^m and Q_ℓ^m for negative m ((3.34) and (3.38)) and the definition of $X_\ell^m(\xi, a)$ and $Z_\ell^m(\xi, a)$ ((3.45) and (3.46)), it can easily

be shown that

$$\begin{aligned} X_\ell^{-m}(\xi,a) &= X_\ell^m(\xi,a) \\ Z_\ell^{-m}(\xi,a) &= Z_\ell^m(\xi,a), \end{aligned} \tag{D.3}$$

which means that X_ℓ^m and Z_ℓ^m for any needed m may be found through the usual means. The spherical harmonics Y_ℓ^m may be found for any of the needed values of m by using the definition in Eq. (3.39):

$$\begin{aligned} Y_\ell^0(\arccos\eta,\phi) &= \sqrt{\frac{2\ell+1}{4\pi}}P_\ell^0(\eta) \\ Y_\ell^1(\arccos\eta,\phi) &= (-1)\sqrt{\frac{2\ell+1}{4\pi\ell(\ell+1)}}P_\ell^1(\eta)\mathrm{e}^{i\phi} \\ Y_\ell^{-1}(\arccos\eta,\phi) &= \sqrt{\frac{2\ell+1}{4\pi\ell(\ell+1)}}P_\ell^1(\eta)\mathrm{e}^{-i\phi}. \end{aligned} \tag{D.4}$$

The constant terms in Eqs. (D.1) and (D.2) are found in terms of the normalized multipole coefficients as

$$\begin{aligned} &\left[\psi_0^{(2s+1)} - \psi_0^{(2s-1)}\right] \\ &= \chi_s R_{\perp,1} E_0 \Bigg\{ \\ &\frac{1}{2\sqrt{\pi}}\sum_{\ell=1}^{M}\zeta_{0\ell}^0\chi_s^{-\ell-2}\left[\mathcal{I}_{0\ell}^{0(2s-1)}(t_r^{(s)},\xi_{0,s})\widehat{A}_{\ell 0}^{(2s-1)} - \mathcal{I}_{0\ell}^{0(2s+1)}(t_r^{(s)},\xi_{0,s})\widehat{A}_{\ell 0}^{(2s+1)}\right] \\ &+\frac{1}{2\sqrt{\pi}}\sum_{\ell=1}^{M}\zeta_{0\ell}^0\chi_s^{\ell-1}\left[\mathcal{K}_{0\ell}^{0(2s-1)}(t_r^{(s)},\xi_{0,s})\widehat{B}_{\ell 0}^{(2s-1)} - \mathcal{K}_{0\ell}^{0(2s+1)}(t_r^{(s)},\xi_{0,s})\widehat{B}_{\ell 0}^{(2s+1)}\right] \\ &- \delta_{s1}\cos\theta_0\left(\frac{\epsilon_1-\epsilon_2}{\epsilon_2}\right)\frac{1}{4}\left(1-t_r^{(1)}\right)^2\Bigg\} \\ &\forall \quad s = 1,2,3,...,S, \end{aligned} \tag{D.5}$$

where it has been used that

$$\xi^{-1}X_1^0(\xi) = 1, \tag{D.6}$$

$$\xi^{-1}X_1^1(\xi) = \sqrt{\xi^{-2}+1}, \tag{D.7}$$

$$\frac{\partial X_1^0(\xi)}{\partial\xi} = 1, \tag{D.8}$$

$$\frac{\partial X_1^1(\xi)}{\partial \xi} = \frac{1}{\sqrt{\xi^{-2}+1}}, \tag{D.9}$$

and

$$\frac{1}{\sqrt{3}}\zeta_{01}^0 Q_{01}^0(-1, t_r^{(1)}) + t_r^{(1)}\left(1 - \zeta_{00}^0 Q_{00}^0(-1, t_r^{(1)})\right) = -\frac{1}{4}\left(1 - t_r^{(1)}\right)^2. \tag{D.10}$$